Electrical control of a spin qubit in InSb nanowire quantum dots: Strongly suppressed spin relaxation in high magnetic field

Suzana Miladić,[1] Pavle Stipsić,[1] Edib Dobardžić,[1] and Marko Milivojević[2,3]
[1]*Faculty of Physics, University of Belgrade, Studentski trg 12, 11001 Belgrade, Serbia*
[2]*NanoLab, QTP Center, Faculty of Physics, University of Belgrade, Studentski trg 12, 11001 Belgrade, Serbia*
[3]*Department of Theoretical Physics and Astrophysics, Faculty of Science, P. J. Šafárik University, Park Angelinum 9, 040 01 Košice, Slovak Republic*

(Received 20 November 2019; revised manuscript received 2 February 2020; accepted 3 April 2020; published 22 April 2020)

In this paper we investigate the impact of gating potential and magnetic field on phonon induced spin relaxation rate and the speed of the electrically driven single-qubit operations inside the InSb nanowire spin qubit. We show that a strong g factor and high magnetic field strength lead to the prevailing influence of electron-phonon scattering due to deformation potential, considered irrelevant for materials with a weak g factor, like GaAs or Si/SiGe. In this regime we find that spin relaxation between qubit states is significantly suppressed due to the confinement perpendicular to the nanowire axis. We also find that maximization of the number of single-qubit operations that can be performed during the lifetime of the spin qubit requres single quantum dot gating potential.

DOI: 10.1103/PhysRevB.101.155307

I. INTRODUCTION

Spin of an electron confined in a semiconductor quantum dot (QD) can act as a carrier of quantum information [1] and a building block of quantum computers. In order to manipulate electron spin, usage of the external magnetic [2,3] and electric [4–6] field was suggested. Although spin control by means of a magnetic field is straightforward, electrical control of spin qubit through electric-dipole spin resonance (EDSR) is technologically more desirable [7–10].

Spin-orbit coupling (SOC) plays an essential role in the EDSR spin qubit scheme, since it allows transitions between qubit states using the spin-independent driving, such as electric-dipole interaction. On the other hand, the presence of SOC induces undesired phonon mediated transitions between qubit states [11–21]. In order to suppress the coupling to phonons, approaches like the optimal design of QDs [22,23] or the control of system size [24] was suggested.

Relaxation rates are dependent on the full three-dimensional QD potential, but in most cases contribution of the confinement along the direction(s) perpendicular to the substrate in which QDs are embedded can be neglected. Assuming magnetic fields up to several tesla, this reduction is justified in material with a weak effective Landé g factor. A typical example that satisfies this assumption are lateral GaAs QDs [25], while in the opposite direction lies an InSb nanowire, having two orders of magnitude stronger g factor [26]. Having also very strong SOC, spin qubits in InSb nanowires [27–31] have attracted much attention due to the observed [28] fast electric-dipole induced transition between qubit states, whose speed is equal to the strength of Rabi frequency.

Since both Rabi frequency and phonon induced relaxation rates are dependent on the magnetic field orientation and strength, design of the gating potential, and SOC, there is a wide range of possibility to tune their strength, with the goal of obtaining as much as possible single-qubit operations during its lifetime.

In this paper we search for the optimal regime in which electrical control of the InSb spin qubit can be achieved. We analyze both single and double quantum dot (DQD) potential and discuss its positive features and negative drawbacks on the spin qubit. In the case of double quantum dot potential, there is the possibility to tune the distance between the dots and to analyze the effects of the asymmetric gating potential. Also, we address the situations in which full three-dimensional confinement has nontrivial influence on spin relaxation rates. We will show that scattering by deformation potential dominates in this regime. Finally, to offer a quantitative insight into the spin qubit quality, we define a figure of merit as the ratio of Rabi frequency and the overall spin relaxation rate and discuss the obtained results in terms of this measure.

This paper is organized as follows. In Sec. II the single-electron Hamiltonian model of the InSb nanowire is introduced. In Sec. III we start with the definition of Rabi frequency and phonon induced spin relaxation rate between spin qubit states. After that, we independently study their dependence on tunable parameters of the system. Using the obtained results, quality of the spin qubit is discussed with the help of the figure of merit as a quantitative measure. In the end we finish the paper with a short conclusion and the impact of the presented results.

II. NANOWIRE SPIN QUBIT MODEL

We start with the Hamiltonian describing the electron confined in an InSb nanowire [30]

$$H = \frac{p^2}{2m^*} + V(x) + H_{\mathrm{so}} + H_{\mathrm{z}}, \tag{1}$$

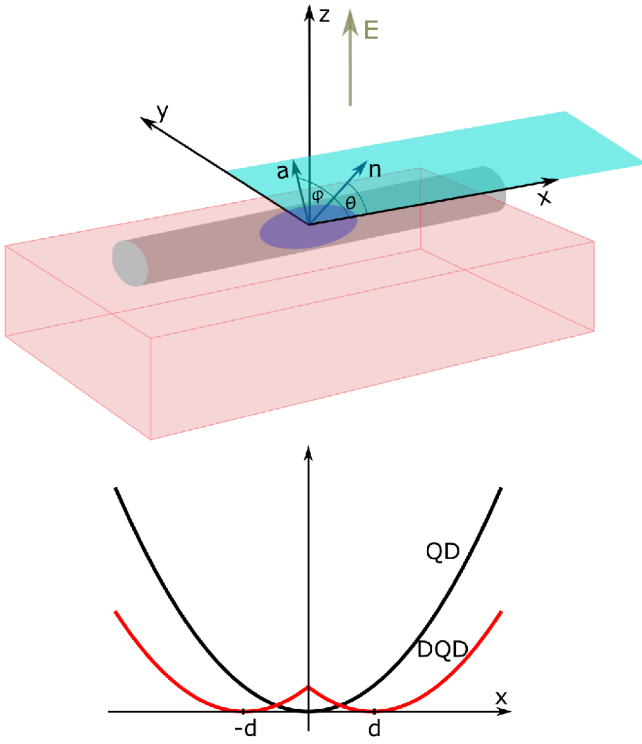

FIG. 1. (Upper panel) *Nanowire QD—schematic view.* Electron dynamics along the nanowire (x) axis is described by the Hamiltonian H, given in Eq. (1). Angle between the nanowire x axis and magnetic field direction $\mathbf{n} = (\cos\theta, \sin\theta, 0)$ is equal to θ, while the spin-orbit vector $\mathbf{a} = (\cos\varphi, \sin\varphi, 0)$ builds an angle φ with the x axis. (Lower panel) Confining potential used in Eq. (1): QD and DQD potential. In the case of a DQD potential [Eq. (6)] symmetric confinement is depicted ($\omega_L = \omega_R$), with distance between the dots equal to $2d$.

where m^* is the effective mass, $p = -i\hbar\partial/\partial_x$ momentum in x direction, $V(x)$ is the gating potential used to localize the electron, while $H_{\rm so}$ represents the spin-orbit interaction Hamiltonian consisting of two terms: Dresselhaus [32] and Rashba [33]. The presence of the Dresselhaus SOC is due to the material in which an electron is embedded. On the other hand, Rashba SOC appears when an electric field E in the z direction is applied (see Fig. 1). In an InSb nanowire, a spin-orbit interaction Hamiltonian is equal to [30]

$$H_{\rm so} = (\alpha_D\sigma_x + \alpha_R\sigma_y)p, \tag{2}$$

where σ_x and σ_y are Pauli matrices, while α_D and α_R are Dresselhaus and Rashba spin-orbit coupling strengths. Suitable change of parameters α_R and α_D with $\alpha = \sqrt{\alpha_D^2 + \alpha_R^2}$ and $\varphi = \arctan(\alpha_R/\alpha_D)$ allows us to write Eq. (2) as

$$H_{\rm so} = \alpha\boldsymbol{a}\cdot\boldsymbol{\sigma}p, \tag{3}$$

using the unit spin-orbit vector $\boldsymbol{a} = (\cos\varphi, \sin\varphi, 0)$ and the vector $\boldsymbol{\sigma}$ made of Pauli matrices. Finally, H_z is the Zeeman term, describing the coupling of spin and magnetic field

$$H_z = \frac{g}{2}\mu_B\boldsymbol{B}\cdot\boldsymbol{\sigma}, \tag{4}$$

where g is the effective Landé factor, μ_B is the Bohr magneton, while $\boldsymbol{B} = B\boldsymbol{n}$ is the applied magnetic field in the plane of the substrate, building an angle θ with the growth x axis of the nanowire (see the upper panel of Fig. 1). In this work a magnetic field is considered to be in-plane to minimize the orbital effects [22,34–36]. In Appendix A we have shown that for B up to 3 T, orbital effects of a magnetic field are small and can be neglected.

Typical gating that confines a single electron in experimental setups [37] can be modeled as a harmonic oscillator quantum dot (QD) [38] or double quantum dot (DQD) [29] potential. Corresponding potentials are equal to (see the lower panel of Fig. 1 as an illustration)

$$V^{\rm QD}(x) = \tfrac{1}{2}m^*\omega^2x^2, \tag{5}$$

$$V^{\rm DQD}(x) = \tfrac{1}{2}m^*\min\{\omega_L^2(x+d)^2, \omega_R^2(x-d)^2\}. \tag{6}$$

In the case of a QD potential, the only degree of freedom is the harmonic potential frequency ω, while in the DQD case frequencies ω_L and ω_R can be tuned, as well as the distance $2d$ between the dots. Since DQD potential allows asymmetric confinement, we introduce asymmetry parameter δ, equal to the ratio of frequencies in the left and right dot, $\delta = \omega_L/\omega_R$. Impact of the DQD confinement will be discussed in terms of δ, $2d$, and $\omega_R = \omega$ (more detailed explanation can be found in Sec. III A).

The Hamiltonian of the electron in different potential types and magnetic field strengths can be solved using the numerical diagonalization [39], although perturbative approaches in the study of spin qubit properties are common [21,27,30]. In this work we follow the numerical approach; the numerical procedure used in obtaining the eigenvalues and eigenvectors of the Hamiltonian given in Eq. (1) is explained in Appendix B. In order to successfully diagonalize the Hamiltonian, orbital $x_0 = \sqrt{\hbar/m^*\omega}$ and spin-orbit $x_{\rm so} = \hbar/m^*\alpha$ lengths are defined. In our calculations we have used $m^* = 0.014\ m_e$ [29], $x_0 = 30$ nm [29], and $x_{\rm so} = 165$ nm [40] parameters for both QD and DQD potentials (recall that $\omega_R = \omega$ in the DQD case), related to the experimental reports on InSb nanowires. On the other hand, we have used g factor in bulk InSb material, $g = -51.3$ [41], being in the range of the experimentally reported values [38,42]. Initial check of the numerical recipe presented in Appendix B were exact analytical results obtained in the special case of the infinite square well [43]. In this case we were able to reproduce the results concerning the angular dependence of the energy splitting between Zeeman sublevels, Rabi frequency, and the relaxation rate.

The nanowire Hamiltonian [Eq. (1)] describes the single-electron dynamics in the x direction only. To ensure the validity of the one-dimensional approximation and to suppress the dynamics in the yz plane, a much stronger yz plane confinement than in the x direction is needed. In this case, a wave function along both directions, y and z, will correspond to the respective ground state. To take into the account the wire geometry of the system, the same confinement length $y_0 = z_0 = 10$ nm in the $y(z)$ direction is assumed. We model the confinement potential as harmonic [39], to which the ground state wave function $\psi(y) = e^{-y^2/2y_0^2}/\sqrt{\sqrt{\pi}y_0}$ corresponds. In the z direction an additional potential eEz ($z > 0$; $z = 0$

corresponds to the position of the substrate) is present due to the applied electric field. Finally, the substrate acts as an infinite potential barrier for the confined electron, forbidding him to propagate in the $z < 0$ region [44]. The ground state $\psi(z)$ of the Hamiltonian in the z direction is found using the same numerical method as for the Hamiltonian in the x direction. Thus, the ground state wave function in the yz plane is equal to $\Psi(y, z) = \psi(y)\psi(z)$.

III. EDSR AND SPIN RELAXATION IN NANOWIRE SPIN QUBIT

In order to achieve electrical control of the nanowire spin qubit, an oscillating electric field in the x direction should be switched on, resulting in the Rabi Hamiltonian $H_R = eE_0 x\cos(\omega_E t)$. When the applied electric field is in resonance with our quantum system, Rabi frequency Ω_{01} is defined as

$$\Omega_{01} = \frac{eE_0}{h}|\langle 0|x|1\rangle|, \tag{7}$$

measuring the speed of the single-qubit rotations. In Eq. (7) states $|0\rangle$ and $|1\rangle$ correspond to the ground and first excited state of the single electron Hamiltonian H, while $e|\langle 0|x|1\rangle|$ is the dipole matrix element. We are particularly interested in the case where qubit states are Zeeman sublevels of the orbital ground state, since in this regime strength of the Rabi frequency can be manipulated by changing the magnetic field orientation [30].

Besides providing the opportunity to electrically control the spin qubit, SOC triggers the undesired phonon induced transition between qubit states, setting up a limit on the qubit lifetime. Rate of spin relaxation can be determined from the Fermi golden rule

$$\Gamma_{01} = \frac{2\pi}{\hbar}\sum_{\nu\mathbf{q}}|M_\nu(\mathbf{q})|^2|\langle\psi_0|e^{i\mathbf{q}\cdot\mathbf{r}}|\psi_1\rangle|^2\delta(\Delta E_{01} - \hbar\omega_{\nu\mathbf{q}}). \tag{8}$$

Transition is triggered by acoustic phonons of energy $\hbar\omega_{\nu\mathbf{q}}$ that correspond to the energy separation between qubit states, $\Delta E_{01} = |E_0 - E_1|$. We assume a linear dispersion relation of acoustic phonons with respect to the intensity of wave vector $\mathbf{q}$, $\omega_{\nu\mathbf{q}} = c_\nu|\mathbf{q}|$, yielding $|\mathbf{q}| = \Delta E_{01}/\hbar c_\nu$.

Next, three different geometric factors $|M_\nu(\mathbf{q})|^2$ entering spin relaxation rates originate from different types of electron-phonon scattering: electron-longitudinal phonon scattering due to the deformation potential [45]

$$|M_{\mathrm{LA-DP}}(\mathbf{q})|^2 = \frac{\hbar D^2}{2\rho c_{\mathrm{LA}}V}|\mathbf{q}|, \tag{9}$$

electron-longitudinal phonon scattering due to the piezoelectric field [45]

$$|M_{\mathrm{LA-PZ}}(\mathbf{q})|^2 = \frac{32\pi^2\hbar(eh_{14})^2}{\epsilon^2\rho c_{\mathrm{LA}}V}\frac{(3q_xq_yq_z)^2}{|\mathbf{q}|^7}, \tag{10}$$

where h_{14} is piezoelectric constant, and electron-transverse phonon scattering due to the piezoelectric field [45]

$$|M_{\mathrm{TA-PZ}}(\mathbf{q})|^2 = 2\frac{32\pi^2\hbar(eh_{14})^2}{\epsilon^2\rho c_{\mathrm{TA}}V} \times\left|\frac{q_x^2q_y^2 + q_x^2q_z^2 + q_y^2q_z^2}{|\mathbf{q}|^5} - \frac{(3q_xq_yq_z)^2}{|\mathbf{q}|^7}\right|. \tag{11}$$

Finally, spin relaxation rates are dependent on the transition matrix element $|\langle\psi_0|e^{i\mathbf{q}\cdot\mathbf{r}}|\psi_1\rangle|^2$ which depends on the full three-dimensional confinement. In order to divide the contribution of confinements along the nanowire axis and the yz plane, we write the transition matrix element as $|\langle 0|e^{iq_xx}|1\rangle|^2|T_{yz}|^2$, where $|\langle 0|e^{iq_xx}|1\rangle|^2$ is the contribution along the nanowire direction, while

$$|T_{yz}|^2 = \left|\iint dydz|\Psi(y, z)|^2e^{i(q_yy+q_zz)}\right|^2 \tag{12}$$

represents scattering in a plane perpendicular to the nanowire axis.

The role of $|T_{yz}|^2$ in the spin relaxation rate depends on the regime in which spin qubit operates. At low magnetic fields, when $|\mathbf{q}|z_0 \ll 1$ and $|\mathbf{q}|y_0 \ll 1$, dipole approximation $e^{i\mathbf{q}\cdot\mathbf{r}} \approx 1 + i\mathbf{q}\cdot\mathbf{r}$ is valid [22] and $|T_{yz}|^2$ can be replaced with $(1 + |\mathbf{q}|^2z_0^2\cos^2\theta) \approx 1$, implying that one-dimensional approximation is justified. However, at higher magnetic fields, dipole approximation is not valid and confinement in the yz direction can play a significant role. To determine its role in the spin relaxation rate, we have numerically calculated $|T_{yz}|^2$ beyond the dipole approximation.

Magnetic field strengths for which the system operates outside of the dipole approximation ($|\mathbf{q}|y_0 \geqslant 1$) can be roughly estimated; assuming energy separation between qubit states proportional to $g\mu_BB$, Fermi golden rule determines phonon wave number $|\mathbf{q}| = g\mu_BB/(\hbar c_\lambda)$, where $c_{\mathrm{LA}} = 3800$ m/s [46] and $c_{\mathrm{TA}} = 1900$ m/s [47], giving us magnetic field strengths for the electron-phonon scattering in the longitudinal (0.084 T) and transverse (0.042 T) direction above which we are outside of the dipole approximation.

Before we continue, we provide necessary parameters for the calculation of the spin relaxation rate: $eh_{14} = 1.41 \times 10^9$ eV/m [45], $\epsilon = 16.5$, $D = 7$ eV [48], $\rho = 5775$ kg/m^3 [49].

A. Rabi frequency

We start the discussion of obtained results with the analysis of Rabi frequency dependence on the parameters of interest.

In Fig. 2(a), dependence of Ω_{01} (in eE_0x_0/h units) on $\theta - \varphi$ and magnetic field strength is presented for the QD confinement potential. Our results confirm the expected π periodic behavior with respect to $\theta - \varphi$ [30]. Depending on the magnetic field strength, results can be divided into two classes. In the first class qubit states represent Zeeman sublevels of the orbital ground state; in this regime zero Rabi frequency can be found for special magnetic field orientations ($\theta - \varphi = 0, \pi$), since these qubit states have orthogonal spin components. In the second class, magnetic field strengths have led to rearrangement of energy levels, such that qubit states originate from the ground and the first excited orbital state. In this situation, an orbital qubit is constructed, with a very weak dependence of Ω_{01} on $\theta - \varphi$ ($\Omega_{01} \neq 0$ in the orbital qubit regime for any $\theta - \varphi$). Critical magnetic field value B_c of spin to orbital qubit transition is almost independent on $\theta - \varphi$ and can be easily determined from the eigenspectrum analysis. Alternatively, for $\theta - \varphi = 0, \pi$, abrupt switch of Ω_{01} from zero to the nonzero value at B_c is a fingerprint of the

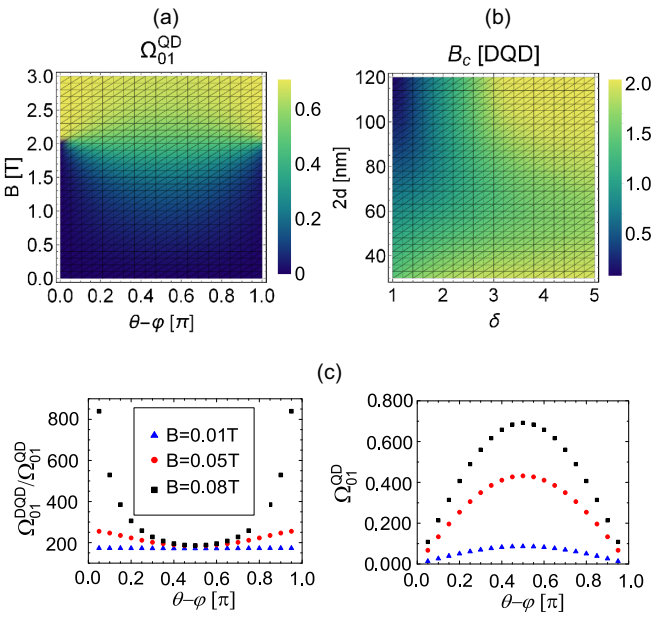

FIG. 2. (a) Dependence of Rabi frequency Ω_{01}^{QD} (in eE_0x_0/h units) on $\theta-\varphi \in (0,\pi)$ and $B \in (0,3)$ T for QD gating potential. (b) In the case of DQD confinement, dependence of B_c on the asymmetry parameter $\delta \in (1,5)$ and distance between the dots $2d \in (30,120)$ nm is given. (c) Dependence of the ratio $\Omega_{01}^{DQD}/\Omega_{01}^{QD}$ on $\theta-\varphi \in (0.05,0.95)\pi$ and magnetic field strengths $B = 0.01$ T, $B = 0.05$ T, and $B = 0.08$ T is presented for the symmetric DQD potential; distance between the dots is equal to $2d = 120$ nm. For the same angle range and magnetic field values Ω_{01}^{QD} in eE_0x_0/h units is presented.

transition. In the case of the QD potential, we extract the critical magnetic field value $B_c \approx 2.04$ T.

Gating with DQD potential gives a qualitatively similar dependence of Ω_{01} on B and $\theta-\varphi$. Being interested in the qualitative comparison of the impacts of QD and DQD potentials, we first establish a basis for comparison between them. To this end, we assume the same frequency of the QD potential and the right dot of the DQD potential, $\omega = \omega_R$, and vary the asymmetry parameter δ and the distance between the dots $2d$. For highly asymmetric DQD confinement and the large interdot distance, the electron will reside on only one dot, i.e., this potential is effectively the same as the single QD potential. The qualitative similarity of the single and double QD potential is checked through the comparison of the probability density of the ground and first excited state (qubit states); similar probability density profiles of the qubit states directly correspond to the similar Rabi frequency values of the two systems. Using the numerical comparison of the probability densities and the Rabi frequency in the case of QD and DQD potential, it can be concluded that for $2d \geqslant 120$ nm and $\delta \geqslant 5$ there is no effective difference between the results arising from two potentials. In other words, one should use $\delta < 5$ and $2d < 120$ nm to test the genuine effects of the DQD potential.

Figure 2(b) depicts the dependence of B_c in the DQD case on $\delta \in (1,5)$ and $2d \in (30,120)$ nm. When compared to the B_c value in the QD case, drastically lower values are found, especially in the case of symmetric confinement with well separated left and right QD. As an example, critical magnetic field value $B_c \approx 0.085$ T for the symmetric DQD confinement with $2d = 120$ nm is roughly 24 times smaller than in the QD case.

Lower B_c for the symmetric DQD confinement is followed by at most factor 3 increase of $\Omega_{01}(B_c^{DQD})$, when compared to $\Omega_{01}(B_c^{QD})$. This slight increase, followed by lower B_c below which symmetric DQD operates, indicates a steeper rise of Rabi frequency for symmetric DQD confinements and the possibility to induce an even bigger difference between Ω_{01}^{DQD} and Ω_{01}^{QD} for the optimal magnetic field configuration. To investigate this possibility, we have performed a numerical analysis of the Rabi frequency ratio $\Omega_{01}^{DQD}/\Omega_{01}^{QD}$ for a wide range of DQD confinements and different magnetic field strengths/orientations, such that both systems operate as spin qubits. Our results confirm that symmetric DQD confinement maximally enhances this ratio when operating at magnetic field strengths close to B_c for the DQD potential, while the field orientation should be chosen such that $\theta-\varphi$ is close to 0 or π. In order to illustrate this conclusion, in the left panel of Fig. 2(c) we present the ratio $\Omega_{01}^{DQD}/\Omega_{01}^{QD}$ for $2d = 120$ nm and $\delta = 1$ in the DQD case, assuming field orientations $\theta-\varphi \in (0.05,0.95)\pi$ and magnetic field strengths $B = 0.01$ T, $B = 0.05$ T, and $B = 0.08$ T ($B_c^{DQD} \approx 0.085$ T for this setup). Since angles $\theta-\varphi = 0,\pi$ should be excluded from the analysis because they correspond to zero Rabi frequency, we have restricted our plots to a $\theta-\varphi$ region smaller than π [see the right panel of Fig. 2(c) for the Ω_{01}^{QD} values], obtaining the highest ratio of around 800. It should be noticed that for angles closer to $0/\pi$ even bigger ratios (10^4) can be obtained, but at the cost of lowering the value of Rabi frequency.

B. Spin relaxation

Another important component for determining spin qubit quality is the spin relaxation rate. Similarly as Rabi frequency, Γ_{01} is dependent on the magnetic field and gating potential. However, Γ_{01} can be additionally dependent on the confinement in yz plane. In order to compare the influence of three-dimensional confinement with the confinement along the nanowire axis solely, we define one-dimensional approximation of the relaxation rate Γ_{01}^{1D} by changing the transition matrix element $|\langle\psi_0|e^{i\mathbf{q}\cdot\mathbf{r}}|\psi_1\rangle|^2$ with $|\langle 0|e^{iq_x x}|1\rangle|^2$ in Eq. (8).

It has been known that in lateral GaAs QDs spin relaxation rates are dominated by piezoelectric field [50,51]. In our case, we wish to analyze the influence of each relaxation channel; thus, the overall spin relaxation rate will be divided into three contributions:

$$\Gamma_{01} = \Gamma_{01}^{LA-DP} + \Gamma_{01}^{LA-PZ} + \Gamma_{01}^{TA-PZ}, \tag{13}$$

each dependent on a different geometric factor, see Eqs. (9)–(11).

Before presenting the numerical results, conclusions independent on the choice of gating potentials are provided. First, Γ_{01} shows oscillatory dependence on the $\theta-\varphi$ angle, being equal to zero for $\theta-\varphi = 0,\pi$ and reaching the maximum for $\theta-\varphi = \pi/2$ in the spin qubit regime [21]. Second, for weak magnetic field strengths ($B < 0.1$ T), piezoelectric fields dominate relaxation rates. At the same time, yz confinement can be ignored.

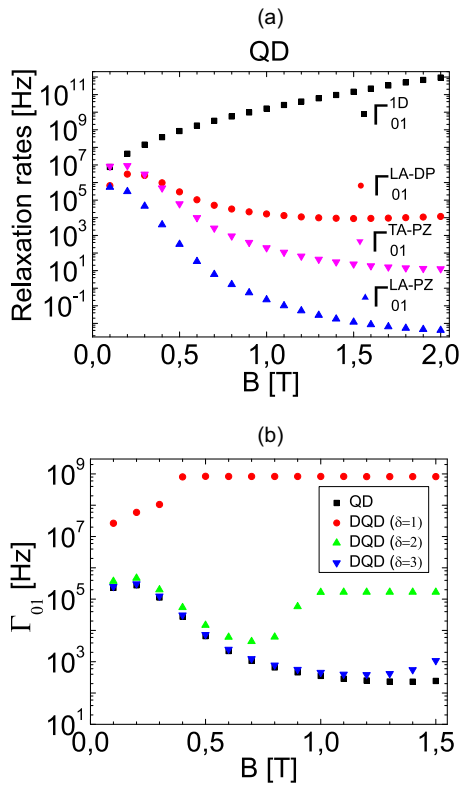

FIG. 3. (a) Dependence of the relaxation rates on the magnetic field strength $B \in (0.1, 2)\,\mathrm{T}$ for $\theta - \varphi = \pi/2$. Red circles represent the contribution of deformation potential in the scattering rates, while inverted pink (blue) triangles show the contribution of piezoelectric field for the electron-phonon scattering in the transverse (longitudinal) direction. Finally, black squares represent relaxation rates in the one-dimensional approximation, in which the contribution of the confinement perpendicular to the nanowire axis is neglected. (b) Dependence of Γ_{01} on the magnetic field strength $B \in (0.1, 1.5)\,\mathrm{T}$ in the case of QD and DQD confinement potential. Magnetic field orientation is chosen such that $\theta - \varphi = 0.05\pi$. In the DQD case, the distance between the dots is set at 90 nm, while the asymmetry parameter is varied.

To explore a new type of behavior accessible in InSb spin qubits, we focus our attention on stronger magnetic fields and investigate its impact on each relaxation channel and one-dimensional approximation of the total relaxation rate Γ_{01}^{1D}. We start from the QD potential. In Fig. 3(a), dependence of relaxation rates on $B \in (0.1, 2)\,\mathrm{T}$ for the fixed angle $\theta - \varphi = \pi/2$ is given [52]. Red circles represent the contribution of deformation potential, pink inverse (blue) triangles denote the impact of piezoelectric field in the electron-phonon scattering along the transverse (longitudinal) direction. Graphs show that relaxation rate Γ_{01}^{LA-PZ} can safely be ignored, while Γ_{01}^{LA-DP} and Γ_{01}^{TA-PZ} have nontrivial influence on Γ_{01}. For weak magnetic fields Γ_{01}^{TA-PZ} term is dominant, while for large magnetic fields Γ_{01}^{LA-DP} should be considered solely [39]. A different influence of Γ_{01}^{TA-PZ} and Γ_{01}^{LA-DP} lies in the opposite behavior of the corresponding geometric factors: $|M_{TA-PZ}(\mathbf{q})|^2$ [$|M_{LA-DP}(\mathbf{q})|^2$] is inversely (directly) proportional to the energy splitting between the Zeeman levels and decreases (increases) with the magnetic field rise.

Contribution of the yz plane confinement on the spin relaxation rate can be determined by comparing the Γ_{01}^{1D} with relaxation rate channels. The comparison is illustrated in Fig. 3(a), clearly demonstrating that one-dimensional approximation of the spin relaxation rate is valid only for weak magnetic fields, below 0.1 T. At higher fields, due to the strong g factor of the InSb material, both $|\mathbf{q}|y_0$ and $|\mathbf{q}|z_0$ are greater than one, triggering the effects of the yz plane confinement for each relaxation rate channel. Thus, suppressed spin relaxation represents a fingerprint of a material with a strong g factor.

In the case of DQD potentials, dependence of B_c on the form of gating presents a serious limitation on the regimes that can be accessed. For example, if the B_c value is sufficiently weak, $B_c < 0.1\,\mathrm{T}$, the spin qubit operates under the dominant influence of the piezoelectric field. A strong magnetic field regime is beneficial for spin qubit operation due to strong Rabi frequency and suppressed spin relaxation. In order to operate in this regime, asymmetric DQD potential should be used. To compare the influence of QD and DQD potential on Γ_{01}, in Fig. 3(b), we plot the dependence of the spin relaxation rate in the case of QD and DQD confinement on the magnetic field strength $B \in (0.1, 1.5)\,\mathrm{T}$, assuming $\theta - \varphi = \pi/2$ and $2d = 90\,\mathrm{nm}$. Besides the symmetric $\delta = 1$ confinement, asymmetric DQD confinements ($\delta = 2, 3$) were analyzed as well. The presented results show that DQD gating leads to increased relaxation rates, when compared to the QD potential. This difference is minimized for highly asymmetric gating potentials. Note that B independent Γ_{01} values suggest that orbital qubit is created: energy difference between the states with the same spin component (representing the orbital qubit states in our case) is independent on B and triggers phonons on the same energy, leading to the observed effect. Consequently, these points should be excluded from the spin qubit analysis.

Finally, we emphasize that in the special case of the asymmetric DQD potential with $\delta = 1.5$ a similar trend of the spin relaxation rate is ascertained [21], i.e., after the increase of the spin relaxation rate in the dominant regime of the piezoelectric field, suppression of spin relaxation is observed, followed by the increase up to magnetic field independent saturation value [see the green triangles in Fig. 3(b) as a comparison].

C. Spin qubit quality

Quantitative estimate of the spin qubit quality can be given with the help of the figure of merit ξ [22],

$$\xi = \frac{\Omega_{01}}{\Gamma_{01} + \Gamma_o}, \tag{14}$$

measuring the number of qubit operations that can be implemented during the qubit lifetime. In Eq. (14) Γ_o represents relaxation rate of decay channels different from phonons. To divide the contribution of phonons from them, we rewrite ξ in terms of the phonon figure of merit $\xi_{ph} = \Omega_{01}/\Gamma_{01}$ and relative influence of other channels with respect to phonons Γ_o/Γ_{01}. Thus,

$$\xi = \frac{\xi_{ph}}{1 + \frac{\Gamma_o}{\Gamma_{01}}}. \tag{15}$$

We first analyze ξ_{ph} for the QD confinement. Neglecting the weak magnetic field regime [53], in Fig. 4 we

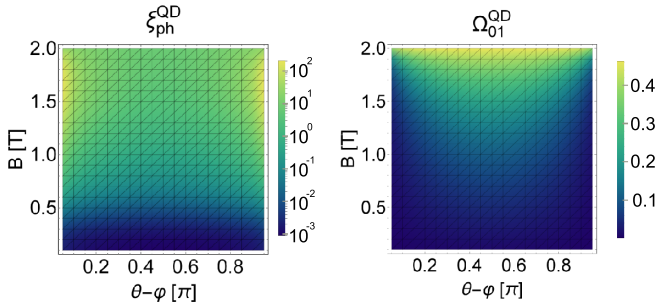

FIG. 4. For the QD confining potential, dependence of the figure of merit $\xi_{\rm ph}^{\rm QD}$ (given in dimensionless unit 7.25 $\frac{\rm m}{\rm V}\times E_0$) and Rabi frequency (in eE_0x_0/h units) on the relative angle $\theta-\varphi\in(0.05, 0.95)\pi$ and magnetic field strength $B\in(0.1, 2)$ T is presented.

present the dependence of $\xi_{\rm ph}^{\rm QD}$ on $B\in(0.1, 2)$ T and $\theta-\varphi\in(0.05, 0.95)\pi$. The restricted $\theta-\varphi$ domain plotted is due to the *a priori* exclusion of $\theta-\varphi=0,\pi$ values ($\Gamma_{01}^{\rm QD}=0$ in these situations). Plots show that to maximal value of $\xi_{\rm ph}^{\rm QD}$ correspond relative angles $\theta-\varphi=0.05\pi, 0.95\pi$. This result suggests that for $\theta-\varphi$ closer to 0 or π than presented even bigger $\xi_{\rm QD}$ values can be obtained, at the cost of lowering the Rabi frequency. In other words, $\Gamma_{01}^{\rm QD}$ has a steeper decline to zero than $\Omega_{01}^{\rm QD}$, when $\theta-\varphi$ goes from $\pi/2$ to 0 or π.

Magnetic field orientation isotropy of $\Gamma_{\rm o}$ [51] implies that shift from $\theta-\varphi=\pi/2$ increases $\Gamma_{\rm o}/\Gamma_{01}^{\rm QD}$ also. Thus, in order to maximize ξ, optimization of both $\xi_{\rm ph}^{\rm QD}$ and $\Gamma_{\rm o}/\Gamma_{01}^{\rm QD}$ is needed. Since at high magnetic fields phonon induced relaxation dominates [51], deviation of $\theta-\varphi$ from $\pi/2$ improves the spin qubit quality until $\Gamma_{\rm o}/\Gamma_{01}^{\rm QD}$ drops below 1. This sets up the optimal magnetic field orientation.

Finally, we compare the impacts of DQD and QD potentials on the spin qubit quality. As discussed in Sec. III A, Rabi frequency in the DQD case can be three orders of magnitude greater than in the QD case. Enhanced Rabi frequency suggests that SOC effects are more pronounced; thus, phonon induced spin relaxation rate should be enhanced. When compared to the QD case, an increase of $\Gamma_{01}^{\rm DQD}$ followed by the negative trend of $\xi_{\rm ph}^{\rm DQD}$ ensures that spin qubit quality decreases; symmetric DQD confinements give the poorest results, while highly asymmetric DQD potentials provide similar values as for QD gating.

IV. CONCLUSIONS

We have investigated the influence of gating potentials, magnetic field strength and orientation on Rabi frequency and spin relaxation rate in a single electron InSb nanowire spin qubit. Due to the strong Landé g factor, we were able to show that InSb spin qubit can operate in the regime in which deformation potential of acoustic phonons dominate relaxation rate. Qualitatively new behavior of spin relaxation rate comes from the confinement perpendicular to the nanowire axis, offering a new regime in which spin qubit can successfully operate. We have shown that gating potential has a crucial role in enabling such a situation, additionally pointing out simple harmonic potential as beneficial for the optimal definition of a spin qubit. Although presented for InSb nanowire spin qubits, conclusions remain valid for spin qubits in other materials with a strong g factor. Thus, modifications of g due to different effects, e.g., strong in-plane magnetic field [54], do not interfere with the conclusions stated in this work.

ACKNOWLEDGMENTS

This research was funded by the Ministry of Education, Science, and Technological Development of the Republic of Serbia under projects ON171035 and ON171027 and the National Scholarship Programme of the Slovak Republic (ID 28226).

APPENDIX A: DERIVATION OF THE EFFECTIVE ONE-DIMENSIONAL HAMILTONIAN

Here we derive the effective one-dimensional Hamiltonian H of the electron in an InSb quantum wire, by averaging the three-dimensional kinetic energy term $T_{\rm 3D}$ and two-dimensional spin-orbit Hamiltonian $H_{\rm so}^{\rm 2D}$ over y and z direction. Thus, we start from the three-dimensional Hamiltonian

$$H_{\rm 3D}=T_{\rm 3D}+V(x)+H_{\rm so}^{\rm 2D}+H_z, \tag{A1}$$

where $T_{\rm 3D}=\sum_{i=x,y,z}P_i^2/2m^*$ ($P_i=p_i+eA_i$),

$$H_{\rm so}^{\rm 2D}=\alpha_R(P_x\sigma_y-P_y\sigma_x)+\alpha_D(P_x\sigma_x-P_y\sigma_y), \tag{A2}$$

while $V(x)$ and H_z are the gating potential and the Zeeman term, defined in Eq. (4) and Eqs. (5) and (6), respectively. The choice of the vector potential components $A_x=-Bz\sin\theta$, $A_y=0$, $A_z=-By\cos\theta$ is such that it corresponds to the applied in-plane magnetic field $\mathbf{B}=B(\cos\theta,\sin\theta,0)$. After averaging the kinetic energy operator over the y and z direction using the ground state wave function $\Psi(y,z)=\psi(y)\psi(z)$, we get

$$\langle T\rangle=\frac{p_x^2}{2m^*}-\frac{eB\langle z\rangle\sin\theta}{m^*}p_x+\left[\frac{\langle p_y^2\rangle}{2m^*}+\frac{\langle(p_z-eBy\cos\theta)^2\rangle}{2m^*}+\frac{e^2B^2\sin^2\theta\langle z^2\rangle}{2m^*}\right]. \tag{A3}$$

In the previous equation, only the first and second term affect the dynamics in the x direction, while all terms in the square brackets can be considered the constant shift of energy and, therefore, can be neglected.

Next, effective one-dimensional spin-orbit interaction Hamiltonian is equal to

$$\begin{aligned}\langle H_{\rm so}\rangle&=\alpha_R((p_x-eB\langle z\rangle\sin\theta)\sigma_y-\langle p_y\rangle\sigma_x)\\&\quad+\alpha_D((p_x-eB\langle z\rangle\sin\theta)\sigma_x-\langle p_y\rangle\sigma_y)\\&=(p_x-eB\langle z\rangle\sin\theta)(\alpha_R\sigma_y+\alpha_D\sigma_x),\end{aligned} \tag{A4}$$

where we have used the fact that expectation value of the momentum p_y, $\langle p_y\rangle=\int_{-\infty}^{\infty}\Psi^*(y,z)p_y\Psi(y,z)$, is explicitly equal to zero.

A further simplification of the effective Hamiltonian can be made by neglecting the term $eB\langle z\rangle\sin\theta\,p_x/m^*$ from Eq. (A3) and $eB\langle z\rangle\sin\theta$ from Eq. (A4). Assuming that intensity of p_x

is proportional to $\hbar/x_0$, magnetic field dependent terms can be neglected if the relation

$$\frac{\hbar}{x_0} \gg eB\langle z\rangle \tag{A5}$$

is satisfied. More concretely, when the $\hbar/x_0$ is for a factor of 10 stronger than the magnetic field dependent term, orbital effects of the magnetic field are small and can be discarded. In our calculations, the magnetic field strengths of interest are up to 3 T, yielding the relation for the z expectation value

$$\langle z\rangle \leqslant 0.1\frac{\hbar}{ex_0 \times 3\ \mathrm{T}} \tag{A6}$$

that has to be satisfied to successfully operate in this regime. As discussed in Sec. II, the wave function $\psi(z)$ is dependent on the strength of the applied electric field E: with the increase of the electric field strength $\langle z\rangle$ increases. In other words, the strength of the electric field is limited from above. Numerical estimate for the critical value of electric field is 6.5×10^6 V/m, going to be used in our numerical calculations. Under these assumptions, the effective one-dimensional Hamiltonian resembles the one defined in Eq. (1), used in the rest of the paper.

APPENDIX B: NUMERICAL SOLUTION OF THE ONE-DIMENSIONAL SCHRÖDINGER EQUATION

In order to find eigenvectors and eigenenergies of the Hamiltonian H, given in Eq. (1), numerical diagonalization is performed. After defining orbital and spin-orbit lengths as x_0 and $x_{so} = \hbar/m\alpha$, respectively, such that $x = x_0 u$, where u is dimensionless variable, H can be written in the following form:

$$H = \frac{\hbar^2}{2m^* x_0^2} H_{\mathrm{red}}. \tag{B1}$$

Eigenvectors of H are the same as of H_{red}, while eigenvalues of H and H_{red} differ for the factor $\hbar^2/2m^* x_0^2$, having the energy units. The benefits of using H_{red} instead of H stems from the transfer into dimensionless units, more suitable for numerical manipulation. The concrete form of H_{red} is equal to

$$H_{\mathrm{red}} = -\frac{d^2}{du^2} - 2i\frac{x_0}{x_{so}}\mathbf{a}\cdot\boldsymbol{\sigma}\frac{d}{du} + V_{\mathrm{eff}}(u) + g_{\mathrm{eff}}\boldsymbol{n}\cdot\boldsymbol{\sigma}, \tag{B2}$$

where g_{eff} and $V_{\mathrm{eff}}(u)$ are effective Landé factor and effective potential, respectively,

$$g_{\mathrm{eff}} = g\frac{m^* x_0^2 \mu_B B}{\hbar^2}, \quad V_{\mathrm{eff}}(u) = \frac{2m^* x_0^2}{\hbar^2} V(x_0 u), \tag{B3}$$

while vectors $\mathbf{a}$ and $\mathbf{n}$ are spin-orbit and magnetic field unit vectors, respectively, defined in the main text. The form of effective potential depends on the choice of gating potential (5) and (6), while effective Landé factor is linearly dependent on the magnetic field strength B.

To numerically solve the eigenproblem of H_{red}, orbital space is discretized with an uniform grid. First and second derivative of a wave function are approximated by finite difference uniform grid formulas [55]

$$\frac{d\psi(u)}{du} = \frac{\psi_{-4}}{280h} - \frac{4\psi_{-3}}{105h} + \frac{\psi_{-2}}{5h} - \frac{4\psi_{-1}}{5h} - \frac{\psi_4}{280h} + \frac{4\psi_3}{105h} - \frac{\psi_2}{5h} + \frac{4\psi_1}{5h} + O(h^8), \tag{B4}$$

$$\frac{d^2\psi(u)}{du^2} = -\frac{\psi_{-4}}{560h^2} + \frac{8\psi_{-3}}{315h^2} - \frac{\psi_{-2}}{5h^2} + \frac{8\psi_{-1}}{5h^2} - \frac{205\psi_0}{72h^2} - \frac{\psi_4}{560h^2} + \frac{8\psi_3}{315h^2} - \frac{\psi_2}{5h^2} + \frac{8\psi_1}{5h^2} + O(h^8), \tag{B5}$$

with accuracy to the h^8 order, where h is the uniform grid step. By definition, $\psi_{\pm n} = \psi(u \pm nh)$ represent wave functions shifted in the left/right $(-/+)$ direction of the coordinate space for nh.

Uniform grid formulas allow us to represent the Hamiltonian as a square matrix. Effective potential is represented as a diagonal matrix, while matrix representation of the first and second order derivative have nondiagonal terms in addition. Since H_{red} is dependent on spin degrees of freedom also, the orbital part of the Hamiltonian is trivially extended in the spin space. Also, the Zeeman Hamiltonian is trivially extended in the orbital space, while the matrix form of the spin-orbit Hamiltonian is obtained as a tensor product of the first derivative matrix and spin Hamiltonian $\mathbf{a}\cdot\boldsymbol{\sigma}$.

In the QD case, harmonic potential is centered at $u = 0$, while in the case of DQD potential numerical calculations assumed each QD center range from $u = \pm 1/2$ to $u = \pm 2$. We have checked that for all studied situations the choice of u from the interval $(-8, 8)$ is enough to capture the smooth decline of the orbital wave function to 0 at $u = \pm 8$. Also, the division of the orbital space into $N = 2000$ parts was enough to ensure convergence of the results, i.e., for the increase of N to 4000 the relative difference between the results is below 10^{-4}.

[1] C. H. Bennett and D. P. DiVincenzo, Nature (London) **404**, 247 (2000).

[2] F. H. L. Koppens, C. Buizert, K. J. Tielrooij, I. T. Vink, K. C. Nowack, T. Meunier, L. P. Kouwenhoven, and L. M. K. Vandersypen, Nature (London) **442**, 766 (2006).

[3] D. Press, T. D. Ladd, B. Zhang, and Y. Yamamoto, Nature (London) **456**, 218 (2008).

[4] V. N. Golovach, M. Borhani, and D. Loss, Phys. Rev. B **74**, 165319 (2006).

[5] K. C. Nowack, F. H. L. Koppens, Yu. V. Nazarov and L. M. K. Vandersypen, Science **318**, 1430 (2007).

[6] R. Brunner, Y.-S. Shin, T. Obata, M. Pioro-Ladriére, T. Kubo, K. Yoshida, T. Taniyama, Y. Tokura, and S. Tarucha, Phys. Rev. Lett. **107**, 146801 (2011).

[7] E. Kawakami, P. Scarlino, D. R. Ward, F. R. Braakman, D. E. Savage, M. G. Lagally, M. Friesen, S. N. Coppersmith, M. A. Eriksson, and L. M. K. Vandersypen, Nat, Nanotechnol. **9**, 666 (2014).

[8] K. Takeda, J. Yoneda, T. Otsuka, T. Nakajima, M. R. Delbecq, G. Allison, Y. Hoshi, N. Usami, K. M. Itoh, S. Oda, T. Kodera, and S. Tarucha, npj Quantum Inf. **4**, 54 (2018).

[9] D. V. Khomitsky, L. V. Gulyaev, and E. Ya. Sherman, Phys. Rev. B **85**, 125312 (2012).

[10] D. V. Khomitsky, E. A. Lavrukhina, and E. Ya. Sherman, Phys. Rev. B **99**, 014308 (2019).

[11] A. V. Khaetskii and Y. V. Nazarov, Phys. Rev. B **61**, 12639 (2000).

[12] A. V. Khaetskii and Y. V. Nazarov, Phys. Rev. B **64**, 125316 (2001).

[13] D. Mozyrsky, S. Kogan, V. N. Gorshkov, and G. P. Berman, Phys. Rev. B **65**, 245213 (2002).

[14] C. Tahan, M. Friesen, and R. Joynt, Phys. Rev. B **66**, 035314 (2002).

[15] E. Ya. Sherman and D. J. Lockwood, Phys. Rev. B **72**, 125340 (2005).

[16] P. Stano and J. Fabian, Phys. Rev. B. **72**, 155410 (2005).

[17] F. Baruffa, P. Stano, and J. Fabian, Phys. Rev. Lett. **104**, 126401 (2010).

[18] X. Linpeng, T. Karin, M. V. Durnev, R. Barbour, M. M. Glazov, E. Ya. Sherman, S. P. Watkins, S. Seto, and K.-M. C. Fu, Phys. Rev. B **94**, 125401 (2016).

[19] V. N. Stavrou, J. Phys.: Condens. Matter **29**, 485301 (2017).

[20] V. N. Stavrou, J. Phys.: Condens. Matter **30**, 455301 (2018).

[21] Z.-H. Liu, R. Li, X. Hu, and J. Q. You, Sci. Rep. **8**, 2302 (2018).

[22] O. Malkoc, P. Stano, and D. Loss, Phys. Rev. B **93**, 235413 (2016).

[23] J. I. Climente, A. Bertoni, G. Goldoni, M. Rontani, and E. Molinari, Phys. Rev. B **75**, 081303(R) (2007).

[24] D. Chaney and P. A. Maksym, Phys. Rev. B **75**, 035323 (2007).

[25] E. Reyes-Gómez, N. Porras-Montenegro, C. A. Perdomo-Leiva, H. S. Brandi, and L. E. Oliveira, J. Appl. Phys. **104**, 023704 (2008).

[26] H. A. Nilsson, P. Caroff, C. Thelander, M. Larsson, J. B. Wagner, L.-E. Wernersson, L. Samuelson, and H. Q. Xu, Nano Lett. **9**, 3151 (2009).

[27] M. Trif, V. N. Golovach, and D. Loss, Phys. Rev. B **77**, 045434 (2008).

[28] S. Nadj-Perge, S. M. Frolov, E. P. A. M. Bakkers, and L. P. Kouwenhoven, Nature (London) **468**, 1084 (2010).

[29] S. Nadj-Perge, V. S. Pribiag, J. W. G. van den Berg, K. Zuo, S. R. Plissard, E. P. A. M. Bakkers, S. M. Frolov, and L. P. Kouwenhoven, Phys. Rev. Lett. **108**, 166801 (2012).

[30] R. Li, J. Q. You, C. P. Sun, and F. Nori, Phys. Rev. Lett. **111**, 086805 (2013).

[31] R. Li and J. Q. You, Phys. Rev. B **90**, 035303 (2014).

[32] G. Dresselhaus, Phys. Rev. **100**, 580 (1955).

[33] E. I. Rashba, Fiz. Tv. Tela (Leningrad) **2**, 1224 (1960); Sov. Phys. Solid State **2**, 1109 (1960).

[34] M. Raith, P. Stano, and J. Fabian, Phys. Rev. B **83**, 195318 (2011).

[35] M. Raith, P. Stano, and J. Fabian, Phys. Rev. B **86**, 205321 (2012).

[36] S. Wu, L. Cheng, H. Yu, and Q. Wang, Phys. Lett. A **382**, 1922 (2018).

[37] F. N. M. Froning, M. K. Rehmann, J. Ridderbos, M. Brauns, F. A. Zwanenburg, A. Li, E. P. A. M. Bakkers, D. M. Zumbühl, and F. R. Braakman, Appl. Phys. Lett. **113**, 073102 (2018).

[38] D. Fan, S. Li, N. Kang, P. Caroff, L. B. Wang, Y. Q. Huang, M. T. Deng, C. L. Yu, and H. Q. Xu, Nanoscale **7**, 14822 (2015).

[39] M. P. Nowak and B. Szafran, Phys. Rev. B **89**, 205412 (2014).

[40] Z.-H. Liu, O. Entin-Wohlman, A. Aharony, and J. Q. You, Phys. Rev. B **98**, 241303(R) (2018).

[41] M. Cardona, N. E. Christensen, and G. Fasol, Phys. Rev. B **38**, 1806 (1988).

[42] H. A. Nilsson, O. Karlström, M. Larsson, P. Caroff, J. N. Pedersen, L. Samuelson, A. Wacker, L. E. Wernersson, and H. Q. Xu, Phys. Rev. Lett. **104**, 186804 (2010).

[43] Z.-H. Liu and R. Li, AIP Adv. **8**, 075115 (2018).

[44] R. de Sousa and S. Das Sarma, Phys. Rev. B **68**, 155330 (2003).

[45] J. I. Climente, A. Bertoni, G. Goldoni, and E. Molinari, Phys. Rev. B **74**, 035313 (2006).

[46] S. E. Hebboul and J. P. Wolfe, Phys. Rev. B **34**, 3948 (1986).

[47] O. Madelung, Ed., *Intrinsic Properties of Group IV Elements and III-V, II-VI and I-VII Compounds*, Landolt-Bornstein, New Series Vol. 22 (Springer, Berlin, 1987), Chap. 2.15, p. 130.

[48] C. F. Destefani and S. E. Ulloa, Phys. Rev. B **72**, 115326 (2005).

[49] I. M. Tsidilkovskii and K. M. Demchuk, Phys. Status Solidi B **44**, 293 (1971); K. M. Demchuk and I. M. Tsidilkovskii, *ibid.* **82**, 59 (1977); K. Tukioka, Jpn. J. Appl. Phys. **30**, 212 (1991).

[50] J. L. Cheng, M. W. Wu, and C. Lü, Phys. Rev. B **69**, 115318 (2004).

[51] L. C. Camenzind, L. Yu, P. Stano, J. D. Zimmerman, A. C. Gossard, D. Loss, and D. M. Zumbühl, Nat. Commun. **9**, 3454 (2018).

[52] Although dependence of relaxation rates on the magnetic field strength are presented for the special $\theta - \varphi = \pi/2$ magnetic field orientation, conclusion remain valid for different $\theta - \varphi$ angles.

[53] Low fields correspond to weak Zeeman splitting. In this case low temperatures are needed, such that Zeeman splitting is above the thermal broadening; temperature dependence analysis is beyond the scope of the presented work.

[54] P. Stano, C.-H. Hsu, M. Serina, L. C. Camenzind, D. M. Zumbühl, and D. Loss, Phys. Rev. B **98**, 195314 (2018).

[55] B. Fornberg, Math. Comput. **51**, 699 (1988).

Control of a spin qubit in a lateral GaAs quantum dot based on symmetry of gating potential

Pavle Stipsić [1] and Marko Milivojević [2,3]

[1] *Faculty of Physics, University of Belgrade, Studentski trg 12, 11001 Belgrade, Serbia*

[2] *NanoLab, QTP Center, Faculty of Physics, University of Belgrade, Studentski trg 12, 11001 Belgrade, Serbia*

[3] *Department of Theoretical Physics and Astrophysics, Faculty of Science, P. J. Šafárik University, Park Angelinum 9, 040 01 Košice, Slovak Republic*

(Received 14 January 2020; revised manuscript received 25 February 2020; accepted 10 March 2020; published 6 April 2020)

We study the influence of quantum dot symmetry on the Rabi frequency and phonon-induced spin relaxation rate in a single-electron GaAs spin qubit. We find that anisotropic dependence on the magnetic field direction is independent of the choice of the gating potential. Also, we discover that relative orientation of the quantum dot, with respect to the crystallographic frame, is relevant in systems with $\mathbf{C}_{1v}$, $\mathbf{C}_{2v}$, or $\mathbf{C}_n$ ($n \neq 4r$) symmetry. To demonstrate the important impact of the gating potential shape on the spin qubit lifetime, we compare the effects of an infinite-wall equilateral triangle, square, and rectangular confinement with the known results for the harmonic potential. In the studied cases, enhanced spin qubit lifetime is revealed, reaching almost six orders of magnitude increase for the equilateral triangle gating.

DOI: 10.1103/PhysRevB.101.165302

I. INTRODUCTION

Every quantum two-level system can act as the quantum bit, a basic unit of quantum information processing [1,2]. Among different solid-state implementations of the qubit system [3–6], single-electron spin in a semiconductor quantum dot (QD) can be used to achieve the task. In order to manipulate spins of charge carriers embedded inside a semiconductor material electrically, through electric dipole spin resonance (EDSR) [7], the presence of spin-orbit interaction (SOI) is obligatory.

Besides its positive effect in EDSR-based schemes [8–16], SOI enables the electron-phonon coupling-mediated transitions between the qubit states [17–20], affecting the spin qubit lifetime. To suppress the coupling to phonons, different approaches like the optimization of the QD design [21,22] or control of the system size [23] were suggested. The observed anisotropy of the spin relaxation rate on the in-plane magnetic field orientation [24] offered another playground for fine-tuning the spin qubit's desired properties. In circular QDs, this is the only degree of freedom accessible in the optimization of the spin qubit, while for the elliptical confining potential [22,25–27] orientation of the QD potential with respect to the crystallographic frame can be used as the tuning parameter.

Evidently, different symmetry of the gating potential [28] is the main reason for the observed behavior. But to what extent can the potential symmetry alter the basic properties of the electrically controlled spin qubit? To address this question, we have performed a general analysis valid for the lateral GaAs QD system with $\mathbf{C}_{nv}$ or $\mathbf{C}_n$ symmetry of the gating potential. Besides the expected anisotropy on the magnetic field orientation, we were able to find potential symmetries for which the QD orientation with respect to the crystallographic frame can act as another control parameter of the spin qubit characteristics. With our theory, we offer a simple and efficient way to determine the impact of the gating potential on the Rabi frequency and spin relaxation rate. This is shown in the example of anisotropic and isotropic harmonic potential, as well as for the infinite-wall equilateral triangle, square, and rectangular potential.

This paper is organized as follows. In Sec. II we define a single-electron GaAs spin qubit model. In Sec. III we define the dipole moment of the electrically controlled spin qubit that describes both the Rabi frequency and SOI-induced spin relaxation rate mediated by acoustic phonons. In Sec. IV we present the main results of the paper: analytical expressions for the dipole moment in the case of the gating potential with $\mathbf{C}_{nv}$ or $\mathbf{C}_n$ symmetry. In Sec. V, to illustrate the impact of the gating potential on the spin qubit lifetime we use the obtained expressions to compare the influence of the harmonic confinement with an infinite-wall equilateral triangle, square, and rectangular potential. In Sec. VI we give our conclusions.

II. DYNAMICS OF THE LATERAL QD

We start with the Hamiltonian describing the lateral dynamics of a single-electron in the GaAs material,

$$H = H_0 + H_z + H_{so} = \frac{p_x^2 + p_y^2}{2m^*} + V(x,y) + H_z + H_{so}, \quad (1)$$

where p_x and p_y are the momentum operators, m^* is the effective mass ($m^* = 0.067m_e$ for GaAs, m_e is the electron mass), while $V(x,y)$ is the gating potential used to localize the electron in a QD. In the lateral system, symmetries that can be present are the n-fold rotational symmetry and the vertical mirror plane symmetry σ_v. For simplicity, we assume that σ_v coincides with the yz plane of the QD coordinate frame (see Fig. 1). Thus, we assume a general form of the orbital Hamiltonian H_0 that has a $\mathbf{C}_{nv}$ or $\mathbf{C}_n$ ($n = \infty$ also) symmetry.

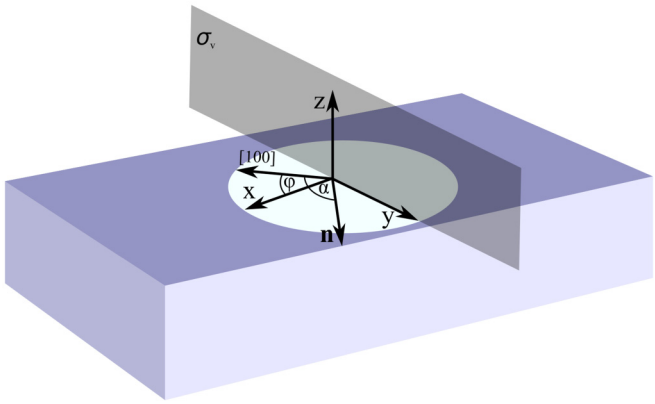

FIG. 1. A schematic view of the GaAs lateral QD. The y axis of the QD reference frame coincides with the vertical mirror plane symmetry σ_v. We define the angle between the chosen x axis and the crystallographic [100] axis as φ. The magnetic field is aligned along the **n** direction, forming an angle α with the [100] direction.

Due to the symmetry, eigenenergies and eigenvectors of H_0 can be classified according to the irreducible representations (IRs) of a given point-group symmetry.

Besides H_0, in Eq. (1) the Zeeman term H_z appears, describing the coupling of spin and magnetic field:

$$H_z = g\mu_B \boldsymbol{B}\cdot\boldsymbol{s}, \tag{2}$$

where g is the effective Landé factor ($g \approx -0.44$ for GaAs), μ_B is the Bohr magneton, $\boldsymbol{s} = 1/2\boldsymbol{\sigma}$ is the electron's spin, and $\boldsymbol{B} = B\boldsymbol{n}$ is the in-plane magnetic field forming an angle α with the crystallographic [100] axis. In Eq. (1) we have neglected the orbital effects of the in-plane magnetic field. This is a reasonable assumption for the magnetic field strength weaker than a few teslas [29]. In the case of the magnetic field applied in the z direction, orbital effects would be much more pronounced [29].

Eigenstates of $H_0 + H_z$ can be written in a direct product form $|\Psi_i\pm\rangle = |\Psi_i\rangle \otimes |\pm\rangle$, where $|\Psi_i\rangle$ corresponds to the eigenvectors of the Hamiltonian H_0 with an energy ϵ_i, while $|\pm\rangle$ represents eigenvectors of H_z with spin projection parallel or antiparallel to the magnetic field direction and an eigenenergy $\pm g\mu_B B/2$, respectively. The effect of H_z on the eigenspectra of H_0 can be seen as the splitting of H_0 eigenenergies into two branches with an energy difference $|g|\mu_B B$. In this work, we assume that $|g|\mu_B B$ is much weaker than the energy difference between the ground and the first excited state of the orbital Hamiltonian H_0.

Besides H_0 (H_z) that acts trivially in the spin (orbital) space, the SOI Hamiltonian does not commute with $H_0 + H_z$. It consists of two terms, Dresselhaus [30] and Rashba [31]: the Dresselhaus term exists due to the bulk inversion asymmetry of the structure, while the Rashba term is present when an electric field perpendicular to the growth direction is applied. The form of spin-orbit coupling is dependent on the structure's symmetry. For GaAs, having the zincblende structure, the SOI Hamiltonian is equal to

$$H_{so} = 2\alpha_d\left(p_y^c s_y - p_x^c s_x\right) + 2\alpha_r\left(p_x^c s_y - p_y^c s_x\right), \tag{3}$$

where α_r and α_d are Rashba and Dresselhaus coupling constants, while p_x^c and p_y^c are momentum operators in the [100] and [010] crystallographic directions, respectively. The electron spin is locked to the crystal momentum, since the potential trap confines electron of the crystal. Thus, an electron in a QD inherits the features of the crystal for which the crystal momentum is only appropriately defined. However, we have the choice to define the x axis of our coordinate frame independently on the crystallographic [100] direction. Assuming that the angle between them is φ, p_x^c and p_y^c should be written in terms of momentum operators in the chosen frame: $p_x^c = p_x\cos\varphi - p_y\sin\varphi$, $p_y^c = p_x\sin\varphi + p_y\cos\varphi$.

The spin-orbit Hamiltonian can be written in a different form using the Rashba $l_r = \hbar^2/2m\alpha_r$ and Dresselhaus $l_d = \hbar^2/2m\alpha_d$ precession lengths:

$$H_{so} = \hbar\left(\frac{p_y^c s_y - p_x^c s_x}{m^* l_d} + \frac{p_x^c s_y - p_y^c s_x}{m^* l_r}\right). \tag{4}$$

To compare the ratio of the spin-orbit precession length and the orbital confinement length l, we redefine l_r and l_d in terms of the overall spin-orbit length l_{so} and the spin-orbit angle ν:

$$l_d^{-1} = l_{so}^{-1}\sin\nu, \quad l_r^{-1} = l_{so}^{-1}\cos\nu. \tag{5}$$

Since we assume no doping of the GaAs material [32], l_{so} can be considered constant. Moreover, the relation $l_{so} \gg l$ [29,33] is satisfied in GaAs QDs, meaning that SOI can be treated as a perturbation.

Without SOI, qubit states can be defined as $|\Psi_0\pm\rangle = |\Psi_0\rangle \otimes |\pm\rangle$, where $|\Psi_0\rangle$ corresponds to the ground state of the spin-independent Hamiltonian H_0. Because SOI can be treated on the level of a perturbation, we calculate first-order corrections of the qubit states due to spin-orbit coupling. Since it is known that the standard perturbation technique badly incorporates the spin-orbit-induced corrections [34,35], we follow the procedure explained in Ref. [22]: the Hamiltonian H is transformed using the unitary operator $U = \exp(i\mathbf{n}_{so}\cdot\boldsymbol{s})$, defined with the help of the position-dependent spin-orbit vector $\mathbf{n}_{so} = l_{so}^{-1}(r_1\sin\nu + r_2\cos\nu, -r_1\cos\nu - r_2\sin\nu, 0)$:

$$UHU^\dagger = H_0 + H_z + H_{so}^{\text{eff}}. \tag{6}$$

The unitary operator U does not change the orbital and Zeeman Hamiltonian. On the other hand, the SOI Hamiltonian H_{so} is transformed into

$$H_{so}^{\text{eff}} = g\mu_B(\mathbf{n}_{so}\times\mathbf{B})\cdot\boldsymbol{s} - \frac{\hbar^2}{4m^* l_{so}^2}(1 + 2l_z s_z\cos 2\nu), \tag{7}$$

where $l_z = -i(r_1\partial_{r_2} - r_2\partial_{r_1})$ is the orbital angular momentum. Using H_{so}^{eff}, the first-order correction of the qubit states can be written as

$$\delta|\Psi_0\sigma'\rangle = U\sum_{i\neq 0,\sigma''}\frac{\langle\Psi_i\sigma''|H_{so}^{\text{eff}}|\Psi_0\sigma'\rangle}{\epsilon_0 - \epsilon_i + \frac{\sigma'-\sigma''}{2}g\mu_B B}|\Psi_i\sigma''\rangle, \tag{8}$$

where the sum over $i \neq 0$ corresponds to all orbital eigenvectors $|\Psi_i\rangle$ different from the ground state $|\Psi_0\rangle$, while $\sigma'' = \pm$.

The lateral QD model is valid if the electron dynamics in the z direction is suppressed; i.e., an electron is always in the ground state. Thus, we assume that confinement length in the z direction is much stronger than in the xy plane. The Hamiltonian describing the quantum confinement in the z

direction is equal to $H(z) = p_z^2/2m^* + V(z)$, where $V(z) = eE_0 z$ for $z \geqslant 0$ and $V(z) = \infty$ for $z < 0$. To this Hamiltonian corresponds the following ground state (for $z > 0$) [36]:

$$\Psi_0(z) = 1.4261\sqrt{\chi}\,\mathrm{Ai}(\chi z - 2.3381), \tag{9}$$

where Ai is the Airy function, while $\chi = (2m^* eE_0/\hbar^2)^{1/3}$ is the inverse of the characteristic length $z_0 = 1.5587/\chi$ in the z direction.

In order to simplify the notation, in the rest of the paper we assume that $|\uparrow\rangle$ and $|\downarrow\rangle$ represent SOI corrected qubit states in the xy plane, while $|\Psi_\uparrow\rangle = |\uparrow\rangle\Psi_0(z)$ and $|\Psi_\downarrow\rangle = |\downarrow\rangle\Psi_0(z)$ correspond to wavefunctions of the qubit states in three dimensions.

III. RABI FREQUENCY AND PHONON-INDUCED SPIN RELAXATION RATE

Electrical control of the spin qubit is possible by applying the in-plane oscillating electric field $\mathbf{E}\cos\omega t$, resulting in the Rabi Hamiltonian $H_\mathrm{R} = e\mathbf{E}\cdot\mathbf{r}\cos(\omega t)$. The Rabi frequency, measuring the speed of the single-qubit rotations, is equal to $\Omega = e/\hbar|\mathbf{E}\cdot\langle\uparrow|\mathbf{r}|\downarrow\rangle|$, where

$$\mathbf{d}_{\uparrow\downarrow} = \langle\uparrow|\mathbf{r}|\downarrow\rangle \tag{10}$$

is the dipole moment (in e units), present due to the SOI-induced spin mixing mechanism. Misalignment of the applied field direction and the dipole moment leads to a trivial suppression of the Rabi frequency. Since it is beneficial to increase the Rabi frequency as much as possible, the electric field should be applied in the direction of the dipole moment. Thus, for fixed $|\mathbf{E}|$, the maximal value $\max(\Omega) = \Omega_{\uparrow\downarrow}$ of the Rabi frequency

$$\Omega_{\uparrow\downarrow} = \frac{e}{\hbar}|\mathbf{E}||\mathbf{d}_{\uparrow\downarrow}| \tag{11}$$

is completely dependent on the strength of the dipole moment.

Since spin-phonon interaction in semiconductor QDs is irrelevant [17], unlike donor-bound electrons in direct band-gap semiconductors [37], only electron-phonon-induced transition between the qubit states should be considered in the study of spin relaxation. Electron-phonon coupling is triggered by the SOI-induced admixture mechanism, being highly dependent on the symmetry of the gating potential [37]. We determine the rate of spin relaxation at $T = 0$ from the Fermi golden rule,

$$\Gamma_{\uparrow\downarrow} = \frac{2\pi}{\hbar}\sum_{\nu\mathbf{q}}|M_\nu(\mathbf{q})|^2|\langle\Psi_\uparrow|e^{i\mathbf{q}\cdot\mathbf{r}_c}|\Psi_\downarrow\rangle|^2\delta(\epsilon_{\uparrow\downarrow} - \hbar\omega_{\nu\mathbf{q}}), \tag{12}$$

assuming the dominant contribution of acoustic phonons, having an energy $\hbar\omega_{\nu\mathbf{q}}$, equal to the level separation between the qubit states, $\epsilon_{\uparrow\downarrow} = |g|\mu_B B$. For magnetic field strengths up to a few teslas, relevant for this work, the linear dependence of phonon frequencies on the crystal wave vector length can be used, $\omega_{\nu\mathbf{q}} = c_\nu|\mathbf{q}|$, giving us $|\mathbf{q}| = |g|\mu_B B/\hbar c_\nu$ [38].

The geometric factor $|M_\nu(\mathbf{q})|^2$ is dependent on the phonon mode, longitudinal acoustic (LA) or transverse acoustic (TA). The longitudinal geometric factor [39]

$$|M_\mathrm{LA}(\mathbf{q})|^2 = \frac{\hbar D^2}{2\rho c_\mathrm{LA} V}|\mathbf{q}| + \frac{32\pi^2\hbar(eh_{14})^2}{\epsilon^2\rho c_\mathrm{LA} V}\frac{(3q_x q_y q_z)^2}{|\mathbf{q}|^7} \tag{13}$$

depends on both D and h_{14}, representing the deformation and piezoelectric constant, respectively. On the other hand, the transverse geometric factor [39]

$$|M_\mathrm{TA}(\mathbf{q})|^2 = 2\frac{32\pi^2\hbar(eh_{14})^2}{\epsilon^2\rho c_\mathrm{TA} V} \times\left|\frac{q_x^2 q_y^2 + q_x^2 q_z^2 + q_y^2 q_z^2}{|\mathbf{q}|^5} - \frac{(3q_x q_y q_z)^2}{|\mathbf{q}|^7}\right| \tag{14}$$

is dependent on the piezoelectric constant solely. Other parameters for the GaAs material are [22,34] $c_\mathrm{LA} = 5290$ m/s, $c_\mathrm{TA} = 2480$ m/s, $\rho = 5300$ kg/m^3, $D = 7$ eV, $eh_{14} = 1.4\times 10^9$ eV/m, and $\epsilon = 12.9$.

Finally, in Eq. (12) both the lateral and the z-direction confinement enter the relaxation rate through the scattering matrix element $|\langle\Psi_\uparrow|e^{i\mathbf{q}\cdot\mathbf{r}_c}|\Psi_\downarrow\rangle|^2$. We employ the dipole approximation $e^{i\mathbf{q}\cdot\mathbf{r}_c} \approx 1 + i\mathbf{q}\cdot\mathbf{r}_c$, justified for magnetic field strengths below a few teslas.

To summarize, the phonon-induced relaxation rate can be divided into three separate channels: the deformation phonons $\Gamma_{\uparrow\downarrow}^\mathrm{def}$, the longitudinal piezoelectric phonons $\Gamma_{\uparrow\downarrow}^\mathrm{piez,LA}$, and the transverse piezoelectric phonons $\Gamma_{\uparrow\downarrow}^\mathrm{piez,TA}$. In GaAs QDs, $\Gamma_{\uparrow\downarrow}^\mathrm{piez,TA}$ is the dominant relaxation channel, being two orders of magnitude stronger than $\Gamma_{\uparrow\downarrow}^\mathrm{piez,LA} + \Gamma_{\uparrow\downarrow}^\mathrm{def}$ in the dipole approximation regime. Thus, we can identify the total relaxation rate with $\Gamma_{\uparrow\downarrow}^\mathrm{piez,TA}$ [40]:

$$\Gamma_{\uparrow\downarrow} = \frac{256\pi(eh_{14})^2(|g|\mu_B B)^3}{105 c_\mathrm{TA}^5\rho\hbar^4\epsilon^2}\left(1 + \frac{7}{33}K_\mathrm{TA}^2 z_0^2\right)|\mathbf{d}_{\uparrow\downarrow}|^2, \tag{15}$$

where $K_\mathrm{TA} = |g|\mu_B B/\hbar c_\mathrm{TA}$. We assume a typical confinement length $l = 10$ nm [29,33] of the GaAs QD in an experimental setup and magnetic field up to a few teslas (see Sec. II). Since confinement in the z direction is much stronger than in the xy plane, $z_0 \ll l$, we conclude that $7K_\mathrm{TA}^2 z_0^2/33$ is much weaker than 1. In other words, the influence of the confinement in the z direction can be neglected.

Note that $\Gamma_{\uparrow\downarrow}$ is squarely dependent on the absolute value of the dipole moment, meaning that the knowledge of the dipole moment is sufficient to fully explain the behavior of both the Rabi frequency and the spin relaxation rate.

IV. ANALYTICAL EXPRESSION FOR THE DIPOLE MOMENT

Based on the previous conclusion, we come to the main objective: to derive symmetry-allowed expression for the dipole moment. The results can be divided into three cases, according to the system's group symmetry: (1) $\mathbf{C}_{n\mathrm{v}}$ ($n \geqslant 3$) and $\mathbf{C}_{\infty\mathrm{v}}$, (2) $\mathbf{C}_{2\mathrm{v}}$ and $\mathbf{C}_{1\mathrm{v}}$, and (3) $\mathbf{C}_n$ and $\mathbf{C}_\infty$.

A. Dipole moment for systems with $\mathbf{C}_{n\mathrm{v}}$ ($n \geqslant 3$) or $\mathbf{C}_{\infty\mathrm{v}}$ symmetry

To find the SOI-induced perturbative correction of the qubit states, we first rewrite the unitarily transformed SOI

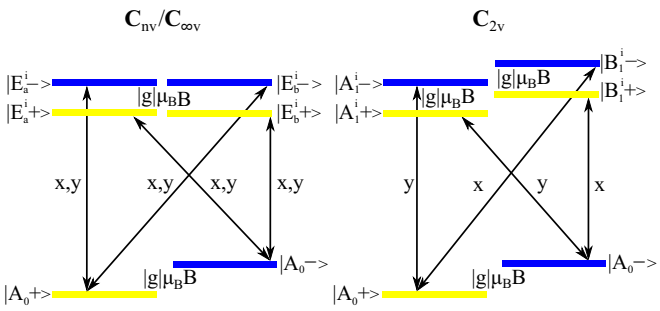

FIG. 2. A schematic view of the first-order perturbation correction of the qubit states $|A_0\pm\rangle$ in the case of $\mathbf{C}_{nv}$ ($\mathbf{C}_{\infty v}$) (left) and $\mathbf{C}_{2v}$ (right) symmetry. In the first case, states that correct the qubit states have twofold orbital degeneracy and transform according to the IR E_1. These states are split by the Zeeman energy $|g|\mu_B B$. The transition between the SOI uncorrected qubit states and the $|E^i_{a,b}\rangle$ states is enabled by the x and y terms from $H^{\rm eff}_{\rm so}$. In the second case, orbital states involved in the qubit states correction transform according to IRs A_1 and B_1; the transition is triggered by the terms y and x from $H^{\rm eff}_{\rm so}$, respectively.

Hamiltonian in the coordinate frame of the potential,

$$H^{\rm eff}_{\rm so} = g\mu_B B s_z (x(\sin(\nu+\varphi)\sin\alpha + \cos(\nu-\varphi)\cos\alpha) + y(\cos(\nu+\varphi)\sin\alpha + \sin(\nu-\varphi)\cos\alpha)), \quad (16)$$

and neglect the second term in Eq. (7), assuming magnetic field strengths $> \mu$T needed to appropriately define the qubit states. For simplicity, we define two factors,

$$v_x = \sin(\nu+\varphi)\sin\alpha + \cos(\nu-\varphi)\cos\alpha, \quad (17)$$

$$v_y = \cos(\nu+\varphi)\sin\alpha + \sin(\nu-\varphi)\cos\alpha, \quad (18)$$

with whose help $H^{\rm eff}_{\rm so}$ can be written in a more compact form.

The Hamiltonian $H^{\rm eff}_{\rm so}$ is in the orbital space dependent on the coordinates x and y that transform according to the IR E_1. Their symmetry behavior restricts the states that can appear in the perturbative correction of the qubit states. It is simple to check that only states transforming according to the IR E_1 are allowed. This is illustrated in the left-hand panel of Fig. 2.

We label the ground state of the orbital Hamiltonian as $|A_0\rangle$, since the ground state in quantum mechanical systems is of the maximal possible symmetry [41] and it should transform according to the A_0 IR, representing the objects invariant under all group symmetry operations (see Table I). We write two complex conjugate basis vectors of the two-dimensional IR E_1 as $|E^i_a\rangle$ and $|E^i_b\rangle$, where i labels the energy level. Also, we define the energy difference between the excited level and the ground state as $\epsilon^i = \epsilon^i_{ex} - \epsilon_{gr}$.

Due to the negative g factor, the lowest qubit state $|A_0+\rangle = |A_0\rangle\otimes|+\rangle$ is parallel to the magnetic field direction, while $|A_0-\rangle = |A_0\rangle\otimes|-\rangle$ is the qubit state with spin projection antiparallel to the magnetic field direction. The first-order perturbative correction to the qubit states is written as $|\delta A_0\pm\rangle$. Thus, we can write the SOI corrected qubit states as $|\uparrow\downarrow\rangle = |A_0\pm\rangle + |\delta A_0\pm\rangle$, where the normalization factor is omitted as the correction is small. Correspondingly, the dipole moment

TABLE I. For $\mathbf{C}_{nv}$ and $\mathbf{C}_{\infty v}$ symmetry groups, tables of matrices of the corresponding IRs are given [42], tabulated on the generators C_n (R_β) and σ_v, where C_n (R_β) represents a rotation for the angle $2\pi/n$ (β) around the z axis. In the $\mathbf{C}_{nv}$ case, two-dimensional IRs exist if $n \geqslant 3$. In both cases, two-dimensional IRs are written in a complex conjugate basis.

$\mathbf{C}_{nv}$	IR	m	C_n	σ_v
	A_0/B_0	0	1	±1
	E_m	$(0, \frac{n}{2})$	$\begin{pmatrix} e^{i\frac{2\pi}{n}m} & 0 \\ 0 & e^{-i\frac{2\pi}{n}m} \end{pmatrix}$	$\begin{pmatrix} 0 & 1 \\ 1 & 0 \end{pmatrix}$
	$A_{\frac{n}{2}}/B_{\frac{n}{2}}$	$\frac{n}{2}$	-1	±1
$\mathbf{C}_{\infty v}$	IR	m	R_β	σ_v
	A_0/B_0	0	1	±1
	E_m	$1, 2, \ldots$	$\begin{pmatrix} e^{i\beta m} & 0 \\ 0 & e^{-i\beta m} \end{pmatrix}$	$\begin{pmatrix} 0 & 1 \\ 1 & 0 \end{pmatrix}$

is equal to

$$\mathbf{d} = \sum_{j=x,y} \langle\uparrow|\mathbf{r}\cdot\boldsymbol{e}_j|\downarrow\rangle \boldsymbol{e}_j = \sum_{j=x,y} (\langle A_0+|\mathbf{r}\cdot\boldsymbol{e}_j|\delta A_0-\rangle \boldsymbol{e}_j + \langle\delta A_0+|\mathbf{r}\cdot\boldsymbol{e}_j|A_0-\rangle \boldsymbol{e}_j). \quad (19)$$

Since $l_{\rm so} \gg l$, we approximate the unitary operator U with I_2, where I_2 is the identity 2×2 matrix. After noticing that $\langle\pm|s_z|\mp\rangle = -1/2$, $\langle\pm|s_z|\pm\rangle = 0$, we find the SOI-induced corrections of the qubit states

$$|\delta A_0\pm\rangle = \frac{|g|\mu_B B}{2l_{\rm so}} \sum_i \left(\frac{\langle E^i_a|xv_x + yv_y|A_0\rangle}{\epsilon^i \pm |g|\mu_B B} |E^i_a\mp\rangle + \frac{\langle E^i_b|xv_x + yv_y|A_0\rangle}{\epsilon^i \pm |g|\mu_B B} |E^i_b\mp\rangle \right). \quad (20)$$

Additionally, transition dipole matrix elements are labeled as

$$X^i = \langle E^i_a|x|A_0\rangle, \quad Y^i = \langle E^i_a|y|A_0\rangle. \quad (21)$$

Since the Zeeman splitting is much smaller than the orbital excitation energies, $|g|\mu_B B \ll \epsilon^i$, the approximation $\epsilon^i \pm |g|\mu_B B \approx \epsilon^i$ can be made. Thus, Eq. (20) is transformed into

$$|\delta A_0\pm\rangle = \frac{|g|\mu_B B}{2l_{\rm so}} \sum_i \left(\frac{X^i v_x + Y^i v_y}{\epsilon^i} |E^i_a\mp\rangle + \frac{(X^i)^* v_x + (Y^i)^* v_y}{\epsilon^i} |E^i_b\mp\rangle \right), \quad (22)$$

where $(X^i)^*$ and $(Y^i)^*$ are the complex conjugates of X^i and Y^i, respectively. Components of the dipole moment can now be written in a more compact form:

$$d_x = \frac{2|g|\mu_B B}{l_{\rm so}} \sum_i \frac{|X^i|^2 v_x + {\rm Re}(X^i(Y^i)^*)v_y}{\epsilon^i},$$
$$d_y = \frac{2|g|\mu_B B}{l_{\rm so}} \sum_i \frac{|Y^i|^2 v_y + {\rm Re}(X^i(Y^i)^*)v_x}{\epsilon^i}, \quad (23)$$

where ${\rm Re}(X^i(Y^i)^*)$ stands for the real part of $X^i(Y^i)^*$. Potential dependent parameters that enter Eq. (23) are the transition dipole matrix elements and the excitation energies. Besides

them, dipole moment components are dependent on the spin-orbit angle ν, magnetic field angle α, and the angle φ between the [100] crystallographic direction and the x axis.

A further simplification of Eq. (23) stems from the existence of the vertical mirror symmetry σ_v, requiring that $\mathrm{Re}(X^i(Y^i)^*)$ must be zero. This can be proven in a few simple steps. First, we deduce from the matrix of an IR E_1, representing the vertical mirror plane, that σ_v transforms one IR vector into the other, $E_1(\sigma_v)|E^i_{a,b}\rangle = |E^i_{b,a}\rangle$. Furthermore, y remains unchanged, while x acquires a minus sign, leading to the following behavior of the transition matrix elements X^i and Y^i under vertical mirror plane symmetry:

$$X^i \xrightarrow{\sigma_v} -(X^i)^*, \quad Y^i \xrightarrow{\sigma_v} (Y^i)^*. \tag{24}$$

From the previous relations, we conclude that the term $\mathrm{Re}(X^i(Y^i)^*)$ transforms into $-\mathrm{Re}(X^i(Y^i)^*)$, meaning that this object does not obey the symmetry of a system and must vanish.

Additionally, rotational symmetry of a system imposes that matrix elements $|X^i|^2$ and $|Y^i|^2$ are equal. This can be concluded from the action of the rotation C_n for an angle $\beta_n = 2\pi/n$ around the z axis, being the element of the group symmetry. An element C_n leaves the vector $|A_0\rangle$ unchanged and adds a phase $\exp(\mathrm{i}\beta_n)$ to the vector $|E^i_a\rangle$. Also, it transforms x and y to $x\cos\beta_n + y\sin\beta_n$ and $-x\sin\beta_n + y\cos\beta_n$. Thus, X^i and Y^i are transformed into $\exp(-\mathrm{i}\beta_n)(X^i\cos\beta_n + Y^i\sin\beta_n)$ and $\exp(-\mathrm{i}\beta_n)(-X^i\sin\beta_n + Y^i\cos\beta_n)$, respectively. Correspondingly,

$$\begin{aligned} |X^i|^2 &\xrightarrow{C_n} |X^i|^2\cos^2\beta_n + |Y^i|^2\sin^2\beta_n, \\ |Y^i|^2 &\xrightarrow{C_n} |X^i|^2\sin^2\beta_n + |Y^i|^2\cos^2\beta_n, \end{aligned} \tag{25}$$

where we have neglected the $\mathrm{Re}(X^i(Y^i)^*)$ term, which was previously proven to equal to zero. Since $|X^i|^2$ and $|Y^i|^2$ must remain unchanged under the group symmetry operations, we conclude that the relation $|X^i|^2 = |Y^i|^2$ must hold. Thus, we have obtained a general relation for the dipole moment in the case of the potential symmetry $\mathbf{C}_{n\mathrm{v}}$ ($n \geqslant 3$):

$$\mathbf{d}^{\mathbf{C}_{n\mathrm{v}}}_{\uparrow\downarrow} = \frac{2|g|\mu_B B}{l_{\mathrm{so}}}\left(\sum_i \frac{|X^i|^2}{\epsilon^i}\right)(v_x\mathbf{e}_x + v_y\mathbf{e}_y). \tag{26}$$

In these situations, the absolute value of the dipole moment $|\mathbf{d}^{\mathbf{C}_{n\mathrm{v}}}_{\uparrow\downarrow}|^2 \sim (1 + \sin 2\alpha \sin 2\nu)$ is independent of the orientation of the potential with respect to the crystallographic frame.

Analogous analysis can be conducted in the $\mathbf{C}_{\infty\mathrm{v}}$ case. Since the matrix form of the IRs A_0 and E_1 (see Table I) for this symmetry group is the same as for $\mathbf{C}_{n\mathrm{v}}$, the procedure is exactly the same if the change $\beta_n \to \beta$ in the previous discussion is made.

As an example, we implement the derived formula (26) in the case of the isotropic two-dimensional harmonic confinement $V^{\mathrm{iho}}(x,y) = 1/2m^*\omega^2(x^2+y^2)$ with $\mathbf{C}_{\infty\mathrm{v}}$ symmetry, assuming only one excited level in the perturbative correction of the qubit states. With the help of the states ψ_0 and ψ_1, corresponding to the ground and the first excited states of the one-dimensional harmonic oscillator, we can define the ground state $|A_0\rangle$ and two complex conjugate eigenstates $|E_a\rangle$ and $|E_b\rangle$ of the degenerate level: $|A_0\rangle = \psi_0(x)\psi_0(y)$, $|E_a\rangle = (\psi_0(x)\psi_1(y) + \mathrm{i}\psi_1(x)\psi_0(y))/\sqrt{2}$, and $|E_b\rangle = (\psi_0(x)\psi_1(y) - \mathrm{i}\psi_1(x)\psi_0(y))/\sqrt{2}$. In this case, the squared norm of the transition matrix element is equal to $|X|^2 = \hbar/4m^*\omega$. Using the energy difference of the ground and the first excited energy level $\epsilon = \hbar\omega$ and the confinement length $l = \sqrt{\hbar/m^*\omega}$, an expression for the dipole moment is obtained [22]:

$$\mathbf{d}^{\mathrm{iho}}_{\uparrow\downarrow} = \frac{|g|\mu_B B m^* l^4}{2l_{\mathrm{so}}\hbar^2}(v_x\mathbf{e}_x + v_y\mathbf{e}_y). \tag{27}$$

B. Dipole moment for systems with $\mathbf{C}_{2\mathrm{v}}$ or $\mathbf{C}_{1\mathrm{v}}$ symmetry

As the next step, we discuss potentials with $\mathbf{C}_{2\mathrm{v}}$ symmetry. In this case, coordinates x and y transform according to the IRs B_1 and A_1, respectively. Their symmetry behavior imposes the following: x (y) couples the ground state $|A_0\rangle$ with states transforming according to the IR B_1 (A_1) (see the right-hand panel of Fig. 2). Thus, the SOI-induced corrections of the qubit states are

$$\begin{aligned} |\delta A_0 \pm\rangle = \frac{|g|\mu_B B}{2l_{\mathrm{so}}}\sum_i \Bigg(&\frac{\langle B^i_1|xv_x|A_0\rangle}{\epsilon^i_{B_1}}|B^i_1 \mp\rangle \\ &+ \frac{\langle A^i_1|yv_y|A_0\rangle}{\epsilon^i_{A_1}}|A^i_1 \mp\rangle\Bigg), \end{aligned} \tag{28}$$

where $\epsilon^i_{B_1}$ ($\epsilon^i_{A_1}$) is the energy difference between the energy level transforming according to the IR B_1 (A_1) and the ground-state energy. We define the transition matrix elements as

$$X^i = \langle B^i_1|x|A_0\rangle, \; Y^i = \langle A^i_1|y|A_0\rangle, \tag{29}$$

and obtain the formula for the dipole moment,

$$\mathbf{d}^{\mathbf{C}_{2\mathrm{v}}}_{\uparrow\downarrow} = \frac{|g|\mu_B B}{l_{\mathrm{so}}}\sum_i\left(\frac{|X^i|^2}{\epsilon^i_{B_1}}v_x\mathbf{e}_x + \frac{|Y^i|^2}{\epsilon^i_{A_1}}v_y\mathbf{e}_y\right). \tag{30}$$

In this case, anisotropy of the dipole moment appears since it is not forbidden that $\sum_i |X^i|^2/\epsilon^i_{B_1}$ differs from $\sum_i |Y^i|^2/\epsilon^i_{A_1}$.

The anisotropy of the dipole moment can be illuminated using the example of the anisotropic two-dimensional harmonic potential $V^{\mathrm{aho}}(x,y) = 1/2m^*(\omega_x^2x^2 + \omega_y^2y^2)$, with different confinement lengths $l_x = \sqrt{\hbar/m^*\omega_x}$ and $l_y = \sqrt{\hbar/m^*\omega_y}$ along the x and y directions. We set $l = l_x$ and $l_y = kl$, where $k < 1$ is the measure of anisotropy. We assume two excited orbital states in the perturbative correction: one of type A_1 and one of type B_1. In this case we define the ground state $|A_0\rangle = \psi_0(x)\psi_0(y)$ and two excited orbital states $|A_1\rangle = \psi_0(x)\psi_1(y)$ and $|B_1\rangle = \psi_1(x)\psi_0(y)$, where $\psi_{0/1}(x/y)$ represents the ground or first excited state (subscript 0 or 1, respectively) of the one-dimensional harmonic oscillator problem in the x or y direction. The obtained result

$$\mathbf{d}^{\mathrm{aho}}_{\uparrow\downarrow} = \frac{|g|\mu_B B m^* l^4}{2l_{\mathrm{so}}\hbar^2}(v_x\mathbf{e}_x + k^4v_y\mathbf{e}_y) \tag{31}$$

is again consistent with Ref. [22].

In the case of the $\mathbf{C}_{1\mathrm{v}}$ symmetry, using a similar analysis as in the previous case, we obtain the expression for the dipole moment,

$$\mathbf{d}^{\mathbf{C}_{1\mathrm{v}}}_{\uparrow\downarrow} = \frac{|g|\mu_B B}{l_{\mathrm{so}}}\sum_i\left(\frac{|X^i|^2}{\epsilon^i_{B_0}}v_x\mathbf{e}_x + \frac{|Y^i|^2}{\epsilon^i_{A_0}}v_y\mathbf{e}_y\right), \tag{32}$$

where $X^i = \langle B_0^i|x|A_0\rangle$, $Y^i = \langle A_0^i|y|A_0\rangle$, and $\epsilon^i_{A_0/B_0}$ is the energy difference between the nondegenerate energy level transforming according to the IR A_0/B_0 and the ground-state energy.

C. Dipole moment for systems with C_n or C_∞ symmetry

In the case of $\mathbf{C}_n$ symmetry, all IRs A_m ($m \in (-n/2, n/2]$) are one dimensional and represent an element of symmetry C_n^s ($s = 0, 1, \ldots, n-1$) as $e^{i2\pi ms/n}$. Besides the geometric symmetry, the time-reversal symmetry Θ should be included also [43]. Time-reversal Θ changes the sign of the quantum number m labeling the IR vector $|A_m\rangle$, since it acts as a complex conjugation in the orbital space:

$$\Theta|A_m\rangle = |A_{-m}\rangle. \tag{33}$$

The eigenproblem of the Hamiltonian $H|A_m\rangle = \epsilon_m|A_m\rangle$, when combined with the commutation relation $[\Theta, H_0] = 0$, gives us

$$H|A_{-m}\rangle = \epsilon_m|A_{-m}\rangle, \tag{34}$$

stating that, for $n \geqslant 3$, vectors $|A_m\rangle$ and $|A_{-m}\rangle$ are eigenstates of the degenerate level ϵ_m. To this degenerate level corresponds the reducible representation $A_m \oplus A_{-m}$ (except for $m = n/2$). The representation $A_m \oplus A_{-m}$ is equivalent to the IR E_m of the $\mathbf{C}_{n\mathrm{v}}$ group (see Table I) if the generator σ_v is neglected. In other words, Eq. (23) for the dipole moment is valid also in this case, since it is obtained without assuming the presence of vertical mirror symmetry. In this case vectors $|E_a^i\rangle$ and $|E_b^i\rangle$ coincide with $|A_1^i\rangle$ and $|A_{-1}^i\rangle$, respectively.

A further simplification of Eq. (23) appears for systems whose symmetry element is $\pi/2$ rotation. This happens if the relation $n = 4r$ ($r \in \mathbb{N}$) is satisfied. Since $\mathrm{Re}(X^i(Y^i)^*) = 0$ and $|X^i|^2 = |Y^i|^2$ in this case, Eq. (26) is relevant. Using the same reasoning it can be concluded that Eq. (26) is valid in the $\mathbf{C}_\infty$ case also.

Finally, the dipole moment components for the $\mathbf{C}_2$ symmetry are equal to

$$(\mathbf{d}^{\mathbf{C}_2}_{\uparrow\downarrow})_x = \frac{|g|\mu_B B}{l_\mathrm{so}} \sum_i \frac{|X^i|^2 v_x + \mathrm{Re}(X^i(Y^i)^*)v_y}{\epsilon^i_{A_1}},$$
$$(\mathbf{d}^{\mathbf{C}_2}_{\uparrow\downarrow})_y = \frac{|g|\mu_B B}{l_\mathrm{so}} \sum_i \frac{|Y^i|^2 v_y + \mathrm{Re}(X^i(Y^i)^*)v_x}{\epsilon^i_{A_1}}, \tag{35}$$

where $X^i = \langle A_1^i|x|A_0\rangle$, $Y^i = \langle A_1^i|y|A_0\rangle$, and $\epsilon^i_{A_1}$ is the energy difference between the level transforming according to the IR A_1 and the ground-state energy.

To conclude, anisotropy of the potential orientation with respect to the crystallographic frame is present in systems without the $\pi/2$ group element ($n \neq 4r$, $r \in \mathbb{N}$); isotropic behavior is present if a rotation for $\pi/2$ is the group element, i.e., if $n = 4r$ ($r \in \mathbb{N}$) or $n = \infty$.

V. APPLICATIONS: INFINITE-WALL EQUILATERAL TRIANGLE, SQUARE, AND RECTANGULAR POTENTIAL

The results presented in the previous section fully explain the dependence of the Rabi frequency and spin relaxation rate on the spin-orbit angle, magnetic field direction, and the relative orientation of the gating potential with respect to the crystallographic frame.

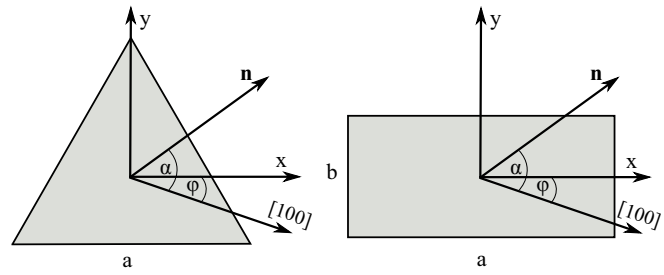

FIG. 3. Infinite-wall equilateral triangle (left) and rectangular (right) gating potential. In both cases, potential is zero inside the area of the polygon; otherwise it is ∞.

However, symmetry arguments alone cannot provide us with a qualitative estimation of the spin relaxation rate, corresponding to the phonon-allowed spin qubit lifetime. Since $\Gamma_{\uparrow\downarrow}$ is known for the harmonic gating [22], we wish to compare the phonon-induced spin relaxation rate of other confinement potentials with the known values. To this end, we analyze the spin qubit confined inside the infinite-wall equilateral triangle, square, and rectangular gating potential (see Fig. 3):

$$V^\mathrm{tqd} = \begin{cases} 0 & \text{for } x \in \left[\frac{y\sqrt{3}-a}{3}, \frac{a-y\sqrt{3}}{3}\right],\ y \in \left[\frac{-a\sqrt{3}}{6}, \frac{a\sqrt{3}}{3}\right] \\ \infty & \text{otherwise,} \end{cases} \tag{36}$$

$$V^\mathrm{rqd} = \begin{cases} 0 & \text{for } x \in \left[-\frac{a}{2}, \frac{a}{2}\right],\ y \in \left[-\frac{b}{2}, \frac{b}{2}\right] \\ \infty & \text{otherwise.} \end{cases} \tag{37}$$

In the first case, Eq. (36), the potential has $\mathbf{C}_{3\mathrm{v}}$ symmetry and the corresponding eigenvectors of the spin-independent Hamiltonian H_0 transform according to the one-dimensional IRs A_0 and B_0 and two-dimensional E_1 IR of the $\mathbf{C}_{3\mathrm{v}}$ group. The set of eigenenergies $\epsilon^\mathrm{tqd}_{p,q}$ and eigenvectors $\psi^{A_0}_{p,q}$, $\psi^{B_0}_{p,q}$, and $\psi^{E_1\pm}_{p,q}$ [44] are dependent on two parameters p and q that have different sets of allowed values for each IR. Their concrete form is given in Appendix A.

In the second case, Eq. (37), the symmetry of the potential is dependent on the ratio $k = b/a \in (0, 1]$: if $k = 1$, the symmetry of the problem is $\mathbf{C}_{4\mathrm{v}}$; otherwise, $\mathbf{C}_{2\mathrm{v}}$ is the symmetry of the spin-independent Hamiltonian H_0. In both situations, eigenenergies and eigenvalues can be found by using the separation of variables. The set of eigenenergies $\epsilon^\mathrm{rqd}_{p,q}$ and eigenvectors $\psi^\mathrm{rqd}_{p,q}$ in this case is

$$\epsilon^\mathrm{rqd}_{p,q} = \frac{\hbar^2\pi^2}{2m^*a^2}\left(p^2 + \frac{q^2}{k^2}\right), \tag{38}$$

$$\psi^\mathrm{rqd}_{p,q} = \frac{2}{a\sqrt{k}} \sin\left[\frac{p\pi}{a}\left(x + \frac{a}{2}\right)\right] \sin\left[\frac{q\pi}{ak}\left(y + \frac{ka}{2}\right)\right], \tag{39}$$

defined using the two independent parameters $p \geqslant 1$ and $q \geqslant 1$ that take integer values. However, these solutions do not have any definite symmetry [45]. Therefore, they need to be symmetrized to apply the general results from Sec. IV. Symmetry-adapted eigenfunctions can be found in Appendix B.

After calculating the transition dipole matrix element and the excitation energies for two excited states in the perturbative correction [46], we obtain the desired results

$$\mathbf{d}^{\mathrm{tqd}}_{\uparrow\downarrow} = \frac{3^{24}}{2^{26}35^2\pi^8}\frac{|g|\mu_B B m^* a^4}{l_{\mathrm{so}}\hbar^2}(v_x\boldsymbol{e}_x + v_y\boldsymbol{e}_y), \tag{40}$$

$$\mathbf{d}^{\mathrm{rqd}}_{\uparrow\downarrow} = \frac{2^9}{3^5\pi^6}\frac{|g|\mu_B B m^* a^4}{l_{\mathrm{so}}\hbar^2}(v_x\boldsymbol{e}_x + k^4 v_y\boldsymbol{e}_y), \tag{41}$$

where the first result corresponds to the infinite-wall equilateral triangle potential, while the second one is valid for both the infinite-wall square, $k = 1$, and rectangular, $k \neq 1$, potentials. Dipole moment constants $3^{24}/2^{26}35^2\pi^8 \approx 3.6 \times 10^{-4}$ and $2^9/3^5\pi^6 \approx 2.2 \times 10^{-3}$ from Eqs. (40) and (41) suggest a much weaker dipole moment when compared to the harmonic gating of the same confinement length [see Eqs. (27) and (31)].

Using the relation $\Gamma_{\uparrow\downarrow} \approx |\mathbf{d}_{\uparrow\downarrow}|^2$, we conclude that square and rectangular confined QDs have a relaxation rate that is four orders of magnitude weaker than the harmonic potential; in the equilateral triangle case, a decrease of almost six orders of magnitude is observed. Thus, our result indicates a significant influence of the gating potential on the spin qubit lifetime and a beneficial role of the equilateral triangle confinement.

VI. CONCLUSIONS

We have investigated the influence of the gating potential symmetry on the Rabi frequency and phonon-induced spin relaxation rate in a single-electron GaAs quantum dot. Our results suggest that, independently of the symmetry of the gating potential, both the Rabi frequency and spin relaxation rate are dependent on the orientation of the magnetic field and the spin-orbit angle. Additionally, in systems with $\mathbf{C}_{1\mathrm{v}}$, $\mathbf{C}_{2\mathrm{v}}$, and $\mathbf{C}_n$ ($n \neq 4r$) symmetry, orientation of the quantum dot potential with respect to the crystallographic reference frame is another degree of freedom that can be used to tune the desired properties of the system. The validity of the approach is confirmed on the known results for the isotropic and anisotropic harmonic potential. Additionally, we have compared the spin qubit lifetime in the case of an infinite-wall rectangular, square, and equilateral triangle gating with the harmonic confinement. Our results indicate the enhanced lifetime of the spin qubit, reaching an almost six-order-of-magnitude increase in the case of the equilateral triangle gating. In the end, we emphasize that in the regime of strong electric field, nonlinear effects [47–49] cannot be fully explained by the symmetry of the gating potential, thus placing the conclusions of our work in the weak driving regime solely.

ACKNOWLEDGMENTS

We thank Nenad Vukmirović for fruitful discussion. This research is funded by the Serbian Ministry of Science (Project No. ON171035) and the National Scholarship Programme of the Slovak Republic (ID 28226).

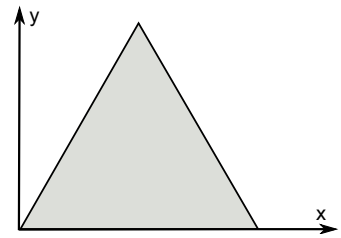

FIG. 4. Infinite-wall equilateral triangle potential with the point group symmetry $\mathbf{C}_{3\mathrm{v}}$. Inside the equilateral triangle potential is 0, otherwise it is ∞.

APPENDIX A: PARTICLE IN THE INFINITE-WALL EQUILATERAL TRIANGLE POTENTIAL: EIGENENERGIES AND EIGENVECTORS

Here we summarize the results from Ref. [44] regarding the Schrödinger equation solution of the particle in the infinite-wall equilateral triangle potential, having $\mathbf{C}_{3\mathrm{v}}$ symmetry. Due to the symmetry, eigenvectors transform according to the one-dimensional IRs A_0 and B_0 and the two-dimensional IR E_1. The concrete forms of eigenenergies and eigenstates,

$$\epsilon^{\mathrm{tqd}}_{p,q} = \frac{8\hbar^2\pi^2}{3m^*a^2}(p^2 + pq + q^2), \tag{A1}$$

$$\begin{aligned}\psi^{A_0}_{p,q}(x,y) = &\cos\left[\frac{2\pi q}{a}x\right]\sin\left[\frac{2\pi(2p+q)}{a\sqrt{3}}y\right] \\ &- \cos\left[\frac{2\pi p}{a}x\right]\sin\left[\frac{2\pi(p+2q)}{a\sqrt{3}}y\right] \\ &- \cos\left[\frac{2\pi(p+q)}{a}x\right]\sin\left[\frac{2\pi(p-q)}{a\sqrt{3}}y\right],\end{aligned}$$

$$q = 0, 1, 2, \ldots, \quad p = q+1, q+2, \ldots, \tag{A2}$$

$$\begin{aligned}\psi^{B_0}_{p,q}(x,y) = &\sin\left[\frac{2\pi q}{a}x\right]\sin\left[\frac{2\pi(2p+q)}{a\sqrt{3}}y\right] \\ &- \sin\left[\frac{2\pi p}{a}x\right]\sin\left[\frac{2\pi(p+2q)}{a\sqrt{3}}y\right] \\ &+ \sin\left[\frac{2\pi(p+q)}{a}x\right]\sin\left[\frac{2\pi(p-q)}{a\sqrt{3}}y\right],\end{aligned}$$

$$q = 1, 2, 3, \ldots, \quad p = q+1, q+2, \ldots, \tag{A3}$$

$$\begin{aligned}\psi^{E_1\pm}_{p,q}(x,y) &= \psi^{B_0}_{p,q}(x,y) \pm \mathrm{i}\psi^{A_0}_{p,q}(x,y), \\ q &= \frac{1}{3}, \frac{2}{3}, \frac{4}{3}, \frac{5}{3}, \ldots, \quad p = q+1, q+2, \ldots,\end{aligned} \tag{A4}$$

are dependent on two parameters p and q that have different allowed values for each IR. Note that the coordinate frame used to derive the previous equations (see Fig. 4) differs from the frame used in our work (see the left-hand panel of Fig. 3). To adapt the eigenfunction from Eqs. (A2)–(A4) to our case, a suitable change of coordinates $x \to x + a/2$ and $y \to y + a\sqrt{3}/6$ should be made.

APPENDIX B: PARTICLE IN THE INFINITE-WALL SQUARE AND RECTANGULAR POTENTIAL: EIGENVECTORS

The infinite-wall square potential has $\mathbf{C}_{4v}$ symmetry with the corresponding IRs A_0/B_0, A_2/B_2, and E_1. Eigenvectors that transform according to the given IRs and the set of allowed quantum numbers are

$$\psi^{A_0}_{p,q}(x,y) = \cos\left[\frac{p\pi}{a}x\right]\cos\left[\frac{q\pi}{a}y\right] + \cos\left[\frac{q\pi}{a}x\right]\cos\left[\frac{p\pi}{a}y\right], \quad q = 1,3,5,\ldots, \quad p = q, q+2, q+4,\ldots, \tag{B1}$$

$$\psi^{B_0}_{p,q}(x,y) = \sin\left[\frac{p\pi}{a}x\right]\sin\left[\frac{q\pi}{a}y\right] - \sin\left[\frac{q\pi}{a}x\right]\sin\left[\frac{p\pi}{a}y\right], \quad q = 2,4,6,\ldots, \quad p = q+2, q+4,\ldots, \tag{B2}$$

$$\psi^{A_2}_{p,q}(x,y) = \cos\left[\frac{p\pi}{a}x\right]\cos\left[\frac{q\pi}{a}y\right] - \cos\left[\frac{q\pi}{a}x\right]\cos\left[\frac{p\pi}{a}y\right], \quad q = 1,3,5,\ldots, \quad p = q+2, q+4,\ldots, \tag{B3}$$

$$\psi^{B_2}_{p,q}(x,y) = \sin\left[\frac{p\pi}{a}x\right]\sin\left[\frac{q\pi}{a}y\right] + \sin\left[\frac{q\pi}{a}x\right]\sin\left[\frac{p\pi}{a}y\right], \quad q = 2,4,6,\ldots, \quad p = q, q+2, q+4,\ldots, \tag{B4}$$

$$\psi^{E_1\pm}_{p,q}(x,y) = \cos\left[\frac{p\pi}{a}x\right]\sin\left[\frac{q\pi}{a}y\right] \pm i\sin\left[\frac{q\pi}{a}x\right]\cos\left[\frac{p\pi}{a}y\right], \quad p = 1,3,5,\ldots, \quad q = p+1, p+3,\ldots. \tag{B5}$$

In the case of the infinite-wall rectangular potential $\mathbf{C}_{2v}$ symmetry is relevant. Eigenfunctions transforming according to the IRs A_0/B_0 and A_1/B_1 and the corresponding set of quantum numbers are

$$\psi^{A_0}_{p,q}(x,y) = \cos\left[\frac{p\pi}{a}x\right]\cos\left[\frac{q\pi}{ka}y\right], \quad q = 1,3,5,\ldots, \quad p = q, q+2, q+4,\ldots, \tag{B6}$$

$$\psi^{B_0}_{p,q}(x,y) = \sin\left[\frac{p\pi}{a}x\right]\sin\left[\frac{q\pi}{ka}y\right], \quad q = 2,4,6,\ldots, \quad p = q, q+2, q+4,\ldots, \tag{B7}$$

$$\psi^{A_1}_{p,q}(x,y) = \cos\left[\frac{p\pi}{a}x\right]\sin\left[\frac{q\pi}{ka}y\right], \quad p = 1,3,5,\ldots, \quad q = p+1, p+3, p+5,\ldots, \tag{B8}$$

$$\psi^{B_1}_{p,q}(x,y) = \sin\left[\frac{p\pi}{a}x\right]\cos\left[\frac{q\pi}{ka}y\right], \quad q = 1,3,5,\ldots, \quad p = q+1, q+3, q+5,\ldots. \tag{B9}$$

In both cases, eigenenergies are given in Eq. (38) ($k = 1$ in the $\mathbf{C}_{4v}$ case and $k \neq 1$ for the $\mathbf{C}_{2v}$ symmetry).

[1] M. A. Nielsen and I. L. Chuang, *Quantum Computation and Quantum Information* (Cambridge University Press, Cambridge, UK, 2010).

[2] C. H. Bennett and D. P. DiVincenzo, Nature (London) **404**, 247 (2000).

[3] D. Loss and D. P. DiVincenzo, Phys. Rev. A **57**, 120 (1998).

[4] T. P. Orlando, J. E. Mooij, L. Tian, C. H. van der Wal, L. S. Levitov, S. Lloyd, and J. J. Mazo, Phys. Rev. B **60**, 15398 (1999).

[5] Y. Nakamura, Yu. A. Pashkin, and J. S. Tsai, Nature (London) **398**, 786 (1999).

[6] M. Yamamoto, S. Takada, C. Bäuerle, K. Watanabe, A. D. Wieck, and S. Tarucha, Nat. Nanotechnol. **7**, 247 (2012).

[7] E. I. Rashba, Sov. Phys. Solid State **2**, 1109 (1960).

[8] V. N. Golovach, M. Borhani, and D. Loss, Phys. Rev. B **74**, 165319 (2006).

[9] D. V. Bulaev and D. Loss, Phys. Rev. Lett. **98**, 097202 (2007).

[10] K. C. Nowack, F. H. L. Koppens, Yu. V. Nazarov, and L. M. K. Vandersypen, Science **318**, 1430 (2007).

[11] E. I. Rashba, Phys. Rev. B **78**, 195302 (2008).

[12] R. Brunner, Y.-S. Shin, T. Obata, M. Pioro-Ladrière, T. Kubo, K. Yoshida, T. Taniyama, Y. Tokura, and S. Tarucha, Phys. Rev. Lett. **107**, 146801 (2011).

[13] E. Kawakami, P. Scarlino, D. R. Ward, F. R. Braakman, D. E. Savage, M. G. Lagally, Mark Friesen, S. N. Coppersmith, M. A. Eriksson, and L. M. K. Vandersypen, Nat. Nanotechnol. **9**, 666 (2014).

[14] K. Takeda, J. Yoneda, T. Otsuka, T. Nakajima, M. R. Delbecq, G. Allison, Y. Hoshi, N. Usami, K. M. Itoh, S. Oda, T. Kodera, and S. Tarucha, npj Quantum Inf. **4**, 54 (2018).

[15] D. V. Khomitsky, E. A. Lavrukhina, and E. Y. Sherman, Phys. Rev. B **99**, 014308 (2019).

[16] S. Studenikin, M. Korkusinski, M. Takahashi, J. Ducatel, A. Padawer-Blatt, A. Bogan, D. Guy Austing, L. Gaudreau, P. Zawadzki, A. Sachrajda, Y. Hirayama, L. Tracy, J. Reno, and T. Hargett, Commun. Phys. **2**, 159 (2019).

[17] A. V. Khaetskii and Y. V. Nazarov, Phys. Rev. B **61**, 12639 (2000); **64**, 125316 (2001).

[18] P. Stano and J. Fabian, Phys. Rev. B **72**, 155410 (2005).

[19] V. N. Stavrou, J. Phys.: Condens. Matter **29**, 485301 (2017); **30**, 455301 (2018).

[20] Z.-H. Liu, R. Li, X. Hu, and J. Q. You, Sci. Rep. **8**, 2302 (2018).

[21] J. I. Climente, A. Bertoni, G. Goldoni, M. Rontani, and E. Molinari, Phys. Rev. B **75**, 081303(R) (2007).

[22] O. Malkoc, P. Stano, and D. Loss, Phys. Rev. B **93**, 235413 (2016).

[23] D. Chaney and P. A. Maksym, Phys. Rev. B **75**, 035323 (2007).

[24] V. I. Fal'ko, B. L. Altshuler, and O. Tsyplyatyev, Phys. Rev. Lett. **95**, 076603 (2005).

[25] P. Scarlino, E. Kawakami, P. Stano, M. Shafiei, C. Reichl, W. Wegscheider, and L. M. K. Vandersypen, Phys. Rev. Lett. **113**, 256802 (2014).

[26] O. Olendski and T. V. Shahbazyan, Phys. Rev. B **75**, 041306(R) (2007).

[27] S. Amasha, K. MacLean, I. P. Radu, D. M. Zumbühl, M. A. Kastner, M. P. Hanson, and A. C. Gossard, Phys. Rev. Lett. **100**, 046803 (2008).

[28] J. Planelles, F. Rajadell, and J. I. Climente, Phys. Rev. B **92**, 041302(R) (2015).

[29] M. Raith, P. Stano, and J. Fabian, Phys. Rev. B **83**, 195318 (2011).
[30] G. Dresselhaus, Phys. Rev. **100**, 580 (1955).
[31] E. I. Rashba, Fiz. Tverd. Tela (Leningrad) **2**, 1224 (1960) [Sov. Phys. Solid State **2**, 1109 (1960)].
[32] E. Ya. Sherman and D. J. Lockwood, Phys. Rev. B **72**, 125340 (2005).
[33] M. Raith, T. Pangerl, P. Stano, and J. Fabian, Phys. Status Solidi B **251**, 1924 (2014).
[34] J. L. Cheng, M. W. Wu, and C. Lü, Phys. Rev. B **69**, 115318 (2004).
[35] F. Baruffa, P. Stano, and J. Fabian, Phys. Rev. Lett. **104**, 126401 (2010).
[36] R. de Sousa and S. Das Sarma, Phys. Rev. B **68**, 155330 (2003).
[37] X. Linpeng, T. Karin, M. V. Durnev, R. Barbour, M. M. Glazov, E. Ya. Sherman, S. P. Watkins, S. Seto, and K.-M. C. Fu, Phys. Rev. B **94**, 125401 (2016).
[38] Note that both the wave vector $\mathbf{q}$ and the electron coordinate $\mathbf{r}_c$ are written in the crystallographic reference frame.
[39] J. I. Climente, A. Bertoni, G. Goldoni, and E. Molinari, Phys. Rev. B **74**, 035313 (2006).
[40] L. C. Camenzind, L. Yu, P. Stano, J. D. Zimmerman, A. C. Gossard, D. Loss, and D. M. Zumbühl, Nat. Commun. **9**, 3454 (2018).
[41] E. Lijnen, L. F. Chibotaru, and A. Ceulemans, Phys. Rev. E **77**, 016702 (2008).
[42] L. Jansen and M. Boon, *Theory of Finite Groups: Applications in Physics* (North Holland, Amsterdam, 1967); M. Damnjanović, O simetriji u kvantnoj nerelativističkoj fizici, Fizički fakultet, Beograd (2000).
[43] In the case of $\mathbf{C}_{nv}/\mathbf{C}_{\infty v}$ groups, time-reversal Θ is the symmetry of the system. However, it can be checked that Θ can be safely neglected. Time reversal in the case of vectors from one-dimensional IRs has a trivial action. In the case of the two-dimensional IRs E_m time reversal transforms one vector of the IR into the other; in other words, it has the same behavior as the vertical mirror plane symmetry σ_v and can be ignored.
[44] W.-K. Li and S. M. Blinder, J. Math. Phys. **26**, 2784 (1985).
[45] L. F. Chibotaru, A. Ceulemans, M. Morelle, G. Teniers, C. Carballeira, and V. V. Moshchalkov, J. Math. Phys. **46**, 095108 (2005).
[46] We have explicitly checked that other states appearing in the perturbative expansion can be safely ignored.
[47] D. V. Khomitsky, L. V. Gulyaev, and E. Ya. Sherman, Phys. Rev. B **85**, 125312 (2012).
[48] J. Romhányi, G. Burkard, and A. Pályi, Phys. Rev. B **92**, 054422 (2015).
[49] M. T. Veszeli and A. Pályi, Phys. Rev. B **97**, 235433 (2018).

Analytical solution for time integrals in diagrammatic expansions: Application to real-frequency diagrammatic Monte Carlo

J. Vučičević,[1] P. Stipsić,[1,2] and M. Ferrero[3,4]

[1]*Scientific Computing Laboratory, Center for the Study of Complex Systems, Institute of Physics Belgrade, University of Belgrade, Pregrevica 118, 11080 Belgrade, Serbia*

[2]*Faculty of Physics, University of Belgrade, Studentski trg 12, 11001 Belgrade, Serbia*

[3]*CPHT, CNRS, Ecole Polytechnique, Institut Polytechnique de Paris, Route de Saclay, 91128 Palaiseau, France*

[4]*Collège de France, 11 place Marcelin Berthelot, 75005 Paris, France*

(Received 19 November 2020; accepted 25 March 2021; published 29 April 2021)

Recent years have seen a revived interest in the diagrammatic Monte Carlo (DiagMC) methods for interacting fermions on a lattice. A promising recent development allows one to now circumvent the analytical continuation of dynamic observables in DiagMC calculations within the Matsubara formalism. This is made possible by symbolic algebra algorithms, which can be used to analytically solve the internal Matsubara frequency summations of Feynman diagrams. In this paper, we take a different approach and show that it yields improved results. We present a closed-form analytical solution of imaginary-time integrals that appear in the time-domain formulation of Feynman diagrams. We implement and test a DiagMC algorithm based on this analytical solution and show that it has numerous significant advantages. Most importantly, the algorithm is general enough for any kind of single-time correlation function series, involving any single-particle vertex insertions. Therefore, it readily allows for the use of action-shifted schemes, aimed at improving the convergence properties of the series. By performing a frequency-resolved action-shift tuning, we are able to further improve the method and converge the self-energy in a nontrivial regime, with only 3–4 perturbation orders. Finally, we identify time integrals of the same general form in many commonly used Monte Carlo algorithms and therefore expect a broader usage of our analytical solution.

DOI: 10.1103/PhysRevResearch.3.023082

I. INTRODUCTION

Finding controlled solutions of the Hubbard model is one of the central challenges in condensed matter physics [1–4]. Many common approaches to this problem rely on the stochastic (Monte Carlo) summation of various expansions and decompositions of relevant physical quantities. However, Monte Carlo (MC) algorithms are often plagued by two notorious problems: the fermionic sign problem and the analytical continuation of frequency-dependent quantities in calculations based on the Matsubara formalism [5–8] (alternatively, the dynamical sign problem in the Kadanoff-Baym and Keldysh formalism calculations [9–23]). In diagrammatic Monte Carlo (DiagMC) methods [24–38] (as opposed to determinantal methods such as continuous-time interaction-expansion quantum Monte Carlo (CTINT) or, auxiliary-field quantum Monte Carlo (CTAUX) [39–42]), an additional problem is often the slow (or absence of) convergence of the series with respect to the perturbation order. In recent years, several works have started to address the problems of obtaining real-frequency quantities [43–51] and series convergence in DiagMC [52–57].

In Refs. [43,52], it has been shown that a convenient transformation of the interaction-expansion series can be used to significantly improve its convergence and sometimes allows one to converge the electronic self-energy with only a few perturbation orders where it would have otherwise been impossible. The method relies on a transformation of the action which affects the bare propagator at the cost of an additional expansion, i.e., more diagram topologies need to be taken into account. Alternatively, this transformation can be viewed as a Maclaurin expansion of the bare propagator with respect to a small chemical potential shift. The resulting convergence speedup comes from an increased convergence radius of the transformed series.

In a separate line of work, DiagMC methods have been proposed that are based on the Matsubara formalism that do not require an ill-defined analytical continuation [47]. Such methods have so far been implemented for the calculation of the self-energy [48,49] and the dynamical spin susceptibility [50]. The algorithms differ in some aspects, but all rely on the symbolic algebra solution of the internal Matsubara frequency summations appearing in Feynman diagrams. However, this approach has some downsides. First, numerical regulators are needed to properly evaluate Bose-Einstein distribution functions and diverging ratios that appear in the analytical expressions, and also poles on the real axis (effec-

tive broadening of the real-frequency results). In the case of finite cyclic lattice calculations, multiple precision algebra is needed in order to cancel divergences even with relatively large regulators [48]. Most importantly, in the Matsubara summation algorithm, applying the series transformation from Refs. [43,52] would require a separate analytical solution for each of the additional diagram topologies, which are very numerous, and the calculation would become rather impractical. More generally, treating any distinct diagram requires that the Matsubara frequency summations be performed algorithmically beforehand. This makes it difficult to devise MC sampling algorithms that go to indefinite perturbation orders, unless the Matsubara summation part is sufficiently optimized so that it no longer presents a prohibitive performance penalty if performed at the time of the Monte Carlo sampling.

In this paper, we show that it can be advantageous to start from the imaginary-time domain formulation of Feynman diagrams. A diagram contribution then features a multiple imaginary-time integral, rather than sums over Matsubara frequencies. The multiple integral can be solved analytically and we present a general solution. This analytical solution, although equivalent to the analytical Matsubara summation, has a simpler and more convenient form that does not feature Bose-Einstein distribution functions or diverging ratios. As a result, numerical regulators are not needed and the need for multiple precision arithmetic may arise only at very high perturbation orders. The numerical evaluation yields a sum of poles of various orders on a uniform grid on the real axis. The ability to separate contributions of poles of different orders allows one to formally extract the real-frequency result without any numerical broadening. Finally, the analytical solution is general and applies to all diagram topologies that would appear in the transformed series proposed in Refs. [43,52] or any other diagrammatic series for single-time correlation functions. This paves the way for real-frequency diagrammatic algorithms formulated in real space that are not *a priori* limited to small perturbation orders (similarly to CTINT or CTAUX [42]).

In this work, we apply the analytical time integral to the momentum-space DiagMC for the calculation of the self-energy, and implement and thoroughly test the method. We reproduce the self-energy results from Ref. [52] and supplement them with real-axis results, free of the uncontrolled systematic error that would otherwise come from the analytical continuation. Furthermore, we show that even if a full convergence is not possible with a single choice of the action-tuning parameter, one can choose the optimal tuning parameter for each frequency independently [46]. Such a frequency-resolved resummation can be used to improve the solution and in some cases systematically eliminate the nonphysical features that appear in the result due to the truncation of the series at a finite order.

The paper is organized as follows. In Sec. II, we define the model and the basic assumptions of our calculations. In Sec. III, we introduce our method in detail. First, in Sec. III A, we present the analytical solution of the general multiple-time integral that appears in the time-domain formulation of Feynman diagrams and discuss the numerical evaluation of the final expression. Then, in Sec. III B, we show the analytical solution for the Fourier transform of the Maclaurin expansion of the bare propagator, which is essential for our DiagMC algorithm. In Sec. III C, we discuss in detail how our analytical solutions can be applied in the context of DiagMC for the self-energy. In Sec. IV, we discuss our results and benchmarks and then give closing remarks in Sec. V. Additional details of the analytical derivations and further benchmarks and examples of the calculations can be found in the appendices.

II. MODEL

We solve the Hubbard model given by the Hamiltonian

$$H = -\sum_{\sigma,ij} t_{ij} c^{\dagger}_{\sigma,i} c_{\sigma,j} + U \sum_{i} n_{\uparrow,i} n_{\downarrow,i} - \mu \sum_{\sigma,i} n_{\sigma,i}, \qquad (1)$$

where $\sigma \in \{\uparrow, \downarrow\}$, i, j enumerate lattice sites, t_{ij} is the hopping amplitude between the sites i and j, U is the on-site coupling constant, and μ is the chemical potential. We only consider the Hubbard model on the square lattice with the nearest-neighbor hopping t and next-nearest-neighbor hopping t'. The bare dispersion is given by

$$\varepsilon_{\mathbf{k}} = -2t(\cos k_x + \cos k_y) - 4t' \cos k_x \cos k_y. \qquad (2)$$

We define $D = 4t$, which will be used as the unit of energy unless stated otherwise. We restrict to thermal equilibrium and paramagnetic phases with full lattice symmetry.

III. METHODS

The idea of DiagMC algorithms is to stochastically compute the coefficients of a perturbation series describing some physical quantity. We will focus on expansions in the coupling constant U and a shift in the chemical potential $\delta\mu$. The calculation of each coefficient involves the evaluation of many Feynman diagrams expressed in terms of the bare propagator, in our case taken as a function of momentum and two imaginary times. The evaluation of a diagram then boils down to a sum over multiple momentum variables and a multiple imaginary-time integral that is always of the same generic form. The goal of this section is to find a general analytical solution for these time integrals and reformulate the perturbation series as a function of a complex frequency z.

A. Analytical solution of time integrals

We are interested in analytically solving $(N-1)$-fold integrals over $\{\tau_{i=2\ldots N}\}$ of the form

$$\mathcal{I}_{\mathbf{X}}(i\Omega_\eta) = \prod_{i=2}^{N} \int_0^{\tau_{i+1}} d\tau_i \; \tau_i^{l_i} \; e^{\tau_i (i\Omega_\eta \delta_{r,i} + \omega_i)}, \qquad (3)$$

where the parameters of the integrand are given by

$$\mathbf{X} = (r, \{l_2 \ldots l_N\}, \{\omega_2 \ldots \omega_N\}). \qquad (4)$$

The argument r is an integer and determines which of the times τ_i is multiplied by the external Matsubara frequency $i\Omega_\eta$ in the exponential. The frequency $i\Omega_\eta$ can be any Matsubara frequency, either fermionic or bosonic, depending on η; $i\Omega_{\eta=-1} \equiv i\omega \equiv i(2m+1)\pi T$ and $i\Omega_{\eta=1} \equiv i\nu \equiv 2im\pi T$, with $m \in \mathbb{Z}$. The integer powers of τ_i outside of the exponent are given by $l_i \geqslant 0$, and the parameters ω_i may be complex.

The limit of the outermost integration is the inverse temperature $\tau_{N+1} \equiv \beta$. We denote by $\delta_{x,y}$ the Kronecker delta (it will be used throughout this paper, also in the shortened version $\delta_x \equiv \delta_{x,0}$). The reason for our choice to label times starting from 2 will become clear later.

The main insight is that upon applying the innermost integral, one gets a number of terms, but each new integrand has the same general form $\sim\tau^n e^{\tau z}$. The solution therefore boils down to a recursive application of

$$\int_0^{\tau_\mathrm{f}} \tau^n e^{\tau z} d\tau = \sum_{k=0}^{n+1} (-)^k C_{nk} \frac{\tau_\mathrm{f}^{n+1-k-B_{nk}} e^{B_{nk} z \tau_\mathrm{f}}}{z^{k+B_{nk}}}, \tag{5}$$

with $B_{nk} = 1 - \delta_{k,n+1}$ and $C_{nk} = \frac{n!}{(n-k+\delta_{k,n+1})!}$ (for the proof, see Appendix D), and

$$\lim_{z\to 0} \int_0^{\tau_\mathrm{f}} \tau^n e^{\tau z} d\tau = \frac{\tau_\mathrm{f}^{n+1}}{n+1}. \tag{6}$$

The number of terms obtained after each integration is apparently $1 + (1 - \delta_z)(n + 1)$, and we can enumerate all terms obtained after the full integration by a set of integers, $\{k_{i=2\ldots N}\}$, where $k_i \geqslant 0$ denotes the choice of the term of the integral i (over $d\tau_i$).

For a given choice of $\{k_i\}$, the propagation of exponents [n and z in Eqs. (5) and (6)] across successive integrals can be fully described by a simple set of auxiliary quantities. We denote the exponent of e in the integration i as $\tilde{z}_i$, and it is given by

$$\tilde{z}_i \equiv z_i + b_{i-1}\tilde{z}_{i-1}, \quad \tilde{z}_2 \equiv z_2, \tag{7}$$

$$z_i \equiv \delta_{i,r} i\Omega_\eta + \omega_i, \tag{8}$$

where we introduced $b_i \equiv B_{n_i,k_i}$. The meaning of b_i can be understood by looking at Eq. (5): The exponent of e that enters the integral on the left-hand side survives in all but the last term ($k = n + 1$) on the right-hand side. Therefore, $b_i = 1$ means that the exponent propagates from integration i to integration $i + 1$, while $b_i = 0$ means it does not, and the calculation of the recursive $\tilde{z}_i$ is reset with each $b_i = 0$. The auxiliary quantity n_i are the exponents of τ_i and is specified below.

We will need to obtain a more convenient expression for the exponent $\tilde{z}_i$, where $i\Omega_\eta$ appears explicitly. Straightforwardly, we can write

$$\tilde{z}_i = i\Omega_\eta h_i + \tilde{\omega}_i, \tag{9}$$

with auxiliary quantities

$$\tilde{\omega}_i \equiv \omega_i + b_{i-1}\tilde{\omega}_{i-1}, \quad \tilde{\omega}_2 \equiv \omega_2, \tag{10}$$

and

$$h_i \equiv \begin{cases} 0, & i < r \\ 1, & i = r \\ b_{i-1}h_{i-1}, & i > r. \end{cases} \tag{11}$$

To be able to determine whether the exponent in the integrand, $\tilde{z}_i$, is zero and then employ Eq. (6) if needed, we can now use

$$\delta_{\tilde{z}_i} = \begin{cases} 1, & h_i = 0 \wedge \tilde{\omega}_i = 0 \\ 0 & \text{otherwise.} \end{cases} \tag{12}$$

It is important to note that at the time of integration, $i\Omega_\eta$ is unspecified and whether $\tilde{z}_i$ is zero cannot be tested by numerical means, unless $i\Omega_\eta$ does not appear in $\tilde{z}_i$. With the convenient rewriting of Eq. (7) as Eq. (9), one can tell whether $i\Omega_\eta$ appears in $\tilde{z}_i$ by looking at h_i. If $i\Omega_\eta$ does appear in $\tilde{z}_i$ (i.e., $h_i = 1$), we cannot use Eq. (6) even if one can find such $i\Omega_\eta$ that cancels $\tilde{\omega}_i$. This is because we are working towards an analytical expression which ought to be general for all possible $i\Omega_\eta$.

The exponent of τ that will be carried over from integration i to integration $i + 1$ depends on the choice of the term from the integral i, and is given by $\mathrm{Pos}(n_i - k_i)$, where Pos denotes the positive part of the number $[\mathrm{Pos}(x) = (x + |x|)/2]$. n_i denotes the maximum exponent that can be carried over from integration i, and is obtained as

$$n_i = \begin{cases} \delta_{\tilde{z}_i} + l_i + \mathrm{Pos}(n_{i-1} - k_{i-1}), & i > 2 \\ \delta_{\tilde{z}_i} + l_i, & i = 2. \end{cases} \tag{13}$$

In the case of Eq. (5), the maximal exponent that can be carried over to the next integration coincides with the exponent that entered the integral [the integral given by Eq. (5) does not raise the power of τ], so the definition of n_i coincides with the meaning of n in Eq. (5). In the case of the integral given by Eq. (6), n_i rather denotes the exponent after the integration, i.e., $n + 1$.

After the last integration, it can happen that $i\Omega_\eta$ appears in the exponent of e (this is signaled by $h_N b_N = 1$). We can then use the property $e^{i\Omega_\eta \beta} = (-1)^{\delta_{\eta,-1}}$ to eliminate it from this exponent. Then, the solution for the integral can be continued to the whole of the complex plane $i\Omega_\eta \to z$, and can be written as (introducing the additional superscript η because the fermionic/bosonic nature of the expression can no longer be inferred from the external Matsubara frequency)

$$\begin{aligned} \mathcal{I}^\eta_{\mathbf{x}}(z) = & \sum_{\{b_i \in [\delta_{\tilde{z}_i}, 1]\}_{i=2\ldots N}} e^{b_N \beta \tilde{\omega}_N} \sum_{\{k_i \in [0, (1-\delta_{\tilde{z}_i}) n_i]\}_{i:b_i=1}} \\ & \times \prod_{i:\delta_{\tilde{z}_i}=1} \frac{1}{n_i} \\ & \times (-1)^{b_N h_N \delta_{\eta,-1} + \sum_{i=2}^N k_i} \times \beta^{n_N + 1 - b_N - k_N} \\ & \times \prod_{i:h_i=0 \wedge \tilde{\omega}_i \neq 0} \frac{C_{n_i,k_i}}{\tilde{\omega}_i^{k_i+b_i}} \prod_{i:h_i=1} \frac{C_{n_i,k_i}}{(z+\tilde{\omega}_i)^{k_i+b_i}}. \end{aligned} \tag{14}$$

Note that we have expressed the sum over $\{k_i\}$ as a sum over $\{b_i\}$ and a partial (inner) sum over $\{k_i\}$. This is not necessary, being that b_i is a function of k_i. Each b_i is fully determined by k_i, but not the other way around, so the inner sum over k_i in Eq. (14) goes over values that are allowed by the corresponding b_i. We present this form of Eq. (14) to emphasize that the factor $e^{b_N \beta \tilde{\omega}_N}$ depends only on $\{b_i\}$, and can thus be pulled out of the inner $\{k_i\}$ sum. The notation "$i : b_i = 1$" means that we only consider indices i such that $b_i = 1$. We therefore only sum over those k_i for which the corresponding $b_i = 1$. The remaining k_i are fixed to $n_i + 1$, which is the only possibility if $b_i = 0$. The notation is applied analogously in other products over i.

TABLE I. Illustration of the calculation of a single term in Eq. (14). Rows correspond to successive integrations over $d\tau_i$. The second to fourth columns are parameters of the integrand. The choice of the term is colored red. The remaining columns are auxiliary quantities, the integrand before and after each integration. The prefactors that are "collected" after each integration are written in blue. The full contribution is written in the last column and then simplified to the form of a term in Eq. (16).

i	$\delta_{r,i}$	l_i	ω_i	k_i	b_i	n_i	$\tilde{\omega}_i$	h_i	$\delta_{\tilde{z}_i}$	Integrand	Integral	Total
2	0	0	1	0	1	0	1	0	0	$e^{\tau_2 1}$	$\frac{1}{1}e^{\tau_3 1} - \frac{1}{1}1$	
3	0	1	2	1	1	1	3	0	0	$\tau_3 e^{\tau_3(2+1)}$	$\frac{1}{3}\tau_4 e^{\tau_4 3} - \frac{1}{3^2}e^{\tau_4 3} + \frac{1}{3^2}1$	
4	1	0	1	1	0	0	4	1	0	$e^{\tau_4(i\Omega_\eta+1+3)}$	$\frac{1}{i\Omega_\eta+4}e^{\tau_5(i\Omega_\eta+4)} - \frac{1}{i\Omega_\eta+4}1$	$\frac{1}{1}(-\frac{1}{3^2})(-\frac{1}{i\Omega_\eta+4})\frac{1}{1}\frac{1}{4}\beta e^{\beta 4}$
5	0	0	0	0	1	1	0	0	1	$e^{\tau_5 0}$	$\frac{1}{1}\tau_6^1$	$\rightarrow \frac{\beta e^{4\beta}/36}{[z-(-4)]^1}$
6	0	0	4	0	1	1	4	0	0	$\tau_6 e^{\tau_6 4}$	$\frac{1}{4}\beta e^{\beta 4} - \frac{1}{4^2}e^{\beta 4} + \frac{1}{4^2}1$	

The only remaining step is to expand the product of poles in Eq. (14) into a sum of poles (see Ref. [48] for more details),

$$\prod_\gamma \frac{1}{(z-z_\gamma)^{m_\gamma}} = \sum_\gamma \sum_{r=1}^{m_\gamma} \frac{1}{(z-z_\gamma)^r} \times (-1)^{m_\gamma - r} \sum_{\mathcal{C}\{p_{\gamma'\neq\gamma}\in\mathbb{N}_0\}:\sum_{\gamma'\neq\gamma} p_{\gamma'}=m_\gamma - r} \times \prod_{\gamma'\neq\gamma} \frac{(m_{\gamma'}+p_{\gamma'}-1)!}{p_{\gamma'}!(m_{\gamma'}-1)!} \frac{1}{(z_\gamma - z_{\gamma'})^{m_{\gamma'}+p_{\gamma'}}}, \tag{15}$$

and the final expression has the form

$$\mathcal{I}^\eta_{\mathbf{X}}(z) = \sum_{j,p\in\mathbb{N}} \frac{\mathcal{A}_{j,p}}{(z-\mathcal{Z}_j)^p}. \tag{16}$$

In order to illustrate our solution, we present in tabular form (Table I) a summary of all intermediate steps, integrand parameters, and auxiliary quantities that are used in calculating the contribution for a single choice of $\{k_i\}$, in an example with $N = 6$ and $r = 4$.

Also note that if $r \notin [2, N]$ (no Matsubara frequency appearing in any exponent), the result of the integral is a number, rather than a frequency-dependent quantity. In that case, the integral can be straightforwardly generalized to the case of real time, where integrations go to some externally given time t (instead of β), and the resulting expression is a function of that time. The step given by Eq. (15) is then not needed. See Appendix A for details.

Numerical evaluation of the analytical expression and relation to other algorithms

The implementation of Eq. (14) is rather straightforward and much simpler than the algorithmic Matsubara summations in our previous work [48]. Indeed, most of the calculations just require the numerical evaluation of an analytical expression and it is not necessary to implement a dedicated symbolic algebra to manipulate the expressions. The only exception is the last step, Eq. (15). This transformation was the centerpiece of the algorithm in Ref. [48] and was applied recursively many times, leading to complex bookkeeping and data structures. Ultimately, the result was a symbolic expression that was stored, and a separate implementation was needed for the comprehension and numerical evaluation of such a general symbolic expression. In the present context, however, Eq. (15) is applied only once to produce numbers, and is simple to implement.

The other important point is that we analytically treat cases with $\delta_{\tilde{z}_i} = 1$ by employing Eq. (6). With the frequency-summation algorithms [48,49], one cannot take into account possible cancellations of the ω_i terms in Eq. (10) without computing a large number of separate analytical solutions. When untreated, these cancellations yield diverging ratios in the final expressions, which need to be regularized. On the contrary, in Eq. (14), the ratio $1/\tilde{\omega}_i^{k_i+b_i}$ cannot have a vanishing denominator and its size will, in practice, be limited by the energy resolution. This will also allow us to have the final result in the form of a sum of poles on an equidistant grid on the real axis, and extract the real-axis results without any numerical pole broadening (see Sec. III C 2 and Appendix B).

It is interesting to compare the computational effort for the numerical evaluation of our analytical solution to the straightforward numerical integration. In the most straightforward integration algorithm, one would discretize the imaginary-time interval $[0, \beta]$ with N_τ times, and then perform the summation which has the complexity $O(N_\tau^{N-1})$ for each external τ, so that overall $O(N_\tau^N)$. With our algorithm, we do not have to go through all of the configurations of internal times, but we do need to go through all of the possible permutations of the internal times, and for each permutation there is at least 2^{N-1} terms to be summed over. So the number of terms one has to sum grows at least as $O[(N-1)!2^{N-1}]$. At sufficiently high N, this number is bound to outgrow the exponential N_τ^N, whatever the N_τ. This will happen, however, only at very large N. For example, if $N_\tau = 30$, the analytical solution becomes slower at around $N = 40$. Moreover, one actually needs a much larger N_τ, especially at low temperature. In any case, the additional computational effort can be understood as coming from the difference in the information content of the result, which is a lot more substantial in the case of the analytical solution.

At orders $N < 6$ (within context of DiagMC), we find that the implementation of our algorithm is significantly more efficient than our current implementation of the Matsubara summations from Ref. [48], and at $N = 6$, they are about equally efficient. However, we anticipate that further optimizations will be possible at the level of Eq. (14).

B. Expansion of the bare propagator

The central quantity is the Green's function defined in Matsubara formalism as

$$G_{\sigma\mathbf{k}}(\tau-\tau') = -\langle T_\tau c_{\sigma\mathbf{k}}(\tau) c^\dagger_{\sigma\mathbf{k}}(\tau')\rangle = \begin{cases} -\langle c_{\sigma\mathbf{k}}(\tau) c^\dagger_{\sigma\mathbf{k}}(\tau')\rangle, & \tau > \tau' \\ \langle c^\dagger_{\sigma\mathbf{k}}(\tau') c_{\sigma\mathbf{k}}(\tau)\rangle, & \tau' > \tau, \end{cases} \quad (17)$$

where $\tau, \tau' \in [0, \beta]$. The noninteracting Green's function (or the bare propagator) in the eigenbasis of the noninteracting Hamiltonian has a very simple general form,

$$G_0(\varepsilon, i\omega) \equiv \frac{1}{i\omega - \varepsilon}, \quad (18)$$

and for the plane wave $\mathbf{k}$, the propagator is $G_{0,\mathbf{k}}(i\omega) = G_0(\varepsilon_\mathbf{k} - \mu, i\omega)$.

As we will discuss below, the diagrammatic series for the self-energy will, in general, be constructed from different powers of the bare propagator,

$$G_0^l(\varepsilon, i\omega) \equiv \frac{1}{(i\omega - \varepsilon)^l}. \quad (19)$$

Indeed, these powers naturally arise after expanding the bare propagator in a Maclaurin series, $\frac{1}{z+x} = \sum_{n=0}^\infty \frac{(-x)^n}{z^{n+1}}$, around a small chemical potential shift,

$$G_0(\varepsilon, i\omega) = \sum_{l=1}^\infty (-\delta\mu)^{l-1} G_0^l(\varepsilon + \delta\mu, i\omega). \quad (20)$$

This series converges (for all $i\omega$) if $\delta\mu$ is smaller in amplitude than the first Matsubara frequency: $|\delta\mu| < \pi T$. Nevertheless, this expression will become a part of a larger series with additional expansion parameters, which may result in a modified convergence radius of the overall series with respect to $\delta\mu$.

We anticipate that the Feynman diagrams will be formulated in the imaginary-time domain, so it is essential to work out the Fourier transform of $G_0^l(\varepsilon, i\omega)$. We present the full derivation in Appendix E and here only write the final solution,

$$G_0^l(\varepsilon, \tau-\tau') = s_{\tau,\tau'} e^{-\varepsilon(\tau-\tau')} n_\mathrm{F}(s_{\tau,\tau'}\varepsilon) \sum_{\zeta=0}^{l-1} \sum_{\varsigma=0}^{l-\zeta-1} c^{s_{\tau,\tau'}}_{l\zeta\varsigma}(\varepsilon)\, \tau^\zeta \tau'^\varsigma, \quad (21)$$

with $s_{\tau,\tau'} = \mathrm{sgn}(\tau' - \tau)$. In our notation, l in G_0^l is a superscript index, rather than the power of G_0 [although these meanings coincide in the case of $G_0^l(\varepsilon, i\omega)$]. The Fermi function is defined as $n_\mathrm{F}(\varepsilon) = 1/(e^{\beta\varepsilon} + 1)$ and the coefficients that go with the $\tau^\zeta \tau'^\varsigma$ terms are

$$c^-_{l,\zeta,\varsigma}(\varepsilon) = \sum_{n=0}^{l-\varsigma-\zeta-1} \frac{n!(-1)^{l+\varsigma-1}[-n_\mathrm{F}(\varepsilon)]^n \beta^{l-\varsigma-\zeta-1}}{(l-\varsigma-\zeta-1)!(\varsigma+\zeta)!} \times \left\{ {l-\varsigma-\zeta-1 \atop n} \right\} \binom{\varsigma+\zeta}{\zeta}, \quad (22)$$

and $c^+_{l,\zeta,\varsigma}(\varepsilon) = (-1)^{l-1} c^-_{l,\varsigma,\zeta}(-\varepsilon)$. Here we make use of binomial coefficients $\binom{n}{k} = \frac{n!}{k!(n-k)!}$ and the Stirling number of the second kind, $\left\{ {n \atop k} \right\} = \sum_{i=0}^k \frac{(-1)^i}{k!} \binom{k}{i} (k-i)^n$.

C. Application to DiagMC

In the following, we apply the analytic time integral and the expansion of the bare propagator in the context of DiagMC. We discuss two kinds of self-energy series (Hartree shifted and bare) and the corresponding implementation details. Note that some symbols will be redefined with respect to previous sections.

1. Hartree-shifted series

In this section, we discuss the construction of the self-energy series, where all tadpolelike insertions are omitted in the topologies of the diagrams. Rather, the full Hartree shift is absorbed in the bare propagator. The diagrams are therefore expressed in terms of the Hartree-shifted bare propagator,

$$G^\mathrm{HF}_{0,\mathbf{k}}(i\omega) = G_0(\tilde{\varepsilon}_\mathbf{k}, i\omega), \quad (23)$$

with the Hartree-shifted dispersion defined as

$$\tilde{\varepsilon}_\mathbf{k} = \varepsilon_\mathbf{k} - \mu + U\langle n_\sigma\rangle, \quad (24)$$

where $\langle n_{\bar\sigma}\rangle$ is the average site occupation per spin.

After constructing the tadpoleless topologies, we are free to expand all propagators that appear in the diagrams according to Eq. (20):

$$G^\mathrm{HF}_{0,\mathbf{k}}(i\omega) = \sum_{l=1}^\infty (-\delta\mu)^{l-1} G_0^l(\tilde{\varepsilon}_\mathbf{k} + \delta\mu, i\omega). \quad (25)$$

In the frequency domain, this step can be viewed as introducing new topologies: we now have diagrams with any number of single-particle-vertex ($\delta\mu$) insertions on any of the propagator lines. Each arrangement of these additional single-particle vertices on the diagram does require a separate solution by the symbolic algebra algorithm, as presented in Refs. [48,49]. Nevertheless, as a $\delta\mu$ vertex cannot carry any momentum or energy, the formal effect of it is that it just raises the power l of the propagator that passes through it. In the imaginary-time domain, it turns out that the contribution of the $\delta\mu$-dressed diagrams is readily treatable by the analytical expression (14) and we no longer have to view the $\delta\mu$ insertions as changes to topology, but rather as additional internal degrees of freedom to be summed over. This is illustrated in Fig. 1.

Up to the Hartree shift, the self-energy expansion can now be made in powers of the interaction U and the small chemical-potential shift $\delta\mu$,

$$\Sigma^{(\mathrm{HF})}_\mathbf{k}(\tau) = \sum_N (-U)^N \times \sum_{l_1,\ldots,l_{2N-1}=1}^\infty (-\delta\mu)^{\sum_j (l_j-1)} \sum_{\Upsilon_N} D_{\Upsilon_N,\mathbf{k},\{l_j\},\delta\mu}(\tau), \quad (26)$$

where j enumerates the propagators, of which there are $N_\mathrm{prop} = 2N-1$, N is the perturbation order in U, each l_j goes from 1 to ∞, Υ_N enumerates distinct topologies of the diagram at order N (without any $\delta\mu$ or Hartree insertions), and D is the contribution of the diagram. The general form of the

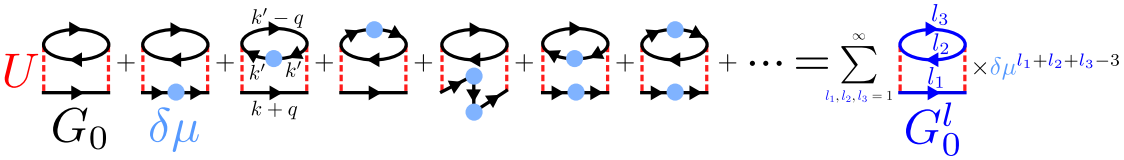

FIG. 1. Illustration of the use of the $G_0^l(\varepsilon, \tau - \tau')$ propagator. The entire series of diagrams with all possible $\delta\mu$ insertions can be captured by a single diagram with additional degrees of freedom.

diagram contribution is

$$D_{\Upsilon_N,\mathbf{k},\{l_j\},\delta\mu}(\tau) = (-1)^{N_{\text{bub}}} \prod_{i=2}^{N-1} \int_0^\beta d\tau_i \sum_{\mathbf{k}_1 \ldots \mathbf{k}_N} \prod_{j=1}^{2N-1} G_0^{l_j}\left(\bar{\varepsilon}_{\tilde{\mathbf{k}}_j}, \tilde{\tau}_j - \tilde{\tau}'_j\right), \quad (27)$$

with $\bar{\varepsilon}_{\mathbf{k}} \equiv \tilde{\varepsilon}_{\mathbf{k}} + \delta\mu$. We denote N_{bub} as the number of closed fermion loops in the diagram; $\tau_1 \ldots \tau_{N-1}$ are internal times, and we fix $\tau_{i=1} = 0$; τ is the external time, $\mathbf{k}$ is the external momentum, $\mathbf{k}_1 \ldots \mathbf{k}_N$ are the independent internal momenta, j indexes the propagator lines, and $\tilde{\mathbf{k}}$ are the corresponding linear combinations of the momenta $\tilde{\mathbf{k}}_j \equiv \sum_{\lambda=0}^{N} \tilde{s}_{j\lambda} \mathbf{k}_\lambda$, where $\tilde{s}_{j\lambda} \in \{-1, 0, 1\}$, and we index with 0 the external momentum $\mathbf{k}_0 \equiv \mathbf{k}$. $\tilde{\tau}_j$ and $\tilde{\tau}'_j$ are the outgoing and incoming times for the propagator j, and take values in $\{\tau_1 \ldots \tau_N\}$, where we denote with index N the external time $\tau_N \equiv \tau$. The coefficients $\tilde{s}_{j\lambda}$, times $\tilde{\tau}_j$, $\tilde{\tau}'_j$, and the number N_{bub} are implicit functions of the topology Υ_N. Throughout the paper, we assume normalized $\mathbf{k}$ sums, $\sum_{\mathbf{k}} \equiv \frac{1}{N_{\mathbf{k}}} \sum_{\mathbf{k}}$, where $N_{\mathbf{k}}$ is the number of lattice sites.

We can perform the Fourier transform of the external time to obtain the contribution of the diagram in the Matsubara-frequency domain,

$$D_{\Upsilon_N,\mathbf{k},\{l_j\},\delta\mu}(i\omega) = (-1)^{N_{\text{bub}}} \prod_{i=2}^{N} \int_0^\beta d\tau_i e^{i\omega\tau_N} \sum_{\mathbf{k}_1 \ldots \mathbf{k}_N} \prod_{j=1}^{2N-1} G_0^{l_j}\left(\bar{\varepsilon}_{\mathbf{k}_j}, \tilde{\tau}_j - \tilde{\tau}'_j\right). \quad (28)$$

The Green's function $G_0^l(\varepsilon, \tau - \tau')$ is discontinuous at $\tau = \tau'$, so to be able to perform the τ integrations analytically, we first need to split the integrals into ordered parts,

$$\int_0^\beta d\tau_2 \ldots \int_0^\beta d\tau_N = \sum_{(\tau_{p_2} \ldots \tau_{p_N}) \in \mathcal{P}(\{\tau_2 \ldots \tau_N\})} \int_0^\beta d\tau_{p_N} \int_0^{\tau_{p_N}} d\tau_{p_{N-1}} \ldots \int_0^{\tau_{p_4}} d\tau_{p_3} \int_0^{\tau_{p_3}} d\tau_{p_2}, \quad (29)$$

where $\mathcal{P}$ denotes all $(N-1)!$ permutations of the time indices. p labels the permutation and p_i is the permuted index of vertex i.

Let us rewrite the contribution of the diagram, with propagators written explicitly using the expression (21),

$$\begin{aligned} D_{\Upsilon_N,\mathbf{k},\{l_j\},\delta\mu}(i\omega) = (-1)^{N_{\text{bub}}} \sum_{\mathbf{k}_1 \ldots \mathbf{k}_N} \sum_{(\tau_{p_2} \ldots \tau_{p_N}) \in \mathcal{P}(\{\tau_2 \ldots \tau_N\})} (-1)^{N_{\text{fwd}}(p)} \prod_j n_{\text{F}}\left(s_j \bar{\varepsilon}_{\tilde{\mathbf{k}}_j}\right) \sum_{\zeta_j=0}^{l_j-1} \sum_{\varsigma_j=0}^{l_j-\zeta_j-1} c^{s_j}_{l_j,\zeta_j,\varsigma_j}\left(\bar{\varepsilon}_{\tilde{\mathbf{k}}_j}\right) \prod_{j \in \mathcal{J}_{\text{i}}(i=1)} \delta_{\zeta_j} \prod_{j \in \mathcal{J}_{\text{o}}(i=1)} \delta_{\varsigma_j} \\ \times \int_0^\beta d\tau_{p_N} \int_0^{\tau_{p_N}} d\tau_{p_{N-1}} \ldots \int_0^{\tau_{p_4}} d\tau_{p_3} \int_0^{\tau_{p_3}} d\tau_{p_2} e^{i\omega\tau_N} \prod_{i=2}^{N} \tau_i^{\sum_{j \in \mathcal{J}_{\text{i}}(i)} \zeta_j + \sum_{j \in \mathcal{J}_{\text{o}}(i)} \varsigma_j} e^{\tau_i\left(\sum_{j \in \mathcal{J}_{\text{o}}(i)} \bar{\varepsilon}_{\tilde{\mathbf{k}}_j} - \sum_{j \in \mathcal{J}_{\text{i}}(i)} \bar{\varepsilon}_{\tilde{\mathbf{k}}_j}\right)}, \end{aligned} \quad (30)$$

where $\mathcal{J}_{\text{i/o}}(i)$ is the set of incoming/outgoing propagators j of the vertex i, which depends on the topology Υ_N. We also introduced shorthand notation $s_j = s_{\tilde{\tau}_j, \tilde{\tau}'_j}$. Practically, s_j depends on whether $p(i(j)) > p(i'(j))$ or the other way around, where $i(j)/i'(j)$ is the outgoing/incoming vertex of propagator j in the given permutation p. The total number of forward-facing propagators is $N_{\text{fwd}}(p) = \sum_j \delta_{-1,s_j}$, which depends on the permutation and the topology. The products of δ_{ζ_j} and δ_{ς_j} are there to ensure that the time $\tau_1 = 0$ is not raised to any power other than 0, as such terms do not contribute.

Now we can apply the analytic solution for the time integrals [Eq. (14)] to arrive at the final expression:

$$\begin{aligned} D_{\Upsilon_N,\mathbf{k},L,\delta\mu}(z) = (-1)^{N_{\text{bub}}} \sum_{\{\tilde{l}_j \geqslant 0\}:\sum_j \tilde{l}_j = L} \sum_{\mathbf{k}_1 \ldots \mathbf{k}_N} \sum_{(\tau_{p_2} \ldots \tau_{p_N}) \in \mathcal{P}(\{\tau_2 \ldots \tau_N\})} (-1)^{N_{\text{fwd}}(p)} \\ \times \prod_j n_{\text{F}}\left(s_j \bar{\varepsilon}_{\tilde{\mathbf{k}}_j}\right) \sum_{\zeta_j=0}^{\tilde{l}_j} \sum_{\varsigma_j=0}^{\tilde{l}_j-\zeta_j} c^{s_j}_{\tilde{l}_j+1,\zeta_j,\varsigma_j}\left(\bar{\varepsilon}_{\tilde{\mathbf{k}}_j}\right) \prod_{j \in \mathcal{J}_{\text{i}}(i=1)} \delta_{\zeta_j} \prod_{j \in \mathcal{J}_{\text{o}}(i=1)} \delta_{\varsigma_j} \mathcal{I}^{\eta=-1}_{\mathbf{X}}(z), \\ \mathbf{X} = \left(p(N), \left\{ \sum_{j \in \mathcal{J}_{\text{i}}(i(p_{i'}))} \zeta_j + \sum_{j \in \mathcal{J}_{\text{o}}(i(p_{i'}))} \varsigma_j \right\}_{i'=2 \ldots N}, \left\{ \sum_{j \in \mathcal{J}_{\text{o}}(i(p_{i'}))} \bar{\varepsilon}_{\tilde{\mathbf{k}}_j} - \sum_{j \in \mathcal{J}_{\text{i}}(i(p_{i'}))} \bar{\varepsilon}_{\tilde{\mathbf{k}}_j} \right\}_{i'=2 \ldots N} \right), \end{aligned} \quad (31)$$

where $i(p_{i'})$ is the vertex index i of the permuted index $p_{i'}$ and we have introduced a new expansion variable $L = \sum_j (l_j - 1)$ and a convenient variable $\tilde{l}_j = l_j - 1$, so that

$$\Sigma_{\mathbf{k}}^{(\mathrm{HF})}(z) = \sum_{K=2}^{\infty} \sum_{N=2}^{K} \sum_{L=0}^{K-N} (-U)^N (-\delta\mu)^L \sum_{\Upsilon_N} D_{\Upsilon_N,\mathbf{k},L,\delta\mu}(z), \tag{32}$$

which is the series that we implement and use in practice. The meaning of K is the number of all independent (internal and external) times in the diagram. Note that in $\mathcal{D}$, we perform only $N-1$ integrations over time. Those are the times associated with N interaction vertices, minus the one that is fixed to zero. The integrations of the times associated with $\delta\mu$ insertions have already been performed in Eq. (21), and there are L such integrals. Overall, the number of independent times is $K = N + L$. Ultimately, we group contributions by the expansion order K and look for convergence with respect to this parameter.

2. Numerical implementation of DiagMC and relation to other algorithms

The expression (31) is very convenient for numerical evaluation. First, we restrict the values of $\bar{\varepsilon}_{\mathbf{k}}$ to a uniform grid on the real axis with the step $\Delta\omega$ ($\bar{\varepsilon}_{\mathbf{k}} = j\Delta\omega$). These appear in $\omega_2, \ldots, \omega_K$ as terms with integer coefficients, which means that $\{\omega_i\}$ entering $\mathcal{I}_{\mathbf{X}}$ will also be restricted to the same uniform grid. The final result therefore has the form

$$D_{\Upsilon_N,\mathbf{k},L,\delta\mu}(z) = \sum_{j\in\mathbb{Z},p\in\mathbb{N}} \frac{\mathcal{A}_{j,p}}{(z - j\Delta\omega)^p}. \tag{33}$$

This form allows us to reinterpret the finite-lattice results as that of the thermodynamic limit and extract $D_{\Upsilon_N,\mathbf{k},L,\delta\mu}(\omega + i0^+)$ without any numerical broadening (see Appendix B for details).

In our present implementation, we perform a flat-weight (uniform) MC sampling over internal momenta $\{\mathbf{k}_i\}$, do a full summation of all the other sums, and accumulate the amplitudes $\mathcal{A}_{j,p}$. There are, however, other options. For example, one may sample $\{\mathbf{k}_i\}, \{p_i\}, \{b_i\}$ and use $P \equiv \prod_j n_{\mathrm{F}}(s_j \bar{\varepsilon}_{\tilde{\mathbf{k}}_j}) e^{b_N \beta \tilde{\omega}_N}$ as the weighting function. We have thoroughly checked that the factor P closely correlates with the contribution to $\mathcal{A}_{j,p}$ coming from a given choice of the $\{\mathbf{k}_i\}, \{p_i\}, \{b_i\}$ variables (with other variables summed over), and thus P could be a good choice for a weighting function. However, this requires additional operations related to move proposals and trials, and we have not yet been able to make such an algorithm more efficient than the flat-weight MC. Nevertheless, it is apparent that our approach offers more flexibility than the algorithmic Matsubara summations (AMS). In AMS, no convenient weighting function can be defined for the Monte Carlo, so one either does the flat-weight summation [48] or uses the whole contribution to the result as the weight, which comes at the price of having to repeat the calculation for each frequency of interest [49] (on the contrary, in Ref. [48], as well as in this paper, the entire frequency dependence of the self-energy is obtained in a single MC run). At present, it is unclear which scheme is best—whether one should evaluate $D(z)$ one z at a time or capture all z at once as we do here. This choice, as well as the choice of the weighting function, likely needs to be made on a case-by-case basis, as it is probable that in different regimes, different approaches will be optimal. In that sense, the added flexibility of our time-integration approach in terms of the choice of the weighting function may prove valuable in the future.

Concerning floating-point arithmetic, it is important that the factor $e^{b_N \beta \tilde{\omega}_N}$ stemming from $\mathcal{I}_{\mathbf{X}}$ can always be absorbed into the product of n_{F} functions in the second row of Eq. (31). This can be understood as follows. A given $\bar{\varepsilon}_{\tilde{\mathbf{k}}_j}$ can, at most, appear twice as a term in $\tilde{\omega}_N$, once with sign $+1$ and once with sign -1, corresponding to the incoming $\tilde{\tau}'_j$ and outgoing $\tilde{\tau}_j$ ends of the propagator j. In that case, the exponent cancels. The other possibility is that it appears only once, in which case it must correspond to the later time in the given permutation. If the later time is the outgoing end of the propagator, then the propagator is forward facing and the sign in front is $s = -1$; if it is the incoming end, then the propagator is backward facing and the sign in front is $s = 1$. In both cases, we can make use of

$$e^{s\beta\varepsilon} n_{\mathrm{F}}(s\varepsilon) = n_{\mathrm{F}}(-s\varepsilon). \tag{34}$$

Therefore, no exponentials will appear in the final expression. A product of n_{F} functions is, at most, 1 and the coefficients c are not particularly big. Then, the size of the pole amplitudes that come out of Eq. (14) is determined by the energy resolution $(1/\Delta\omega)$ and temperature $(\beta^{n_N+1-b_N-k_N})$. In our calculations so far, the amplitudes remain relatively small. Our approach ensures that we do not have very large canceling terms, such as we had in Ref. [48]. Indeed, we have successfully implemented Eq. (31) without the need for multiple-precision floating-point types.

Compared to the Matsubara-frequency summation algorithm [47–49], Eq. (31) presents an improved generality. Equation (31) is valid for any number and arrangement of instantaneous (i.e., frequency-independent) insertions, i.e., any choice of $\{\tilde{l}_j\}$. In contrast, the algorithmic Matsubara summation has to be performed for each choice of $\{\tilde{l}_j\}$ independently, and the resulting symbolic expressions need to be stored. For example, at $N = 4$, we have 12 Υ_N topologies. Therefore, at $L = 0$, the number of analytical solutions to prepare is 12. However, at $L = 2$, this number is 336, i.e., 28-fold bigger (we can place $L = 2$ insertions on $2N - 1 = 7$ fermionic lines in $7 \times 6/2 + 7 = 28$ ways, times 12 Υ_N topologies, i.e., 336).

3. Bare series

We are also interested in constructing a bare series where tadpole insertions are present in diagram topologies. Tadpole (or Hartree) insertions are instantaneous and an evaluation of their amplitudes can be done relatively simply by various means. At the level of the Hubbard model, the Hartree insertions factor out: For each Hartree diagram, the internal momentum summations and time integrations can be performed beforehand and only once, leading to a significant speedup.

In the expression (31), there is no difference between a Hartree insertion and a chemical-potential vertex insertion. Therefore, the inclusion of the Hartree insertions can be en-

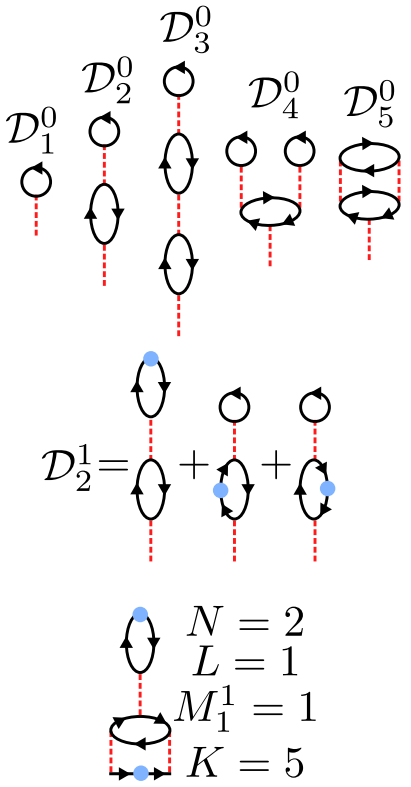

FIG. 2. Top: Illustration of possible Hartree diagrams, without any $\delta\mu$ insertions. Middle: Amplitude of a Hartree diagram with a single $\delta\mu$ insertion. Bottom: An example of a diagram dressed with both Hartree and $\delta\mu$ insertions, and the values of the parameters $N, L, \{M_i^{L'}\}, K$ that it falls under (with $M_{i\neq 1}^{L'\neq 1} = 0$).

tirely accounted for in the resummation of the $D_{\Upsilon_N,\mathbf{k},L,\delta\mu}(z)$ contributions from the previous section, with the replacement

$$\bar{\varepsilon}_{\mathbf{k}} \equiv \varepsilon_{\mathbf{k}} - \mu + \delta\mu \tag{35}$$

(i.e., full Hartree shift excluded).

Note that the expansion of the propagators in $\delta\mu$ is performed in Hartree insertions as well, so we need to account for possible additional $\delta\mu$ insertions inside the Hartree diagrams. As before, our expansion order will be K, which is the total number of independent times, with each time associated to a single interaction or a $\delta\mu$ vertex, including those within Hartree insertions.

We will for now focus on the series up to $K = 5$. As the number of interactions in Υ_N is at least two, we can have, at most, three interaction vertices in a Hartree insertion. There are only five such Hartree diagrams (Fig. 2). We can evaluate these five amplitudes with very little effort by making use of spatial and temporal Fourier transforms.

Before we proceed with the calculation of the amplitudes $\mathcal{D}$ of possible Hartree insertions relevant for the series up to $K = 5$, we define some auxiliary quantities. We first define the bare density,

$$n_0^{\tilde{l}} = \sum_{\mathbf{k}} G_0^{l=1+\tilde{l}}(\bar{\varepsilon}_{\mathbf{k}}, \tau = 0^-), \tag{36}$$

and the real-space propagator,

$$G_{0,\mathbf{r}}^{l=1+\tilde{l}} = \sum_{\mathbf{k}} e^{i\mathbf{k}\cdot\mathbf{r}} G_0^{l=1+\tilde{l}}(\bar{\varepsilon}_{\mathbf{k}}, \tau = 0^-). \tag{37}$$

We will also need the polarization bubble diagram,

$$\chi_{0,\mathbf{r}}^{\tilde{l}_1,\tilde{l}_2}(\tau) = G_{0,\mathbf{r}}^{l=1+\tilde{l}_1}(\tau) G_{0,-\mathbf{r}}^{l=1+\tilde{l}_2}(-\tau), \tag{38}$$

$$\chi_{0,\mathbf{q}=0}^{\tilde{l}_1,\tilde{l}_2}(i\nu = 0) = \sum_{\mathbf{r}} \int d\tau \, \chi_{0,\mathbf{r}}^{\tilde{l}_1,\tilde{l}_2}(\tau), \tag{39}$$

and the second-order self-energy diagram (up to the constant prefactor),

$$\Sigma_{2,\mathbf{r}}^{\tilde{l}_1,\tilde{l}_2,\tilde{l}_3}(\tau) = G_{0,\mathbf{r}}^{l=1+\tilde{l}_1}(\tau) \chi_{0,\mathbf{r}}^{\tilde{l}_2,\tilde{l}_3}(\tau), \tag{40}$$

which can be Fourier transformed to yield $\Sigma_{2,\mathbf{k}}^{\tilde{l}_1,\tilde{l}_2,\tilde{l}_3}(i\omega)$.

We can now calculate the amplitudes of the possible Hartree insertions with a number L of $\delta\mu$ insertions on them, in any arrangement

$$\mathcal{D}_1^L = (-) n_0^L, \tag{41}$$

$$\mathcal{D}_2^L = (-)^2 \sum_{\substack{\tilde{l}_1,\tilde{l}_2,\tilde{l}_3 \\ \tilde{l}_1+\tilde{l}_2+\tilde{l}_3 = L}} n_0^{\tilde{l}_1} \chi_{0,\mathbf{q}=0}^{\tilde{l}_2,\tilde{l}_3}(i\nu = 0), \tag{42}$$

$$\mathcal{D}_3^L = (-)^3 \sum_{\substack{\tilde{l}_1,\ldots,\tilde{l}_5 \\ \sum_i \tilde{l}_i = L}} n_0^{\tilde{l}_1} \chi_{0,\mathbf{q}=0}^{\tilde{l}_2,\tilde{l}_3}(i\nu = 0) \chi_{0,\mathbf{q}=0}^{\tilde{l}_4,\tilde{l}_5}(i\nu = 0), \tag{43}$$

$$\mathcal{D}_4^L = (-)^3 \sum_{\substack{\tilde{l}_1,\ldots,\tilde{l}_3 \\ \sum_i \tilde{l}_i = L}} \binom{2+\tilde{l}_3}{2} n_0^{\tilde{l}_1} n_0^{\tilde{l}_2} n_0^{2+\tilde{l}_3}, \tag{44}$$

$$\mathcal{D}_5^L = (-)^2 \sum_{\substack{\tilde{l}_1,\ldots,\tilde{l}_5 \\ \sum_i \tilde{l}_i = L}} T \sum_{i\omega} e^{-i\omega 0^-} \sum_{\mathbf{k}} G_{0,\mathbf{k}}^{l=1+\tilde{l}_1}(i\omega) \Sigma_{2,\mathbf{k}}^{\tilde{l}_2,\tilde{l}_3,\tilde{l}_4}(i\omega) G_{0,\mathbf{k}}^{l=1+\tilde{l}_5}(i\omega). \tag{45}$$

As we are restricting to $K \leqslant 5$ calculations, the $\mathcal{D}_{3\ldots5}^L$ insertions can only be added once, and only with $L = 0$. We now define M_i^L as the number of insertions of $\mathcal{D}_i^L$ tadpoles, and we define N_i as the number of interaction vertices contained in the tadpole $\mathcal{D}_i$ (regardless of L, we have $N_1 = 1, N_2 = 2, N_3 = N_4 = N_5 = 3$).

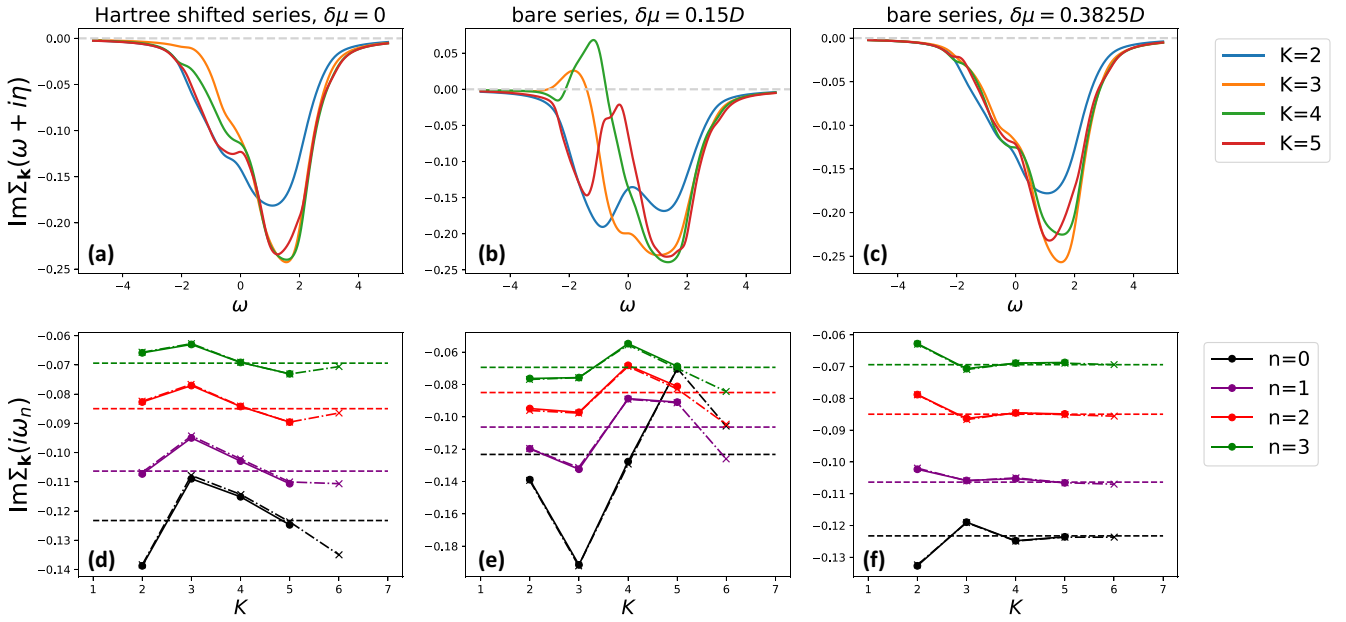

FIG. 3. DiagMC solution for the Hubbard model on a square lattice. Parameters of the model are $t' = -0.3t$, $\mu = 0$, $U = 1D$, and $T = 0.125D$, which corresponds to $\langle n_\sigma \rangle \approx 0.3625$. Top row: Imaginary part of self-energy at $\mathbf{k} = (\pi/4, \pi)$ on the real axis (with broadening $\eta = 0.3D$) obtained with three different series, up to perturbation order K. Bottom row: Illustration of convergence with respect to perturbation order K, using values of the imaginary part of the self-energy at the lowest four Matsubara frequencies, $i\omega_{n=0\ldots3}$. Full lines are our result, dash-dotted lines with crosses are the analogous result with a numerical τ-integration algorithm from Ref. [52], and horizontal dashed lines are the determinantal QMC result on a 16×16 lattice from Ref. [52].

The series can now be resummed as

$$\Sigma_{\mathbf{k}}^{(\mathrm{HF})}(z) = \sum_{K=2}^{\infty} \sum_{N=2}^{K} \sum_{L=0}^{K-N} \sum_{\substack{\{M_i^{L'}\}=0 \\ N+L+\sum_{i,L'} M_i^{L'}(N_i+L')=K}}^{K-N-L} (-U)^{N+\sum_{i,L'} M_i^{L'} N_i} (-\delta\mu)^{L+\sum_{i,L'} M_i^{L'} L'} \prod_{i,L'} \left(\mathcal{D}_i^{L'}\right)^{M_i^{L'}} \Omega\left(L, \{M_i^{L'}\}\right) \times \sum_{\Upsilon_N} D_{\Upsilon_N, \mathbf{k}, L+\sum_{i,L'} M_i^{L'}}(z), \tag{46}$$

where $\Omega(L, \{M_i^{L'}\})$ is the combinatorial prefactor which counts all the possible ways the selected single-particle vertices $\delta\mu, \{\mathcal{D}_i\}$ can be arranged. This corresponds to the number of permutations of the multisets,

$$\Omega\left(L, \{M_i^{L'}\}\right) = \frac{\left(L + \sum_{i,L'} M_i^{L'}\right)!}{L! \prod_{i,L'} M_i^{L'}!}. \tag{47}$$

We emphasize that Eq. (46) is fully general, but at orders $K \geqslant 5$, additional Hartree insertions $\mathcal{D}$ [compared to Eqs. (41)–(45)] need to be considered.

Finally, we stress that our analytical time-integral solution and action-shift tuning scheme in DiagMC are not restricted to the treatment of the Hubbard Hamiltonian. See Appendix F for a discussion of DiagMC in the case of a general Hamiltonian with two-body interactions.

IV. RESULTS

A. Convergence speedup with $\delta\mu$ expansion in the bare series

Here we focus on supplementing the results from Ref. [52] with real-frequency self-energies calculated without any numerically ill-defined analytical continuation.

The model parameters are $t' = -0.3t$, $\mu = 0$, $U = 1.0D$, $T = 0.125D$, and $\langle n_\sigma \rangle = 0.3625$. In Ref. [52], the calculation was performed with the Hartree-shifted series with $\delta\mu = 0$, as well as with the bare series, with two values of $\delta\mu$, namely, $0.15D$ and $0.3825D$. We repeat these calculations with our method. We use lattice size 32×32, and project the dispersion onto a uniform energy grid, as described in Ref. [48] and discussed in Sec. III C 2. In Fig. 3, we show our results and compare them with the results of Ref. [52].

In the upper row of Fig. 3 are the real-frequency self-energies calculated up to order $K \leqslant 5$. We are keeping a finite broadening $\eta = 0.3D$ to smoothen the curves. As discussed in Appendix B, in our method, numerical pole broadening is not a formal necessity. However, there is still a significant amount of statistical noise in our real-frequency result (although the imaginary-frequency result is already very well converged). It is important to note that some of the noisy features in our real-frequency result may be artifacts of the finite-lattice size that would not vanish with increasing number of MC steps. However, by comparing the result with a 256×256 lattice calculation (Appendix C), we check that already at $\eta = 0.2D$, no such artifact should be visible. It appears that for the given

external $\mathbf{k}$ and broadening $\eta = 0.2D$, increasing the lattice size further from 32×32 brings no new information, but it also does not present an additional cost: at $\eta = 0.2D$, our 256×256 lattice calculation appears equally well converged as the 32×32 lattice calculation, with the equal number of MC steps and a similar runtime, and yields a result that is on top of the 32×32 calculation.

In the bottom row of Fig. 3, we show the change in the imaginary part of the self-energy at the first four Matsubara frequencies, as a function of the maximal order K. Full-line and dots are the result of our calculations. The dash-dotted lines with crosses are data points taken from Ref. [52]. The horizontal dashed lines are the 16×16-lattice determinantal QMC result, also from Ref. [52].

The excellent agreement with the results from Ref. [52] serves as a stringent test of our implementation. In the $\delta\mu = 0.3825D$ calculation, even on the real axis, the self-energy does appear well converged by order $K = 5$, although there is some discrepancy between $K = 4$ and $K = 5$ at around $\omega = 1.5D$.

B. ω-resolved resummation

We can now go one step further by resumming the series presented in Figs. 3(a) and 3(c) for each ω individually, using an ω-dependent optimal shift $\delta\mu^*(\omega)$. The results are shown in Figs. 4 and 5.

We determine the optimal $\delta\mu^*(\omega)$ by minimizing the spread of the $\mathrm{Im}\Sigma(\omega + i\eta)$ results between orders $K = 3$ and $K = 5$. This spread as a function of ω and $\delta\mu$ is color plotted in Figs. 4 and 5. We have results for a discrete set of $\delta\mu \in \{\delta\mu_i\}$, so the optimal $\delta\mu^*(\omega)$ is *a priori* a discontinuous curve. As this is clearly nonsatisfactory, we smoothen the curve (shown with the blue line on the top panels in Figs. 4 and 5). However, we do not have results for each precise value of this optimal $\delta\mu^*(\omega)$. One could take, for each ω, the available $\delta\mu_i$ that is closest to $\delta\mu^*(\omega)$, but this would, again, result in a discontinuous curve. To avoid this, we average the available results as

$$\Sigma(\omega) = \frac{\sum_i \Delta\delta\mu_i \Sigma(\omega; \delta\mu_i) w(\delta\mu^*(\omega), \delta\mu_i)}{\sum_i \Delta\delta\mu_i w(\delta\mu^*(\omega), \delta\mu_i)}, \tag{48}$$

where $\Delta\delta\mu_i$ is the size of the $\delta\mu$ step in the available results at the ith value (allows for nonuniform grids). We use a narrow Gaussian weighting kernel,

$$w(\delta\mu^*(\omega), \delta\mu_i) = e^{-(\delta\mu_i - \delta\mu^*(\omega))^2/W^2}. \tag{49}$$

The width of the kernel W is chosen such that it is as narrow as possible, while still encompassing at least 3–4 $\delta\mu_i$ points, so that the final result is reasonably smooth as a function of ω; W is therefore determined according to the resolution in $\delta\mu$. We use $W = 0.05$ and $\Delta\delta\mu_i \approx 0.02$ and have checked that the results are insensitive to the precise choice of this numerical parameter.

The results of the averaging around the optimal $\delta\mu^*(\omega)$ are shown in the middle and bottom panels of Figs. 4 and 5. In both cases, the ω-resolved resummation helps to converge the result. In the case of the bare series, the convergence is now almost perfect, and already order $K = 3$ is on top of the exact result. In the case of the Hartree-shifted series, the results are

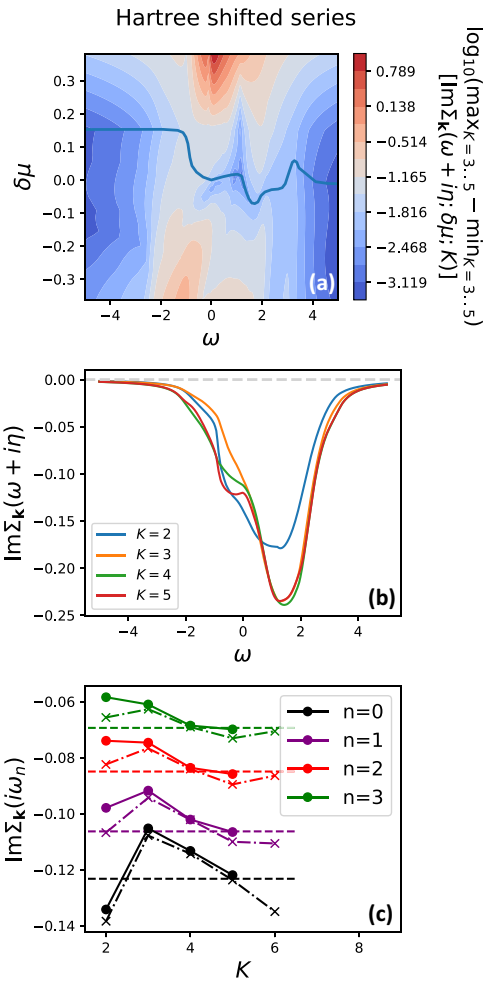

FIG. 4. Results of the Hartree-shifted series with ω-resolved resummation, to be compared to Figs. 3(a) and 3(d) (all parameters are the same). Top panel: Color plot of the spread of the imaginary part of the self-energy at a given $\omega + i\eta$ between orders $K = 3$ and 5, in a calculation with a given $\delta\mu$. The blue line smoothly connects the minima of the spread (at each ω), and defines the ω-dependent optimal shift $\delta\mu^*(\omega)$ used in the resummation. Middle and bottom panels are analogous to Figs. 3(a) and 3(d). In the bottom panel, the dash-dotted and dashed lines are the same as in Fig. 3(d).

not perfectly converged at $\omega < 0$, yet the $K = 5$ calculation is practically on top of the exact result on the imaginary axis, and presents an improvement to the $\delta\mu = 0$ series in Fig. 3(a). Note that the improvement in convergence is seen on the imaginary axis, as well.

C. Removing nonphysical features

In this section, we focus on the parameters case discussed in Ref. [48]. We calculate the Hartree-shifted series with parameters of the model $t' = 0$, $\mu - U\langle n_\sigma\rangle = -0.1D$, $T = 0.1D$, and employ various $\delta\mu$ shifts. The lattice size is again 32×32 and we focus on the self-energy at $\mathbf{k} = (0, \pi)$. Note that in Hartree-shifted series, the quantity that enters the calculation is $\mu - U\langle n_\sigma\rangle$, rather than μ. If $\langle n\rangle$ is calculated, μ can be estimated *a posteriori*. In our calculation, we fix

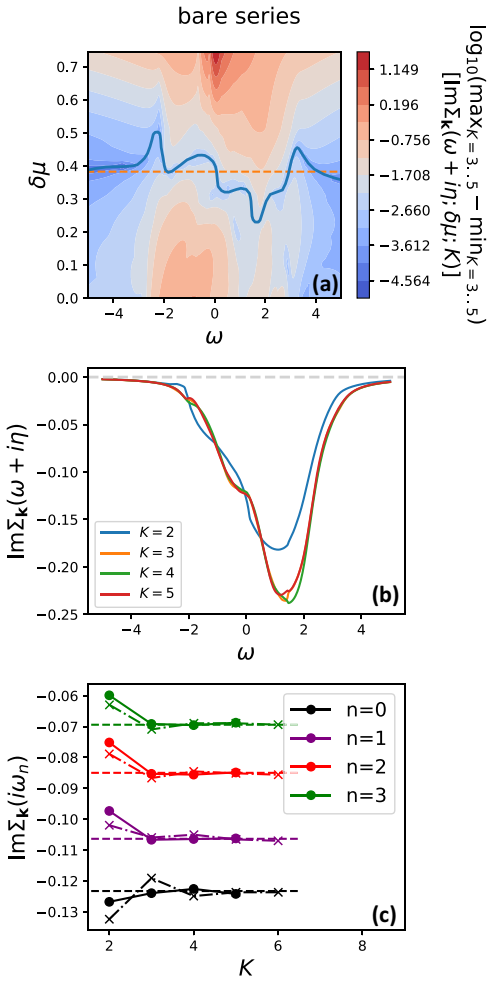

FIG. 5. Results of the bare series with ω-resolved resummation, to be compared to Figs. 3(c) and 3(f) (all parameters are the same). The top panel is analogous to Fig. 4(a). The horizontal orange dashed line denotes the value of $\delta\mu$ used in Figs. 3(c) and 3(f) to best converge the imaginary-axis result. The middle and bottom panels are analogous to Figs. 3(c) and 3(f). In the bottom panel, the dash-dotted and dashed lines are the same as in Fig. 3(f).

$\mu - U\langle n_\sigma\rangle$, and $\langle n_\sigma\rangle$ is then U dependent. Roughly, as given in Ref. [48], at $U = 1$, we have $\langle n_\sigma\rangle \approx 0.455$.

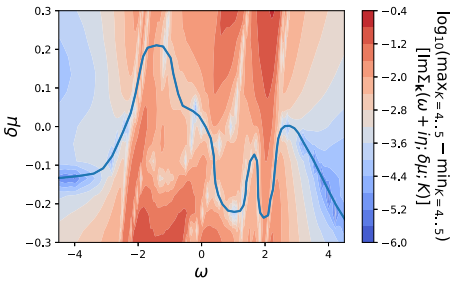

FIG. 7. Analogous to Fig. 4(a), for the parameters of the model corresponding to Fig. 6. The blue line is the optimal $\delta\mu^*$, to be used in Fig. 8.

The results are presented in Fig. 6 for three values of U. At low U, the series is well converged by $K = 5$, and the result is entirely insensitive to the choice of $\delta\mu$, as expected. At intermediate and high U, the result can be strongly $\delta\mu$ sensitive. The $\delta\mu$ dependence of the result, however, strongly varies with ω. It appears that for a given ω, there are ranges of the $\delta\mu$ value where the result (at fixed order K) is insensitive to the precise choice of $\delta\mu$. This presents an alternative way of choosing an optimal $\delta\mu$ (a similar idea was employed in a different context in Ref. [58]).

The striking feature at large U is the causality violations at $|\omega| \approx 2$ that were previously discussed in Ref. [48] (note that the broadening somewhat masks the extent of the problem). The dips in the self-energy spectrum appear to happen only at certain values of $\delta\mu$: at $\omega = -2$, the problem is present at $\delta\mu$ large and negative, and at $\omega = 2$, at $\delta\mu$ large and positive. In particular, at $\omega = 2$, the result appears to vary uniformly with $\delta\mu$, and one cannot select an optimal $\delta\mu$ based on the sensitivity of the result to the $\delta\mu$ value. We therefore repeat the procedure from the previous section and select the optimal $\delta\mu^*(\omega)$ based on the level of convergence between orders $K = 4$ and $K = 5$. The spread of the results and a smooth choice of $\delta\mu^*(\omega)$ are presented in Fig. 7.

In Fig. 8, the results of the averaging are shown and compared to the $\delta\mu = 0$ results at the highest available orders $K = 4$ and $K = 5$, at three values of U. The convergence is visibly better around our $\delta\mu^*$ than with $\delta\mu = 0$ at problematic frequencies $|\omega| \approx 2$. More importantly, the nonphysical features are clearly absent. At $U = 1$, in the $\delta\mu = 0$

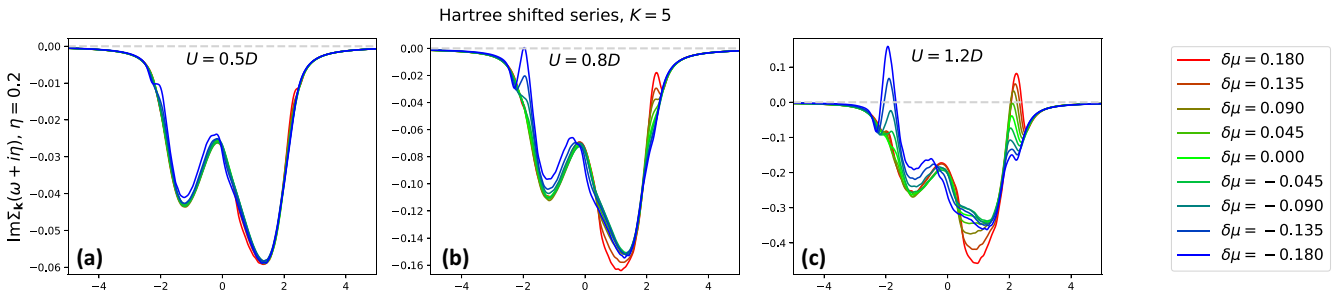

FIG. 6. Imaginary part of the self-energy on the real axis (with broadening η), at different values of coupling constant U, obtained with our method at $K = 5$ using different chemical-potential shifts $\delta\mu$. The parameters of the calculation are the same as in Ref. [48], i.e., $t' = 0$, $\mu - U\langle n_\sigma\rangle = -0.1D$, $T = 0.1D$. The self-energy is calculated at $\mathbf{k} = (0, \pi)$. Passing of the curves above the gray dashed line indicates breaking of causality.

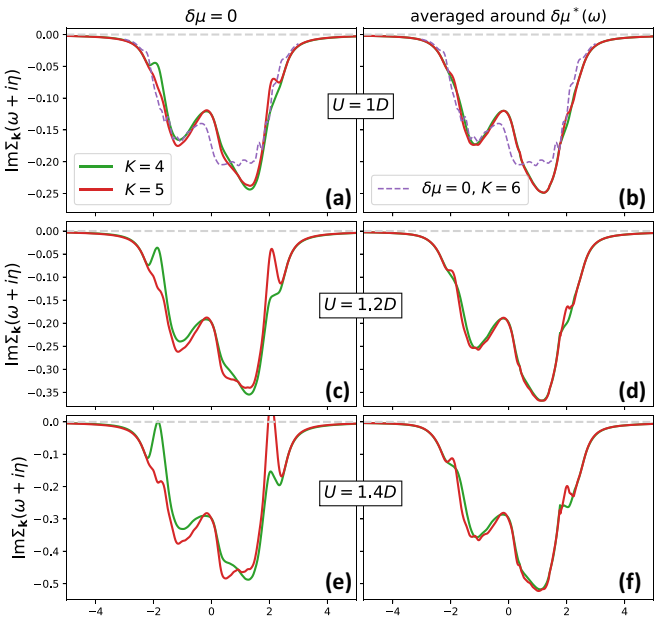

FIG. 8. Imaginary part of self-energy, real-frequency results (with broadening η). Right column: obtained with the ω-resolved resummation for the model parameters from Fig. 6, using the optimal $\delta\mu^*(\omega)$ from Fig. 7; to be compared to the standard $\delta\mu = 0$ calculation in the left column. Purple dashed lines in the top row are the $K = 6$ calculation with $\delta\mu = 0$.

calculation, the causality is not yet violated, but the dip at $\omega = 2$ is already starting to appear, which is clearly an artifact of the series truncation which should be removed systematically. It is important that the intermediate frequency behavior that we obtained by averaging results around the optimal $\delta\mu$ is indeed the correct one, and it will not change much further with increasing orders. We show in the top panels the $K = 6$, the $\delta\mu = 0$ result of which has been benchmarked against a fully converged imaginary-axis result in Fig. 9 (the converged result was obtained with the ΣDet method [59,60] at order

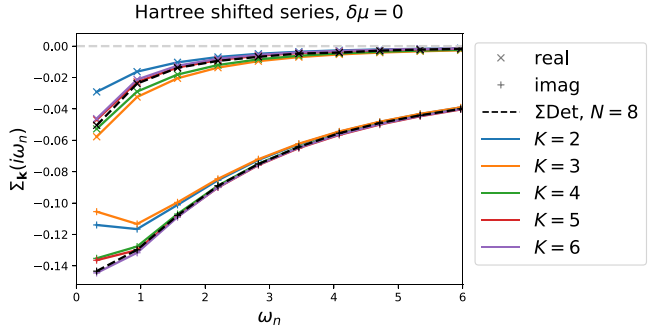

FIG. 9. Matsubara-frequency self-energy result, with model parameters as in Fig. 6. Crosses are the real part, pluses are the imaginary part, and lines are eye guides. Solid lines are the Hartree-shifted series with $\delta\mu = 0$ at different maximal K. The same result was obtained with both the algorithm presented in this work and the algorithmic Matsubara summation method from Ref. [48] (the two methods were compared diagram by diagram). Black dashed lines are the ΣDet result at maximal order $N = 8$.

8). Clearly, the improved convergence between orders 4 and 5 that we have achieved by choosing $\delta\mu$ appropriately does indeed mean an improved final result. However, our procedure does not improve the result at around $\omega = 0$, where the optimal $\delta\mu$ does appear to be close to 0. The $K = 6$, $\delta\mu = 0$ result shown in the upper panels of Fig. 8 is still a bit different from the $K = 5$, $\delta\mu \approx \delta\mu^*(\omega)$ results around $\omega = 0$.

In the case of $U = 1D$, it is interesting that a large negative $\delta\mu$ does bring the $\omega \approx 0$ result at order $K = 5$ much closer to the exact value. This can be anticipated from Fig. 6, where we show the corresponding results for $U = 0.8D$ and $U = 1.2D$. Also, by looking at the color plot in Fig. 7, we see that at $\omega = 0$, there is indeed a local minimum in the spread at around $\delta\mu = -0.2$, which could be used as the optimal $\delta\mu^*$. This minimum, however, cannot be continuously connected with the other minima that we observe at $\omega < 0$, so we chose a different trajectory in the $(\omega, \delta\mu)$ space. It would be interesting for future work to inspect the behavior at even more negative $\delta\mu$, where another continuous trajectory $\delta\mu^*(\omega)$ might be found.

V. DISCUSSION, CONCLUSIONS, AND PROSPECTS

In this paper, we have derived an analytical solution for the multiple-time integral that appears in the imaginary-time Feynman diagrams of an interaction series expansion. The solution is general for any diagram with a single external time or no external times. We find this generality to be a great advantage compared to the recently proposed algorithmic solutions of the corresponding Matsubara-frequency summations. Our analytical solution allowed us to develop a very flexible DiagMC algorithm that can make use of the possibility to optimize the series with shifted actions. As a result, we were able to almost perfectly converge a real-frequency self-energy in just 3–4 orders of perturbation, in a nontrivial regime and practically in the thermodynamic limit.

More importantly, the fact that one does not have to prepare a solution for each diagram topology individually opens the possibility to develop algorithms more akin to CTINT and allow the MC sampling to go to indefinite perturbation orders. In fact, upon a simple inspection of CTINT and continuous-time hybridization-expansion quantum Monte Carlo in the segment picture (segment-CTHYB) equations [42], it becomes clear that our solution can, in principle, be applied there, so as to reformulate these methods in real frequency. This would, however, come at the price of having to break into individual terms the determinant that captures all the contributions to the partition function at a given perturbation order. In turn, this may lead to a more significant sign problem, and an effective cap on the perturbation orders that can be handled in practice. On the other hand, it is not entirely clear how much of the sign problem comes from summing the individual terms and how much from the integration of the internal times, and we leave such considerations for future work. In any case, DiagMC algorithms based on hybridization expansion have been proposed before (see Refs. [23,28,61]), where our analytical solution may be applied.

Our solution also trivially generalizes to real-time integrals and may have use in Keldysh and Kadanoff-Baym [9]

calculations, where the infamous dynamical sign problem arises precisely due to oscillating time integrands. There have been recent works [62,63] with imaginary-time propagation of randomized walkers where our solution may also find application.

Finally, we emphasize that avoiding analytical continuation could be beneficial at high temperature where the Matsubara frequencies become distant from the real axis, and thus noisy imaginary-axis correlators contain little information [64,65]. The high-temperature regime is particularly relevant for optical lattice simulations of the Hubbard model [66]. In that context, we anticipate our method will find application in the calculation of conductivity and other response functions.

ACKNOWLEDGMENTS

We thank Fedor Šimkovic for useful discussions and for sharing his diagram topology data. Computations were performed on the PARADOX supercomputing facility (Scientific Computing Laboratory, Center for the Study of Complex Systems, Institute of Physics Belgrade) and the ALPHA cluster (Collège de France). This work was also granted access to the HPC resources of TGCC and IDRIS under the Allocations No. A0090510609 and No. A0070510609 attributed by GENCI (Grand Equipement National de Calcul Intensif). J.V. acknowledges funding provided by the Institute of Physics Belgrade, through the grant by the Ministry of Education, Science, and Technological Development of the Republic of Serbia, as well as by the Science Fund of the Republic of Serbia, under the Key2SM project (PROMIS program, Grant No. 6066160). M.F. acknowledges support by the Simons Foundation. We also acknowledge support by the European Research Council for the European Union Seventh Framework Program (FP7/2007-2013) with ERC Grant No. 319286 (QMAC).

APPENDIX A: REAL-TIME INTEGRATION

Let us consider the following special case of the integral given by Eq. (3), which is relevant for real-time integrations featuring integrands of the form e^{itE}:

$$\tilde{\mathcal{I}}_{\{l_2\ldots l_N\},\{E_2\ldots E_N\}}(t)=\prod_{i=2}^{N}\int_0^{t_{i+1}}dt_i\,t_i^{l_i}\,e^{it_iE_i}, \tag{A1}$$

with $t_{N+1}\equiv t$. This corresponds to the case $r\notin[2,N]$ in Eq. (3), and $\omega_i=iE_i$, and we will define $\tilde{E}_i$ analogously to $\tilde{\omega}_i$. The result is then obtained straightforwardly from Eq. (14),

$$\begin{aligned}\tilde{\mathcal{I}}_{\{l_2\ldots l_N\},\{E_2\ldots E_N\}}(t)=&\sum_{\{b_i\in[\delta_{\tilde{z}_i},1]\}_{i=2\ldots N}}e^{it\tilde{E}_Nb_N}\sum_{\{k_i\in[0,(1-\delta_{\tilde{z}_i})n_i]\}_{i:b_i=1}}\\&\times(-1)^{\sum_{i=2}^{N}k_i}\prod_{i:\delta_{\tilde{z}_i}=1}\frac{1}{n_i}\\&\times t^{n_N+1-b_N-k_N}\prod_{i:\tilde{E}_i\neq0}\frac{C_{n_i,k_i}}{(i\tilde{E}_i)^{k_i+b_i}},\end{aligned} \tag{A2}$$

which has the following general form:

$$\tilde{\mathcal{I}}(t)=\sum_{j;p\in\mathbb{N}_0}\mathcal{Z}_{p,j}t^pe^{it\mathcal{E}_j}. \tag{A3}$$

APPENDIX B: EXTRACTING REAL-AXIS RESULTS WITHOUT POLE BROADENING

In this section, we show how the results on the real axis can be extracted without any numerical broadening of the poles. Rather, we make use of the pole amplitudes by interpreting the result as being representative of the thermodynamic limit, where poles on the real axis merge into a branch cut, and thus we consider that the pole amplitude is a continuous function of the real frequency. We extract the imaginary part of the contribution [Im$D(\omega)$], and then the Hilbert transform can be used to reconstruct the real part.

The procedure relies on the following construction: A function $f(z)$ which is analytic everywhere in the upper half of the complex plane ($z^+=x+iy$ with $y>0$) and decays to zero with $|z^+|$ satisfies the relation

$$f(z^+)=-\frac{1}{\pi}\int dx'\frac{\mathrm{Im}f(x'+i0^+)}{z^+-x'}. \tag{B1}$$

After applying the pth derivative with respect to x (i.e., the real part of z^+) on both sides of the equation, one obtains

$$\begin{aligned}\partial_x^pf(z^+)&=-\frac{1}{\pi}\int dx'\partial_x^p\frac{\mathrm{Im}f(x'+i0^+)}{z^+-x'}\\&=-\frac{1}{\pi}\int dx'(-1)^p(p+1)!\frac{\mathrm{Im}f(x'+i0^+)}{(z^+-x')^{p+1}}.\end{aligned} \tag{B2}$$

We can now move the constant prefactors to the left-hand side and rename $p+1\to p$. Just above the real axis, we have

$$\frac{(-1)^p\pi}{p!}\partial_x^{p-1}f(x+i0^+)=\int dx'\frac{\mathrm{Im}f(x'+i0^+)}{(x-x'+i0^+)^p}. \tag{B3}$$

We can now discretize the expression on a uniform x grid with the step Δx, say, $x_j=j\Delta x$, and we see that the right-hand side has the form of a sum of poles of order p, equidistant along the real axis, and with amplitudes $\mathcal{A}_j=\mathrm{Im}f(x_j+i0^+)$,

$$\frac{(-1)^p\pi}{p!}\tilde{\partial}_j^{p-1}\mathcal{A}_j\approx\mathrm{Im}\sum_{j'}\Delta x\frac{\mathcal{A}_{j'}}{(x_j-x_{j'}+i0^+)^p}, \tag{B4}$$

where $\tilde{\partial}$ is the finite-difference approximation for the derivative along the x axis. Clearly, the imaginary part of the entire sum of p-order poles at a certain point x_j can be estimated by looking only at the $(p-1)$th derivative of the amplitudes of these poles at x_j, as given in the above expression.

The expression (B4) can be readily applied in our case [Eq. (33)] where the real axis is the frequency axis ω, with step $\Delta\omega$ and $\omega_j=j\Delta\omega$, and the sum of the poles determines our diagram contribution D. In general we have poles of various orders, but we can group the poles by order and treat their contributions separately. We therefore have

$$\mathrm{Im}D(\omega_j+i0^+)\approx\frac{\pi}{\Delta\omega}\sum_p\frac{(-1)^p}{p!}\tilde{\partial}_j^{p-1}\mathcal{A}_{j,p}. \tag{B5}$$

In the case of simple poles only, the contribution at any ω_j is simply proportional to the amplitude of the pole $\mathcal{A}_{j,1}$. Other-

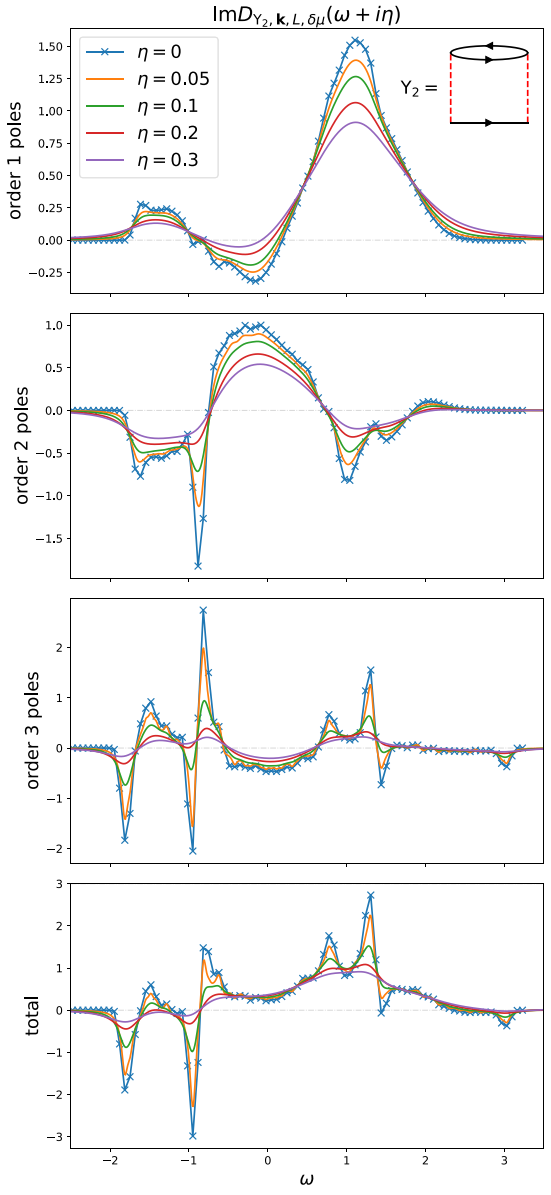

FIG. 10. Illustration of a $\eta = 0^+$ result obtained from Eq. (31) without any numerical broadening, based only on pole amplitudes. The diagram used is the second-order diagram (illustrated in the top panel), with $L = 2$. In the propagators, we take $\delta\mu = 0$. The rest of the parameters are $\mu - U\langle n_\sigma\rangle = -0.1D$, $T = 0.1D$, and the external momentum is $\mathbf{k} = (0, \pi)$. The top three panels are contributions from first-, second-, and third-order poles, respectively. The bottom panel is the total result. Lines with $\eta > 0$ are obtained with numerical broadening. The crosses on the $\eta = 0$ result denote the available frequencies (in between, we assume linear interpolation).

wise, the procedure requires that the pole amplitudes form a reasonably smooth function of the real frequency. Additionally, the energy resolution is a measure of the systematic error made in this procedure.

To avoid statistical noise and noisy features coming from the finite size of the lattice (see next section), we test our method on the example of a $N = 2$, $L = 2$ diagram, which we can solve with the full summation of Eq. (31), on a lattice

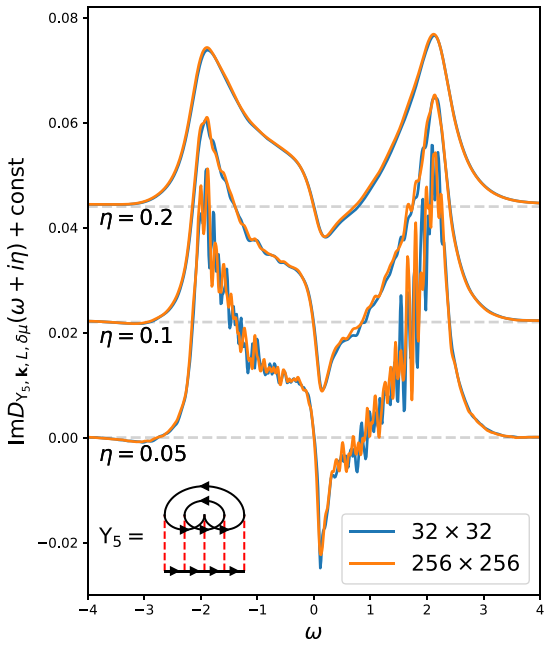

FIG. 11. Comparison of the real-frequency imaginary self-energy result for a single fifth-order diagram (illustrated in the bottom-left corner), for the lattice sizes 32×32 and 256×256, at three different levels of broadening. The calculation is in both cases performed with the same number of MC steps and took similar time. The parameters are $L = 0$, $\delta\mu = 0$, $\mu - U\langle n_\sigma\rangle = -0.1D$, $T = 0.1D$, and the external momentum is $\mathbf{k} = (0, \pi)$.

of the size 96×96. This diagram produces poles up to order 3. The result is shown in Fig. 10. In the first three panels, we show the contribution from the poles of each order, and in the bottom panel, we show the total result.

APPENDIX C: CONVERGENCE WITH LATTICE SIZE

In this section we discuss the convergence of the result with respect to the lattice size. In Fig. 11, we compare the results for a single $N = 5$, $L = 0$ diagram on the lattices of size 32×32 and 256×256. We observe that the result is almost exactly the same at broadening level $\eta = 0.2$, which brings further confidence in the results in the main part of the paper.

In Fig. 12, we illustrate how the size of the lattice determines the highest energy resolution that one can have, under requirement that the results form a continuous curve on the real axis and are, therefore, representative of the thermodynamic limit. We perform the full summation for the second-order diagram with $L = 0$, with various sizes of the lattice and various resolutions. Clearly, the bigger the lattice, the higher the energy resolution one can set without affecting the smoothness of the results.

The numerical parameters of the calculation are therefore the size of the lattice, the energy resolution, and the broadening (the resolution and the broadening can be tuned *a posteriori*), and one can tune them to get the optimal ratio between performance and the error bar. If the pole amplitudes $\mathcal{A}_{jp}$ are a relatively smooth function of j, no broadening is then needed at all.

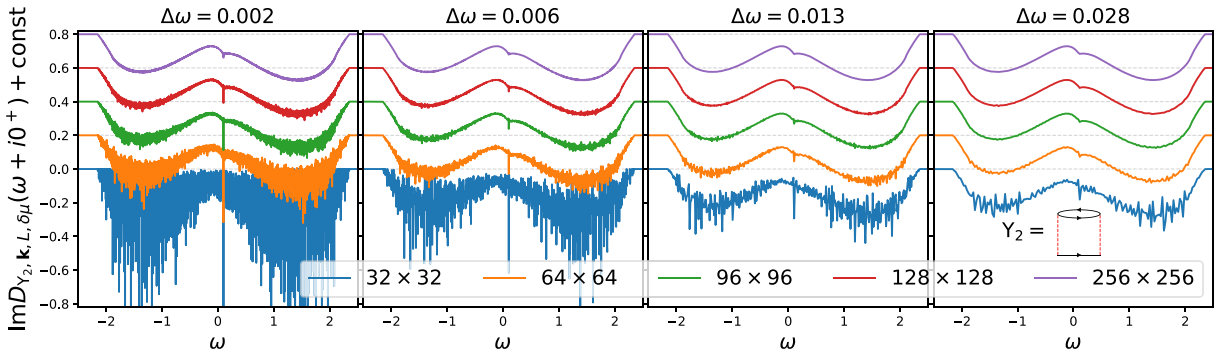

FIG. 12. Real-frequency result ($\eta = 0^+$) for the contribution of the lowest-order diagram (illustrated in the rightmost panel) at various lattice sizes and frequency resolutions, obtained with full summation (gray code). The step of the uniform energy grid is denoted $\Delta\omega$. The parameters are $L = 0$, $\delta\mu = 0$, $\mu - U\langle n_\sigma\rangle = -0.1D$, $T = 0.1D$, and the external momentum is $\mathbf{k} = (0, \pi)$.

APPENDIX D: DERIVATION OF EQ. (5)

After applying n times the partial integration over the integral from the left-hand side of Eq. (5), we get

$$\begin{aligned}
\int_0^{\tau_f} \tau^n e^{\tau z} d\tau &= \frac{1}{z^{n+1}} \int_0^{z\tau_f} \tau^n e^{\tau} d\tau \\
&= \frac{1}{z^{n+1}} \left[e^{z\tau_f}(z\tau_f)^n - n e^{z\tau_f}(z\tau_f)^{n-1} + \cdots + (-1)^n n! \int_0^{z\tau_f} \tau^0 e^{\tau} d\tau \right] \\
&= \frac{1}{z^{n+1}} \left[\frac{n!}{(n-0)!}(-1)^0 e^{z\tau_f}(z\tau_f)^{n-0} + (-1)^1 \frac{n!}{(n-1)!} e^{z\tau_f}(z\tau_f)^{n-1} + \cdots + (-1)^n \frac{n!}{(n-n)!} \int_0^{z\tau_f} \tau^0 e^{\tau} d\tau \right] \\
&= \frac{1}{z^{n+1}} \left[\frac{n!}{(n-0)!}(-1)^0 e^{z\tau_f}(z\tau_f)^{n-0} + (-1)^1 \frac{n!}{(n-1)!} e^{z\tau_f}(z\tau_f)^{n-1} + \cdots + (-1)^n \frac{n!}{(n-n)!} (z\tau_f)^0 (e^{z\tau_f} - 1) \right] \\
&= \frac{1}{z^{n+1}} e^{z\tau_f} \sum_{k=0}^{n} (-1)^k (z\tau_f)^{n-k} \frac{n!}{(n-k)!} - (-1)^n \frac{n!}{z^{n+1}},
\end{aligned} \tag{D1}$$

which can be readily identified with the right-hand side of Eq. (5).

APPENDIX E: DERIVATION OF EQ. (21)

We are looking for a solution of the Fourier transform

$$G_0^l(\varepsilon, \tau) = \frac{1}{\beta} \sum_{i\Omega_\eta} \frac{e^{-i\Omega_\eta \tau}}{(i\Omega_\eta - \varepsilon)^l}. \tag{E1}$$

For any τ, we can express the sum above as a contour integral, and we find

$$\begin{aligned}
G_0^l(\varepsilon, \tau) &= -\mathrm{Res}_{z=\varepsilon} \frac{e^{-z\tau}}{(z-\varepsilon)^l} \frac{\eta^{\lfloor \frac{\tau}{\beta} \rfloor} e^{\lfloor \frac{\tau}{\beta} \rfloor \beta z}}{1 - \eta e^{-\beta z}} dz \\
&= -\frac{\eta^{\lfloor \frac{\tau}{\beta} \rfloor}}{(l-1)!} \frac{d^{l-1}}{dz^{l-1}} \frac{e^{-\beta z \{\frac{\tau}{\beta}\}}}{1 - \eta e^{-\beta z}} \bigg|_{z=\varepsilon},
\end{aligned} \tag{E2}$$

where $\lfloor \ldots \rfloor$ denotes the integer part (floor function), and $\{x\} \equiv x - \lfloor x \rfloor$ denotes the fractional part.

We see that it will be useful to have an expression for derivatives of $(1 - \eta e^z)^{-1}$. They have the general form

$$\frac{d^k}{dz^k} \frac{1}{1 - \eta e^z} = \sum_{n=0}^{k} C_n^k \frac{(e^z)^n}{(1 - \eta e^z)^{n+1}}. \tag{E3}$$

By deriving this expression on both sides, one obtains a recursion for the coefficients C_n^k,

$$C_n^{k+1} = n C_n^k + \eta n C_{n-1}^k, \tag{E4}$$

with holds for $k > -1$ and $n > 0$ with $C_0^0 = 1$. That can be rewritten

$$\frac{\eta^n}{n!} C_n^{k+1} = n \frac{\eta^n}{n!} C_n^k + \frac{\eta^{n-1}}{(n-1)!} C_{n-1}^k. \tag{E5}$$

If we define $S_n^k = \frac{\eta^n}{n!} C_n^k$, we have the recursion $S_n^{k+1} = n S_n^k + S_{n-1}^k$, which is the recursion for the Stirling numbers of the second kind. This allows one to have the following important result:

$$\begin{aligned}
\frac{d^k}{dz^k} \frac{1}{1 - \eta e^z} &= \sum_{n=0}^{k} \eta^n n! \left\{ {k \atop n} \right\} \frac{(e^z)^n}{(1 - \eta e^z)^{n+1}} \\
&= \sum_{n=0}^{k} \eta^n n! \left\{ {k \atop n} \right\} \frac{e^{-z}}{(e^{-z} - \eta)^{n+1}}.
\end{aligned} \tag{E6}$$

With this, one obtains the following expression:

$$G_0^l(\varepsilon,\tau) = -e^{\varepsilon\beta(1-\{\frac{\tau}{\beta}\})}\eta^{\lfloor\frac{\tau}{\beta}\rfloor+1}(-\beta)^{l-1} \times \sum_{m=0}^{l-1}\sum_{n=0}^{l-m-1}\frac{n!}{(l-m-1)!m!}\left\{\begin{matrix} l-m-1 \\ n \end{matrix}\right\} \times \left(\frac{1}{\eta e^{\varepsilon\beta}-1}\right)^{n+1}\left\{\frac{\tau}{\beta}\right\}^m, \tag{E7}$$

which already satisfies the (anti)periodicity properties of the Green's function.

To make use of the result given by Eq. (E7), we need to express $G_0^l(\varepsilon,\tau)$ as a function of two times $G_0^l(\varepsilon,\tau,\tau') \equiv G_0^l(\varepsilon,\tau-\tau')$, with $\tau,\tau' \in [0,\beta]$. We first consider $\tau \geqslant \tau'$. By substituting $(\tau-\tau')^m = \sum_{\zeta=0}^m (-1)^{m-\zeta}\binom{m}{\zeta}\tau^\zeta\tau'^{m-\zeta}$ into Eq. (E7) and substituting $m-\zeta$ with ς, we get

$$G_0^l(\varepsilon,\tau-\tau') = \eta e^{\varepsilon(\tau'-\tau)}n_\eta(-\varepsilon)\sum_{\zeta=0}^{l-1}\sum_{\varsigma=0}^{l-\zeta-1} c^-_{l,\zeta,\varsigma}(\varepsilon)\tau^\zeta\tau'^\varsigma, \tag{E8}$$

with $c^-_{l,\zeta,\varsigma}(\varepsilon)$ as defined in Eq. (22). The result for $\tau < \tau'$ can then be easily obtained by proving the property $G_0^l(\varepsilon,\tau) = (-1)^l G_0^l(-\varepsilon,-\tau)$,

$$\begin{aligned} G_0^l(\varepsilon,-\tau) &= \frac{1}{\beta}\sum_{n=-\infty}^{\infty}\frac{e^{i\Omega_\eta\tau}}{(i\Omega_\eta-\varepsilon)^l} \\ &= \frac{1}{\beta}\sum_{n=-\infty}^{\infty}\frac{e^{-i\Omega_\eta\tau}}{(-i\Omega_\eta-\varepsilon)^l} \\ &= (-1)^l\frac{1}{\beta}\sum_{n=-\infty}^{\infty}\frac{e^{-i\Omega_\eta\tau}}{(i\Omega_\eta+\varepsilon)^l} \\ &= (-1)^l G_0^l(-\varepsilon,\tau), \end{aligned}$$

which implies that in the definition (21), we must have

$$c^+_{l,\zeta,\varsigma}(\varepsilon) = (-1)^{l-1}c^-_{l,\varsigma,\zeta}(-\varepsilon). \tag{E9}$$

APPENDIX F: GENERAL HAMILTONIAN CASE

It is important to show that our method is not restricted to a specific choice of Hamiltonian. The local density-density interaction and the single band of the Hubbard Hamiltonian bring many simplifications, but none of them are necessary for our imaginary-time integral solution or the chemical-potential tuning scheme.

Consider the general Hamiltonian

$$H = \sum_\alpha(\varepsilon_\alpha-\mu) + \sum_{\alpha_1\alpha_2\alpha_3\alpha_4}U_{\alpha_1\alpha_2\alpha_3\alpha_4}c^\dagger_{\alpha_1}c_{\alpha_2}c^\dagger_{\alpha_3}c_{\alpha_4}. \tag{F1}$$

The α are the eigenstates of the noninteracting Hamiltonian, e.g., a combined momentum, band, and spin index. The self-energy can be now expressed as a series,

$$\Sigma^{(\mathrm{HF})}_{\alpha,\alpha'}(\tau) = \sum_N\sum_{\Upsilon_N}\prod_{j=1}^{2N-1}\sum_{l_j=1}^{\infty}\sum_{\alpha_{j,1}\ldots\alpha_{j,l_j}}\prod_{n=1}^{l_j-1}\sum_{\mathbf{V}_{j,n}} \times [\mathbf{V}_{j,n}]_{\alpha_{j,n}\alpha_{j,n+1}}\prod_{i=1}^{N}U_{\alpha_{j_1}(i)\alpha_{j_2}(i)\alpha_{j_3}(i)\alpha_{j_4}(i)} \times \prod_{m=1}^{N-1+\sum_j(l_j-1)}\int_0^\beta d\tau_m\, G_0\big(\bar\varepsilon_{\alpha_{j,n}},\tilde\tau_{j,n}-\tilde\tau'_{j,n}\big). \tag{F2}$$

Similarly as before, Υ_N enumerates topologies without any instantaneous insertions (Hartree or chemical potential) at perturbation order N (the number of interaction vertices). The fermionic lines in the Υ_N topology are enumerated with j. On each fermionic line, we make any number l_j-1 of instantaneous insertions with amplitudes $\mathbf{V}_{j,n}$ (interaction amplitudes in Hartree insertions are included in $\mathbf{V}$; n enumerates the insertions at the fermionic line j). In general, Hartree insertions may contain off-diagonal terms in the α basis and are therefore a matrix in the α space. However, it is necessary that chemical-potential shifts are diagonal in this basis, as we want to have the bare propagator diagonal in this basis as well. Otherwise, the form of G_0 from Eq. (18) would no longer hold. Nevertheless, one may still have a separate chemical-potential shift for each state, $\delta\mu_\alpha$. After making insertions, the number of fermionic lines increases to $\sum_j l_j$. The fermionic lines are now enumerated with j,n, and the corresponding states are $\alpha_{j,n}$. The index i enumerates the interaction vertices outside of any Hartree insertions. We denote $\alpha_{j_{1\ldots4}}(i)$ as the single-particle states at four terminals of each interaction vertex. The interaction vertices at incoming ($i=1$) and outgoing ($i=N$) terminals of the self-energy diagram are $\alpha_{j_1}(i=N)=\alpha$, $\alpha_{j_2}(i=1)=\alpha'$. With m, we enumerate all times to be integrated over. With each interaction vertex $i>1$, we associate one time, and there is a time associated to each instantaneous insertion of which there are $\sum_j(l_j-1)$. We assume that the incoming time corresponding to the vertex $i=1$ is 0. The times on the terminals of each bare propagator j,n are $\tilde\tau_{j,n}$ and $\tilde\tau'_{j,n}$ and they take on values from the set $\{\tau_m\}_{m=0\ldots N-1+\sum_j(l_j-1)}$, with the external incoming time fixed, $\tau_0\equiv 0$. $\tilde\tau_{j,n}$, $\tilde\tau'_{j,n}$, and $\alpha_{j_{1\ldots4}}(i)$ are implicit functions of topology Υ_N. Finally, $\bar\varepsilon_{\alpha_{j,n}} \equiv \varepsilon_{\alpha_{j,n}}-\mu+\delta\mu_{\alpha_{j,n}}$. We can now focus only on the time-integral part and proceed completely analogously to Eqs. (27)–(31).

It is worth noting that with general interactions, pulling the coupling constant in front of the diagram contribution is impossible, as the frequency dependence of the contribution of each diagram will depend on the precise form of $U_{\alpha_1\alpha_2\alpha_3\alpha_4}$. In the most general case, one must set specific values for $U_{\alpha_1\alpha_2\alpha_3\alpha_4}$ and $\delta\mu_\alpha$ before performing the Monte Carlo summation. One can then choose the variables that will be sampled stochastically and the ones that will be fully summed over. In the end, the contributions can be easily grouped by total number of independent times (K), including those in Hartree insertions. The integration of times in Hartree insertions can always be performed beforehand. Therefore, in the fully

general case, the number of integrations to be performed at the time of Monte Carlo sampling is $N-1+\sum_j(l_j-1)$. In the case of purely density-density interactions (as is the case in the Hubbard model) or spin-spin interactions in the absence of external magnetic fields, this simplifies further because instantaneous insertions lead to expressions of the type $\frac{1}{(i\omega-\varepsilon)^l}$ for which we can work out the temporal Fourier transform analytically [Eq. (21)] and the remaining number of integrations to perform is $N-1$ [as we do in Eq. (31)]. In the general case, when Hartree insertions are not diagonal in the α basis, one has expressions of the type $\frac{1}{i\omega-\varepsilon_1}\frac{1}{i\omega-\varepsilon_2}\cdots\frac{1}{i\omega-\varepsilon_l}$. In principle, one could prepare the analytical Fourier transforms for a general function of this form, but it might be increasingly involved at large l, so we assume one would do these integrations at the level of the Monte Carlo, when $\varepsilon_{1\ldots l}$ are already specified.

We finally emphasize that even more general constructions are possible, even in bases other than the noninteracting eigenbasis. In such cases, the G_0's are nondiagonal and may have a continuous real-frequency dependence, instead of being a single pole. We leave such considerations for future work.

[1] The Hubbard model at half a century, Nat. Phys. **9**, 523 (2013).

[2] J. P. F. LeBlanc, A. E. Antipov, F. Becca, I. W. Bulik, Garnet Kin-Lic Chan, Chia-Min Chung, Y. Deng, M. Ferrero, T. M. Henderson, C. A. Jiménez-Hoyos, E. Kozik, Xuan-Wen Liu, A. J. Millis, N. V. Prokof'ev, M. Qin, G. E. Scuseria, Hao Shi, B. V. Svistunov, L. F. Tocchio, I. S. Tupitsyn, S. R. White, S. Zhang, Bo-Xiao Zheng, Z. Zhu, and E. Gull (Simons Collaboration on the Many-Electron Problem), Solutions of the Two-Dimensional Hubbard Model: Benchmarks and Results from a Wide Range of Numerical Algorithms, Phys. Rev. X **5**, 041041 (2015).

[3] G. Rohringer, H. Hafermann, A. Toschi, A. A. Katanin, A. E. Antipov, M. I. Katsnelson, A. I. Lichtenstein, A. N. Rubtsov, and K. Held, Diagrammatic routes to nonlocal correlations beyond dynamical mean field theory, Rev. Mod. Phys. **90**, 025003 (2018).

[4] T. Schäfer, N. Wentzell, F. Šimkovic, Y.-Y. He, C. Hille, M. Klett, C. J. Eckhardt, B. Arzhang, V. Harkov, F.-M. Le Régent, A. Kirsch, Y. Wang, A. J. Kim, E. Kozik, E. A. Stepanov, A. Kauch, S. Andergassen, P. Hansmann, D. Rohe, Y. M. Vilk, J. P. F. LeBlanc, S. Zhang, A.-M. S. Tremblay, M. Ferrero, O. Parcollet, and A. Georges, Tracking the Footprints of Spin Fluctuations: A MultiMethod, MultiMessenger Study of the Two-Dimensional Hubbard Model, Phys. Rev. X **11**, 011058 (2021).

[5] A. W. Sandvik, Stochastic method for analytic continuation of quantum Monte Carlo data, Phys. Rev. B **57**, 10287 (1998).

[6] O. F. Syljuåsen, Using the average spectrum method to extract dynamics from quantum Monte Carlo simulations, Phys. Rev. B **78**, 174429 (2008).

[7] S. Fuchs, T. Pruschke, and M. Jarrell, Analytic continuation of quantum Monte Carlo data by stochastic analytical inference, Phys. Rev. E **81**, 056701 (2010).

[8] K. Ghanem and E. Koch, Extending the average spectrum method: Grid point sampling and density averaging, Phys. Rev. B **102**, 035114 (2020).

[9] H. Aoki, N. Tsuji, M. Eckstein, M. Kollar, T. Oka, and P. Werner, Nonequilibrium dynamical mean-field theory and its applications, Rev. Mod. Phys. **86**, 779 (2014).

[10] J. K. Freericks, Quenching Bloch oscillations in a strongly correlated material: Nonequilibrium dynamical mean-field theory, Phys. Rev. B **77**, 075109 (2008).

[11] M. Eckstein and M. Kollar, Nonthermal Steady States after an Interaction Quench in the Falicov-Kimball Model, Phys. Rev. Lett. **100**, 120404 (2008).

[12] M. Schiró and M. Fabrizio, Real-time diagrammatic Monte Carlo for nonequilibrium quantum transport, Phys. Rev. B **79**, 153302 (2009).

[13] P. Werner, T. Oka, and A. J. Millis, Diagrammatic Monte Carlo simulation of nonequilibrium systems, Phys. Rev. B **79**, 035320 (2009).

[14] M. Eckstein, M. Kollar, and P. Werner, Thermalization after an Interaction Quench in the Hubbard Model, Phys. Rev. Lett. **103**, 056403 (2009).

[15] M. Schiró and M. Fabrizio, Time-Dependent Mean Field Theory for Quench Dynamics in Correlated Electron Systems, Phys. Rev. Lett. **105**, 076401 (2010).

[16] P. Werner, T. Oka, M. Eckstein, and A. J. Millis, Weak-coupling quantum Monte Carlo calculations on the Keldysh contour: Theory and application to the current-voltage characteristics of the Anderson model, Phys. Rev. B **81**, 035108 (2010).

[17] M. Eckstein and P. Werner, Nonequilibrium dynamical mean-field calculations based on the noncrossing approximation and its generalizations, Phys. Rev. B **82**, 115115 (2010).

[18] M. Schiró and M. Fabrizio, Quantum quenches in the Hubbard model: Time-dependent mean-field theory and the role of quantum fluctuations, Phys. Rev. B **83**, 165105 (2011).

[19] P. Werner and M. Eckstein, Phonon-enhanced relaxation and excitation in the Holstein-Hubbard model, Phys. Rev. B **88**, 165108 (2013).

[20] M. Eckstein and P. Werner, Nonequilibrium dynamical mean-field simulation of inhomogeneous systems, Phys. Rev. B **88**, 075135 (2013).

[21] G. Cohen, D. R. Reichman, A. J. Millis, and E. Gull, Green's functions from real-time bold-line Monte Carlo, Phys. Rev. B **89**, 115139 (2014).

[22] G. Cohen, E. Gull, D. R. Reichman, and A. J. Millis, Green's Functions from Real-Time Bold-Line Monte Carlo Calculations: Spectral Properties of the Nonequilibrium Anderson Impurity Model, Phys. Rev. Lett. **112**, 146802 (2014).

[23] G. Cohen, E. Gull, D. R. Reichman, and A. J. Millis, Taming the Dynamical Sign Problem in Real-Time Evolution of Quantum Many-Body Problems, Phys. Rev. Lett. **115**, 266802 (2015).

[24] N. V. Prokof'ev and B. V. Svistunov, Polaron Problem by Diagrammatic Quantum Monte Carlo, Phys. Rev. Lett. **81**, 2514 (1998).

[25] A. S. Mishchenko, N. V. Prokof'ev, A. Sakamoto, and B. V. Svistunov, Diagrammatic quantum Monte Carlo study of the Fröhlich polaron, Phys. Rev. B **62**, 6317 (2000).

[26] N. Prokof'ev and B. Svistunov, Bold Diagrammatic Monte Carlo Technique: When the Sign Problem Is Welcome, Phys. Rev. Lett. **99**, 250201 (2007).

[27] N. V. Prokof'ev and B. V. Svistunov, Bold diagrammatic Monte Carlo: A generic sign-problem tolerant technique for polaron models and possibly interacting many-body problems, Phys. Rev. B **77**, 125101 (2008).

[28] E. Gull, D. R. Reichman, and A. J. Millis, Bold-line diagrammatic Monte Carlo method: General formulation and application to expansion around the noncrossing approximation, Phys. Rev. B **82**, 075109 (2010).

[29] E. Kozik, K. Van Houcke, E. Gull, L. Pollet, N. Prokof'ev, B. Svistunov, and M. Troyer, Diagrammatic Monte Carlo for correlated fermions, Europhys. Lett. **90**, 10004 (2010).

[30] K. V. Houcke, E. Kozik, N. Prokof'ev, and B. Svistunov, Diagrammatic Monte Carlo, Phys. Proc. **6**, 95 (2010).

[31] L. Pollet, Recent developments in quantum Monte Carlo simulations with applications for cold gases, Rep. Prog. Phys. **75**, 094501 (2012).

[32] K. Van Houcke, F. Werner, E. Kozik, N. Prokof'ev, B. Svistunov, M. J. H. Ku, A. T. Sommer, L. W. Cheuk, A. Schirotzek, and M. W. Zwierlein, Feynman diagrams versus Fermi-gas Feynman emulator, Nat. Phys. **8**, 366 (2012).

[33] S. A. Kulagin, N. Prokof'ev, O. A. Starykh, B. Svistunov, and C. N. Varney, Bold Diagrammatic Monte Carlo Method Applied to Fermionized Frustrated Spins, Phys. Rev. Lett. **110**, 070601 (2013).

[34] S. A. Kulagin, N. Prokof'ev, O. A. Starykh, B. Svistunov, and C. N. Varney, Bold diagrammatic Monte Carlo technique for frustrated spin systems, Phys. Rev. B **87**, 024407 (2013).

[35] R. Rossi, T. Ohgoe, E. Kozik, N. Prokof'ev, B. Svistunov, K. Van Houcke, and F. Werner, Contact and Momentum Distribution of the Unitary Fermi Gas, Phys. Rev. Lett. **121**, 130406 (2018).

[36] R. Rossi, Determinant Diagrammatic Monte Carlo Algorithm in the Thermodynamic Limit, Phys. Rev. Lett. **119**, 045701 (2017).

[37] K. Van Houcke, F. Werner, T. Ohgoe, N. V. Prokof'ev, and B. V. Svistunov, Diagrammatic Monte Carlo algorithm for the resonant Fermi gas, Phys. Rev. B **99**, 035140 (2019).

[38] K. Chen and K. Haule, A combined variational and diagrammatic quantum Monte Carlo approach to the many-electron problem, Nat. Commun. **10**, 3725 (2019).

[39] A. N. Rubtsov and A. I. Lichtenstein, Continuous-time quantum Monte Carlo method for fermions: Beyond auxiliary field framework, J. Expt. Theor. Phys. Lett. **80**, 61 (2004).

[40] A. N. Rubtsov, V. V. Savkin, and A. I. Lichtenstein, Continuous-time quantum Monte Carlo method for fermions, Phys. Rev. B **72**, 035122 (2005).

[41] E. Gull, P. Werner, O. Parcollet, and M. Troyer, Continuous-time auxiliary-field Monte Carlo for quantum impurity models, Europhys. Lett. **82**, 57003 (2008).

[42] E. Gull, A. J. Millis, A. I. Lichtenstein, A. N. Rubtsov, M. Troyer, and P. Werner, Continuous-time Monte Carlo methods for quantum impurity models, Rev. Mod. Phys. **83**, 349 (2011).

[43] R. E. V. Profumo, C. Groth, L. Messio, O. Parcollet, and X. Waintal, Quantum Monte Carlo for correlated out-of-equilibrium nanoelectronic devices, Phys. Rev. B **91**, 245154 (2015).

[44] A. Moutenet, P. Seth, M. Ferrero, and O. Parcollet, Cancellation of vacuum diagrams and the long-time limit in out-of-equilibrium diagrammatic quantum Monte Carlo, Phys. Rev. B **100**, 085125 (2019).

[45] C. Bertrand, O. Parcollet, A. Maillard, and X. Waintal, Quantum Monte Carlo algorithm for out-of-equilibrium Green's functions at long times, Phys. Rev. B **100**, 125129 (2019).

[46] C. Bertrand, S. Florens, O. Parcollet, and X. Waintal, Reconstructing Nonequilibrium Regimes of Quantum Many-Body Systems from the Analytical Structure of Perturbative Expansions, Phys. Rev. X **9**, 041008 (2019).

[47] A. Taheridehkordi, S. H. Curnoe, and J. P. F. LeBlanc, Algorithmic Matsubara integration for Hubbard-like models, Phys. Rev. B **99**, 035120 (2019).

[48] J. Vučičević and M. Ferrero, Real-frequency diagrammatic Monte Carlo at finite temperature, Phys. Rev. B **101**, 075113 (2020).

[49] A. Taheridehkordi, S. H. Curnoe, and J. P. F. LeBlanc, Optimal grouping of arbitrary diagrammatic expansions via analytic pole structure, Phys. Rev. B **101**, 125109 (2020).

[50] A. Taheridehkordi, S. H. Curnoe, and J. P. F. LeBlanc, Algorithmic approach to diagrammatic expansions for real-frequency evaluation of susceptibility functions, Phys. Rev. B **102**, 045115 (2020).

[51] M. Maček, P. T. Dumitrescu, C. Bertrand, B. Triggs, O. Parcollet, and X. Waintal, Quantum Quasi-Monte Carlo Technique for Many-Body Perturbative Expansions, Phys. Rev. Lett. **125**, 047702 (2020).

[52] W. Wu, M. Ferrero, A. Georges, and E. Kozik, Controlling Feynman diagrammatic expansions: Physical nature of the pseudogap in the two-dimensional Hubbard model, Phys. Rev. B **96**, 041105(R) (2017).

[53] R. Rossi, F. Šimkovic IV, and M. Ferrero, Renormalized perturbation theory at large expansion orders, Europhys. Lett. **132**, 11001 (2020).

[54] F. Šimkovic IV, R. Rossi, and M. Ferrero, Efficient one-loop-renormalized vertex expansions with connected determinant diagrammatic Monte Carlo, Phys. Rev. B **102**, 195122 (2020).

[55] F. Šimkovic IV, J. P. F. LeBlanc, A. J. Kim, Y. Deng, N. V. Prokof'ev, B. V. Svistunov, and E. Kozik, Extended Crossover from a Fermi Liquid to a Quasiantiferromagnet in the Half-Filled 2D Hubbard Model, Phys. Rev. Lett. **124**, 017003 (2020).

[56] A. J. Kim, F. Šimkovic IV, and E. Kozik, Spin and Charge Correlations across the Metal-to-Insulator Crossover in the Half-Filled 2D Hubbard Model, Phys. Rev. Lett. **124**, 117602 (2020).

[57] C. Lenihan, A. J. Kim, F. Šimkovic IV., and E. Kozik, Entropy in the Non-Fermi-Liquid Regime of the Doped 2D Hubbard Model, Phys. Rev. Lett. **126**, 105701 (2021).

[58] T. Ayral, J. Vučičević, and O. Parcollet, Fierz Convergence Criterion: A Controlled Approach to Strongly Interacting Systems with Small Embedded Clusters, Phys. Rev. Lett. **119**, 166401 (2017).

[59] A. Moutenet, W. Wu, and M. Ferrero, Determinant Monte Carlo algorithms for dynamical quantities in fermionic systems, Phys. Rev. B **97**, 085117 (2018).

[60] F. Šimkovic IV and E. Kozik, Determinant Monte Carlo for irreducible Feynman diagrams in the strongly correlated regime, Phys. Rev. B **100**, 121102(R) (2019).

[61] E. Eidelstein, E. Gull, and G. Cohen, Multiorbital Quantum Impurity Solver for General Interactions and Hybridizations, Phys. Rev. Lett. **124**, 206405 (2020).

[62] A. A. Kunitsa and So Hirata, Grid-based diffusion Monte Carlo for fermions without the fixed-node approximation, Phys. Rev. E **101**, 013311 (2020).

[63] M. Hutcheon, Stochastic nodal surfaces in quantum Monte Carlo calculations, Phys. Rev. E **102**, 042105 (2020).

[64] J. Vučičević, J. Kokalj, R. Žitko, N. Wentzell, D. Tanasković, and J. Mravlje, Conductivity in the Square Lattice Hubbard Model at High Temperatures: Importance of Vertex Corrections, Phys. Rev. Lett. **123**, 036601 (2019).

[65] E. W. Huang, R. Sheppard, B. Moritz, and T. P. Devereaux, Strange metallicity in the doped Hubbard model, Science **366**, 987 (2019).

[66] P. T. Brown, D. Mitra, E. Guardado-Sanchez, R. Nourafkan, A. Reymbaut, Charles-David Hébert, S. Bergeron, A.-M. S. Tremblay, J. Kokalj, D. A. Huse, P. Schauß, and W. S. Bakr, Bad metallic transport in a cold atom Fermi-Hubbard system, Science **363**, 379 (2018).